DES-2019-0471
FERMILAB-PUB-20-082-AE-SCD

MNRAS **000**, 1–40 (2020) Preprint 17 January 2022 Compiled using MNRAS LATEX style file v3.0

STRIDES: Spectroscopic and photometric characterization of the environment and effects of mass along the line of sight to the gravitational lenses DES J0408−5354 and WGD 2038−4008

E. J. Buckley-Geer,[1]★ H. Lin,[1] C. E. Rusu,[2] J. Poh,[3,4] A. Palmese,[1] A. Agnello,[5] L. Christensen,[5] J. Frieman,[1,3,4] A. J. Shajib,[6] T. Treu,[6] T. Collett,[7] S. Birrer,[6,8] T. Anguita,[9,10] C. D. Fassnacht,[11] G. Meylan,[12] S. Mukherjee,[13] K. C. Wong,[14] M. Aguena,[15,16] S. Allam,[1] S. Avila,[17] E. Bertin,[18,19] S. Bhargava,[20] D. Brooks,[21] A. Carnero Rosell,[22] M. Carrasco Kind,[23,24] J. Carretero,[25] F. J. Castander,[26,27] M. Costanzi,[28,29] L. N. da Costa,[16,30] J. De Vicente,[22] S. Desai,[31] H. T. Diehl,[1] P. Doel,[21] T. F. Eifler,[32,33] S. Everett,[34] B. Flaugher,[1] P. Fosalba,[26,27] J. García-Bellido,[17] E. Gaztanaga,[26,27] D. Gruen,[35,36,37] R. A. Gruendl,[23,24] J. Gschwend,[16,30] G. Gutierrez,[1] S. R. Hinton,[38] K. Honscheid,[39,40] D. J. James,[41] K. Kuehn,[42,43] N. Kuropatkin,[1] M. A. G. Maia,[16,30] J. L. Marshall,[44] P. Melchior,[45] F. Menanteau,[23,24] R. Miquel,[46,25] R. L. C. Ogando,[16,30] F. Paz-Chinchón,[23,24] A. A. Plazas,[45] E. Sanchez,[22] V. Scarpine,[1] M. Schubnell,[47] S. Serrano,[26,27] I. Sevilla-Noarbe,[22] M. Smith,[48] M. Soares-Santos,[49] E. Suchyta,[50] M. E. C. Swanson,[24] G. Tarle,[47] D. L. Tucker,[1] and T. N. Varga[51,52] (The DES Collaboration)
Affiliations appear at the end of the paper

Accepted XXX. Received YYY; in original form ZZZ

ABSTRACT

In time-delay cosmography, three of the key ingredients are 1) determining the velocity dispersion of the lensing galaxy, 2) identifying galaxies and groups along the line of sight with sufficient proximity and mass to be included in the mass model, and 3) estimating the external convergence $\kappa_{\rm ext}$ from less massive structures that are not included in the mass model. We present results on all three of these ingredients for two time-delay lensed quasar systems, DES J0408−5354 and WGD 2038−4008 . We use the Gemini, Magellan and VLT telescopes to obtain spectra to both measure the stellar velocity dispersions of the main lensing galaxies and to identify the line-of-sight galaxies in these systems. Next, we identify 10 groups in DES J0408−5354 and 2 groups in WGD 2038−4008 using a group-finding algorithm. We then identify the most significant galaxy and galaxy-group perturbers using the "flexion shift" criterion. We determine the probability distribution function of the external convergence $\kappa_{\rm ext}$ for both of these systems based on our spectroscopy and on the DES-only multiband wide-field observations. Using weighted galaxy counts, calibrated based on the Millennium Simulation, we find that DES J0408−5354 is located in a significantly underdense environment, leading to a tight (width ∼ 3%), negative-value $\kappa_{\rm ext}$ distribution. On the other hand, WGD 2038−4008 is located in an environment of close to unit density, and its low source redshift results in a much tighter $\kappa_{\rm ext}$ of ∼ 1%, as long as no external shear constraints are imposed.

Key words: gravitational lensing: strong – quasars: individual: DES J0408−5354 , WGD 2038−4008 – galaxies: groups: general

1 INTRODUCTION

When a source with a time-varying luminosity such as a quasar or a supernova undergoes strong gravitational lensing, the light reaching the observer from the multiple images takes different paths and hence different travel times. It was noted by Refsdal (1964) that these time-delays between the images can be used to measure cosmological distances and the Hubble constant H_0. In recent years, the H_0 Lenses in COSMOGRAILâĂŹs Wellspring (H0LiCOW) collaboration has been leading an active time-delay cosmography program to measure H_0 using lensed quasars, see Suyu et al. (2017); Wong et al. (2019) and references therein. For a recent review of the field of time-delay cosmography see Treu & Marshall (2016). The significant improvements in the uncertainty in the measurements of H_0 in the last two decades have come from the understanding of the key ingredients required to achieve an accurate measurement. In particular, three of these ingredients are: 1) determining the velocity dispersion of the lensing galaxy, 2) identifying galaxies and groups along the line of sight that are close enough to the lens and massive enough to be included in the mass model, and 3) estimating the external convergence $\kappa_{\rm ext}$ due to less massive structures that are not included explicitly in the mass model. In this work, we present results on these three ingredients for two time-delay lensed quasar systems, DES J0408−5354 (source redshift $z_{\rm s} = 2.375$, main deflector redshift $z_{\rm d} = 0.5967$, Lin et al. 2017) and WGD 2038−4008 ($z_{\rm s} = 0.777$, $z_{\rm d} = 0.2283$, Agnello et al. 2018), as part of the STRong Lensing Insights into the Dark Energy Survey (STRIDES) campaign (Treu et al. 2018), an external collaboration of the Dark Energy Survey.

It has been known for sometime that including stellar kinematics of the lensing galaxy allows one to break the degeneracies inherent in the mass profile of the lens (Treu & Koopmans 2002). To obtain the stellar velocity dispersion of the lens we took spectroscopic observations of the main lensing galaxy in DES J0408−5354 and WGD 2038−4008 .

If the perturbers along the line of sight are not explicitly accounted for in the lens modeling, these perturbations can result in systematic errors of order a few percent in the inferred value of H_0. To reduce such systematics, we identify galaxies and galaxy groups in the fields of DES J0408−5354 and WGD 2038−4008 that may significantly impact the lensing potential of the system. These galaxies and galaxy groups will be included in the lens models for both DES J0408−5354 (Shajib et al. 2019a, Yidirim et al. in prep) and WGD 2038−4008 (Wong et al. in prep).

To identify the most significant perturbing galaxies and galaxy groups, we use the "*flexion shift*" diagnostic proposed by McCully et al. (2014, 2017), which has also been used in the line-of-sight analysis of the H0LiCOW lenses HE 0435−1223 (Sluse et al. 2017) and WFI 2033−4723 (Sluse et al. 2019). This diagnostic estimates the difference in lensed image positions caused by the leading order non-tidal (i.e. third-order) perturbation produced by a nearby galaxy or galaxy group. McCully et al. (2017) showed that by explicitly modeling perturbers with flexion shifts larger than the conservative limit of $\Delta_3 x > 10^{-4}$ ″, we can constrain the bias on H_0 due to this uncertainty to the percent level.

In addition, we determine for both systems the probability distribution function of the external convergence $\kappa_{\rm ext}$ due to less massive structures, which do not need to be explicitly incorporated in the mass modeling, but nonetheless contribute a uniform mass-sheet. Indeed, if unaccounted for, this quantity would bias H_0 such that $H_0 = H_0^{\rm model}(1 - \kappa_{\rm ext})$ (e.g., Suyu et al. 2010a), for $H_0^{\rm model}$ obtained from lens modeling. For the first time we determine $\kappa_{\rm ext}$ based on multi-band (*griz*), wide-field images obtained from the Dark Energy Survey[1] (DES) data. Following previous work (Fassnacht et al. 2011; Greene et al. 2013; Rusu et al. 2017; Rusu et al. 2019; Birrer et al. 2019; Chen et al. 2019), we measure the under/overdensity of the line of sight towards both lens systems relative to the "average" line of sight density throughout the Universe, obtained from the cosmologically representative sample provided by the DES in the form of a set of control fields. Aiming to constrain $\kappa_{\rm ext}$ as tightly as possible, as well as to study the effect of different analysis choices, we determine under/overdensities using various combinations of weighting schemes for the galaxy counts, such as the radial distance to the lens/field center and the redshift. Finally, we convert the measured under/overdensities into a $\kappa_{\rm ext}$ distribution, using ray-tracing through the Millennium Simulation (MS; Springel et al. 2005). We explore several aperture sizes, and two different photometric redshift algorithms, which we further test through simulations.

We perform a spectroscopic survey to obtain redshifts of galaxies in the fields of DES J0408−5354 and WGD 2038−4008 . This redshift data is used to identify galaxy groups located in the environment or along the line of sight to these strong lensing systems as well as in the calculation of the under/overdensity of the line of sight towards both lens systems.

The structure of this paper is as follows. In Section 2 we describe our photometric and spectroscopic data, and in Section 3 we present our techniques to measure redshifts and stellar masses. In Section 4 we derive the stellar velocity dispersions for the main lensing galaxies in the two systems, and in Section 5 we describe our technique to identify galaxy groups. In Section 6 we identify the structures which can potentially affect the modeling of the lensing systems. In Section 7 we present our measurement of the relative weighted galaxy count ratios for DES J0408−5354 and WGD 2038−4008 , including accounting for relevant errors. In Section 8 we use ray-tracing through the MS in order to obtain $P(\kappa_{\rm ext})$ for the measured ratios, and present our tests for robustness. Finally, we conclude in Section 9.

The current work represents one of a series of papers from the STRIDES collaboration, which together aim to obtain an accurate and precise estimate of H_0 with a blinded approach, from a comprehensive modelling of DES J0408−5354 and WGD 2038−4008 . In particular, lens modeling is performed by two independent modeling teams (Shajib et al. 2019a, as well as Yildirim et al. in prep, Wong et al. in prep), both of which make use of the stellar velocity dispersion, environment and line-of-sight constraints derived in the present work. Throughout this paper, we assume a flat ΛCDM cosmology with $H_0 = 70$ km s^{-1} Mpc^{-1}, $\Omega_m = 0.3$ for convenience when estimating physical individual galaxy and galaxy group properties (§5-§6). However, in the latter part

[1] https://www.darkenergysurvey.org

of the analysis, where we determine the under/overdensities of the fields of the lenses and then derive $\kappa_{\rm ext}$ distributions using ray-tracing through the MS, we adopt the MS cosmology, $\Omega_m = 0.25$, $\Omega_\lambda = 0.75$, $h = 0.73$, $\sigma_8 = 0.9$ for consistency. This is not expected to have a significant effect on the inference of H_0 (see Section 8). We present all magnitudes in the AB system. We define all standard deviations as the semi-difference between the 84th and 16th percentiles.

2 DATA

The Dark Energy Survey (DES) is a deep sky survey that was carried out using the Dark Energy Camera (DECam, Flaugher et al. 2015) located on the Blanco 4m telescope at the Cerro Tololo Inter-American Observatory in the Chilean Andes. The survey ran from 2013-2019 (Diehl et al. 2019) and covered ~ 5100 sq. degs of the southern sky in five optical filters (*grizY*). The DES data are processed by the DES Data Management team (DESDM, Morganson et al. 2018) to produce annual data releases that consist of coadded images and object catalogs. We have used two data sets for the work described here, the first year of DES data which is referred to as DES Year 1 (Y1) and the first three years known as DES Year 3 (Y3). The median single epoch PSF FWHM in the *i*-band is 0.88″and the coadd magnitude limit in the *i*-band is 23.44. More details of the survey data can be found in Abbott et al. (2018).

2.1 Spectroscopic Observations

Spectroscopic observations were carried out using three instruments: (1) the Gemini Multi-Object Spectrograph (GMOS-S) on the Gemini South telescope; (2) the Low Dispersion Survey Spectrograph (LDSS-3) on the Magellan Clay telescope; and (3) the Multi Unit Spectroscopic Explorer (MUSE) on the European Southern Observatory (ESO) Very Large Telescope (VLT) Unit Telescope 4 (UT4). Table 1 summarizes details of the spectroscopic data taken using these three telescope+instrument setups.

The GMOS-S observations were taken as part of two programs: (1) a Gemini Large and Long Program (LLP; PI: E. Buckley-Geer; program IDs GS-2015B-LP-5 and GS-2017A-LP-5) of spectroscopic follow-up for DES strong lensing systems and for DES photometric redshift (photo-z) calibrations; and (2) a dedicated program (PI: H. Lin; program ID GS-2018B-Q-220) to observe line-of-sight galaxy redshifts and lensing galaxy velocity dispersions for our two lensed quasar systems. These programs observed a total of four GMOS-S multi-object spectroscopy (MOS) masks for DES J0408−5354 and two masks for WGD 2038−4008 , and the data were taken in queue mode on Gemini South during the semesters 2015B, 2017A, and 2018B. Nearly all the masks were each observed using both the GMOS-S B600 and R400 gratings, in order to provide spectral coverage over both blue and red wavelength ranges, respectively, spanning approximately 3800Å−7500Å and 5000Å−10500Å. Multiple science exposures were taken to reject cosmic rays, and the grating central wavelength was dithered slightly for different exposures to fill in wavelength gaps due to spatial gaps between the three GMOS-S CCDs. Flat field and wavelength calibration exposures were interspersed with the science exposures.

Table 1. Spectroscopic observations for the DES J0408−5354 and WGD 2038−4008 systems.

Mask/Cube	Telescope/Instrument Grating/ Grism	UT Date	Exposure time (sec)
DES J0408−5354			
Gemini South/GMOS-S			
(1) DESJ0408-5354_42	B600	2015 Dec 09	4 × 900
(2) DESJ0408-5354_42	R400	2015 Dec 09	4 × 900
(3) DESJ0408-5354_45	B600	2017 Apr 26−27	5 × 900
(4) DESJ0408-5354_45	R400	2017 Mar 30−31	4 × 900
(5) DESJ0408-5354_A	B600	2018 Dec 04	4 × 900
(6) DESJ0408-5354_A2	R400	2019 Feb 04	6 × 1000
(7) DESJ0408-5354_B	B600	2018 Dec 09	4 × 900
(8) DESJ0408-5354_B	R400	2018 Dec 09	4 × 900
Magellan Clay/LDSS-3			
(9) des0408a	VPH-All	2018 Jan 21	7 × 780
(10) des0408b	VPH-All	2018 Jan 21	6 × 780
(11) des0408c	VPH-All	2018 Jan 22	7 × 780
(12) des0408d	VPH-All	2018 Jan 22	6 × 780
VLT UT4/MUSE			
(13) MUSE		2019 Jan 11,13	14400
WGD 2038−4008			
Gemini South/GMOS-S			
(14) DESJ2038-4008_A	B600	2018 Nov 06	4 × 900
(15) DESJ2038-4008_A	R400	2018 Nov 07	4 × 900
(16) DESJ2038-4008_B	B600	2018 Nov 07	4 × 900

The LDSS-3 observations were taken as part of a semester 2018A Magellan program (PI: J. Frieman) to obtain line-of-sight galaxy spectroscopy for DES J0408−5354 and two other lensed quad quasar systems. Four LDSS-3 MOS masks were observed for DES J0408−5354 over the two nights 2018 January 21,22 UT. Each mask was observed using the LDSS-3 VPH-All grism, with wavelength coverage of about 3800Å−10500Å. Multiple science exposures were taken to reject cosmic rays. Flat field and wavelength calibration exposures were taken immediately before and after the sequence of science exposures.

The VLT MUSE observations were taken as part of an ESO program (0102.A-0600(E), PI: A. Agnello) to do integral field spectroscopy of DES J0408−5354 and its surrounding field. The MUSE observations were done in wide-field mode with adaptive optics corrections and were carried out over the two nights 2019 Jan 11 and 13. The final MUSE data cube covered an area of 92″ × 95″, and the wavelength coverage spanned 4700Å−5803Å and 5966Å−9350Å. Additional spectroscopic analysis of the MUSE data and further details of the observations and data processing are given in Shajib et al. (2019a).

2.2 Spectroscopic target selection

Galaxy targets for the Gemini and Magellan masks were selected using DES photometry. The exact selection criteria changed somewhat with time, due to improvements in DES photometric measurements, star-galaxy separation, and object catalogs. Specifically, three sets of selection criteria were used for the masks in Table 1, listed below in order

from earliest to latest in time.

(A) Gemini South masks (1)-(4): Galaxies were selected from the DES Year 1 (Y1) "Y1A1 COADD" catalog (Drlica-Wagner et al. 2018), using the i-band `SExtractor AUTO` magnitude (Bertin & Arnouts 1996) cuts $20 \leq$ `MAG_AUTO_I` < 22.5. No Milky Way extinction corrections were applied to the magnitudes before selection. Star-galaxy separation used the `SExtractor SPREAD_MODEL` classifier (Desai et al. 2012), also in the i-band: `SPREAD_MODEL_I` > 0.002.

(B) Magellan masks (9)-(12): Galaxy targets were now selected from the deeper DES Year 3 (Y3) data set, specifically from the "Y3 GOLD" (Sevilla et al. in prep) version 1.0 catalog, using the i-band magnitude cuts $18 \leq$ `MAG_AUTO_I` < 23, in particular extending the faint magnitude limit fainter to aim for a deeper sample. Again no Milky Way extinction corrections were applied to the magnitudes. Star-galaxy separation used the same i-band cut: `SPREAD_MODEL_I` > 0.002.

(C) Gemini South masks (5)-(8) and (14)-(16): These masks were the latest to be designed and therefore used improved selection methods compared to the masks in (A) and (B). Galaxies were again selected from the "Y3 GOLD" data set, but using the most current version 2.2 catalog. We also changed the selection magnitudes from `AUTO` to `MOF` (Drlica-Wagner et al. 2018, Sevilla et al. in prep) magnitudes, where the latter provide improved photometry, based on simultaneous multiepoch, multiband, and multiobject fits. The adopted i-band cuts were $15 \leq$ `MOF_CM_MAG_CORRECTED_I` < 23, where these MOF magnitudes also included Milky Way extinction corrections and several other sub-percent photometric zeropoint corrections (Sevilla et al. in prep). Finally, we also updated the star-galaxy separation classifier to `EXTENDED_CLASS_MASH_MOF` (Sevilla et al. in prep), specifically using the cuts `EXTENDED_CLASS_MASH_MOF` $= 3$ (indicating "high confidence galaxies") or 2 (indicating "mostly galaxies"). For $i \leq 22.5$, this classification should yield a galaxy efficiency $> 98.5\%$ and a stellar contamination $< 1\%$ (Sevilla et al. in prep).

Each Magellan LDSS-3 and Gemini South GMOS-S mask included galaxy targets distributed over about a $5.5' \times 5.5'$ sky area centered on each lensed quasar system. Generally one to three slits on each mask were manually designed to target objects in or close to the lensed quasar system, e.g., to measure the redshift or velocity dispersion of the main lensing galaxy in each system, or to observe close nearby neighbor galaxies of the systems. The remaining targets were selected automatically by `GMMPS`[2] or `maskgen`[3], the respective GMOS-S or LDSS-3 mask design software, both of which designed masks to maximize the number of targets observed. The potential set of galaxies that could be targeted was subject to the selection criteria described above. In addition, at the time each mask was designed, we removed from the initial target list any galaxies which already had high-confidence redshifts from previous observations, or which were already targeted on companion masks designed for the same semester's (Gemini) observing queue or (Magellan) observing run. Moreover, for the Magellan LDSS-3 targets (only), we assigned targeting priorities as inputs to `maskgen`, depending on the i-band magnitude and on the radius from the DES J0408−5354 quad system. Specifically, for galaxies with radius $\leq 3'$, we assigned priorities based on `MAG_AUTO_I` (as in criteria (B) above), with highest priority given to bright galaxies `MAG_AUTO_I` < 19.5, next priority to galaxies otherwise brighter than `MAG_AUTO_I` $= 22$, and lowest priority to galaxies otherwise brighter than `MAG_AUTO_I` $= 23$. Finally, for galaxies with radius $> 3'$, we assigned lower priorities than for galaxies $\leq 3'$, and these priorities were tied linearly to `MAG_AUTO_I` (with brighter galaxies at higher priority).

[2] https://gmmps-documentation.readthedocs.io/en/latest/
[3] https://code.obs.carnegiescience.edu/maskgen

2.3 Data for the determination of the line-of-sight under/overdensities

In order to determine the line-of-sight under/overdensities for DES J0408−5354 and WGD 2038−4008 we need a catalog of galaxy properties that includes magnitudes and photometric redshifts. We have used the catalogs from the Year 3 Gold version 2.2 catalog.

We have used the photometric redshifts computed using the DNF machine-learning algorithm described in De Vicente et al. (2016). We also repeat the analysis using the photometric redshifts derived with the Bayesian Photometric Redshift (BPZ: Benítez 2000; Hoyle et al. 2018) method. If an object has a spectroscopic redshift from Gemini or Magellan, as described below in §3.1, then we use that redshift instead of the photometric redshift. In Figure 1 we show the comparison of the photometric redshifts from the DNF algorithm to the spectroscopic redshifts for objects with $i < 22.5$. The comparison of the DNF and BPZ photo-z's for the objects that only have photometric redshifts is shown also in Figure 1 for both DES J0408−5354 and WGD 2038−4008 . We observe that there is no obvious mismatch between the two algorithms so we have used results from both of them in the subsequent analysis. We note that the photometric redshifts are computed using the photometry in the *griz* filters only, as Hoyle et al. (2018) have found that the Y−band adds little to no predictive power.

2.3.1 The Control Field: DES

To to apply the weighted number counts technique we need a control field against which to determine an under/overdensity, the constraint we will eventually use to determine $P(\kappa_{\rm ext})$. As both lensing systems are within the DES footprint we have chosen to use the full DES survey footprint of 5100 sq. deg to provide our control field. This differs from our approach in the past, where we have used control fields observed with the *Hubble Space Telescope (HST)* (Suyu et al. 2010b; Fassnacht et al. 2011; Suyu et al. 2013; Greene et al. 2013), and from CFHTLenS (Heymans et al. 2012), (e.g., Rusu et al. 2017; Rusu et al. 2019; Birrer et al. 2019; Chen et al. 2019). The choice of control fields from DES itself, as opposed to other large-scale cosmological surveys, is opti-

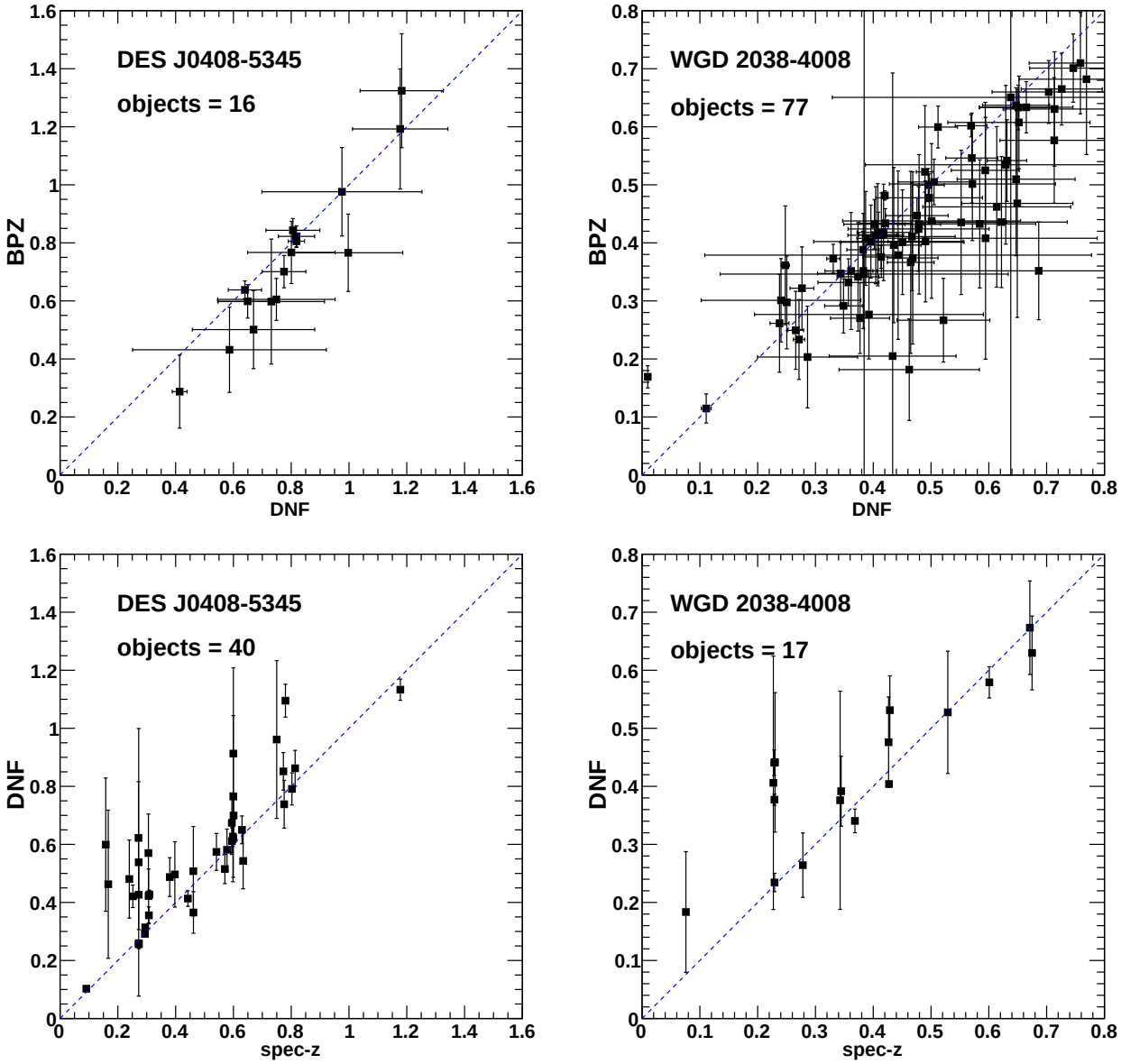

Figure 1. Upper figures: Comparison of the DNF and BPZ photometric redshifts for galaxies with no spectroscopic redshift which have $i < 22.5$ within 120 arcsec of the lens center. The dashed line indicates BPZ = DNF. Left figure DES J0408−5354 , right figure WGD 2038−4008 . Lower figures: Comparison of spectroscopic and DNF photometric redshifts for galaxies with $i < 22.5$ within 120 arcsec of the lens center. The dashed line indicates specz = DNF photo-z. Left figure DES J0408−5354 , right figure WGD 2038−4008 .

mal. This choice avoids potential biases to which our technique of obtaining $\kappa_{\rm ext}$ from weighted number count ratios may be sensitive, such as due to mismatches in image resolution, depth and star-galaxy classification between the lens (target) fields and the control fields (e.g., Rusu et al. 2017). The full Year 6 DES survey footprint consists of 10169 tiles, each $10,000 \times 10,000$ pixels or 0.53 sq deg in area. We take a sample of tiles from the center of the footprint that are far from the survey edges and also eliminate tiles that contain very bright stars or very large galaxies. This results in a total of 5402 tiles of which we select 843 from across the survey footprint. For each tile we select six fields each of 1000×1000 pixels. This gives us a total of 5094 control fields spread over the sky and covering ≈ 27 sq deg. The location of these six fields are shown in Figure 2 for one of the DES tiles. This should allow us to account for sample variance.

2.3.2 The galaxy samples for the target and control fields

For the target fields we make an initial selection of all objects from the Y3 Gold catalog that fall within a $4' \times 4'$ box centered on the lens. For the control fields we make the same selection but using the center of the control field. We select all objects that satisfy `FLAGS_GOLD` = 0 and

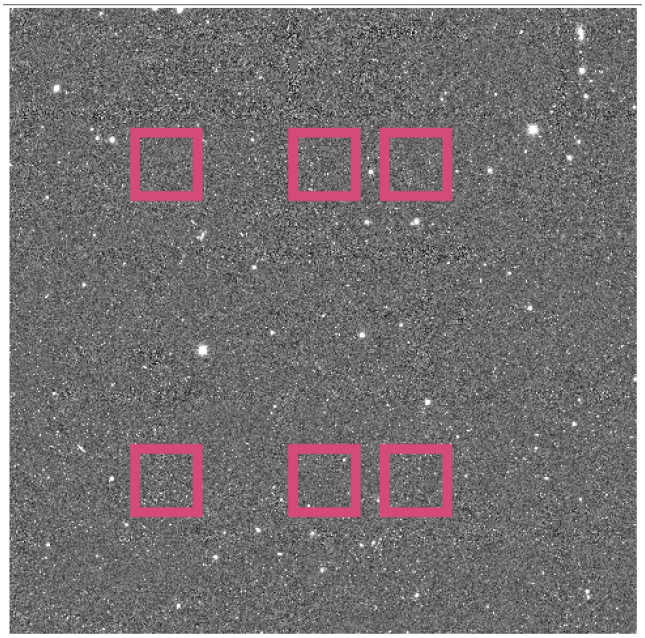

Figure 2. A typical DES tile showing the location of the control fields. Each magenta box is 1000×1000 pixels.

`EXTENDED_CLASS_SOF` ≥ 2, which selects galaxies[4]. We are using the Single-Object Fitting (SOF) magnitudes that are computed using a simplified version of the Multi-Object Fitting (MOF) algorithm described in section 6.3 of Drlica-Wagner et al. (2018). We select all objects with i-band magnitude $0 <$ `SOF_CM_MAG_CORRECTED_I` < 22.5. The faint-end limiting magnitude, which is the same one used in Rusu et al. (2019) based on the analysis in Sluse et al. (2019), also for the purpose of constraining H_0, ensures that the galaxy classification is reliable, and that the galaxy catalog is complete. It is also deep enough (Collett et al. 2013) to keep biases on $\kappa_{\rm ext}$ due to depth significantly below the 1% level. We are using the photometric redshifts that were calculated using the SOF magnitudes, namely `DNF_ZMEAN_SOF` and `BPZ_ZMEAN_SOF`. We also require that the redshift `DNF_ZMEAN_SOF` or `BPZ_ZMEAN_SOF` of the objects satisfy $z < z_s$, where z_s is the source redshift, and that their distance Δr from the center of the field is less than $120''$. Figure 3 shows the objects that pass these selection criteria in a 1000×1000 pixel field around DES J0408−5354 and WGD 2038−4008 .

3 REDSHIFTS AND STELLAR MASSES

In this section we first describe our spectroscopic redshift measurement procedure, summarize the results, and show the line-of-sight galaxy redshift distributions for each lensing system. We then describe and plot the spectroscopic redshift completeness for the overall galaxy samples in the two systems. Finally, we detail the procedures for measuring stellar masses using photometric model fitting for our galaxies.

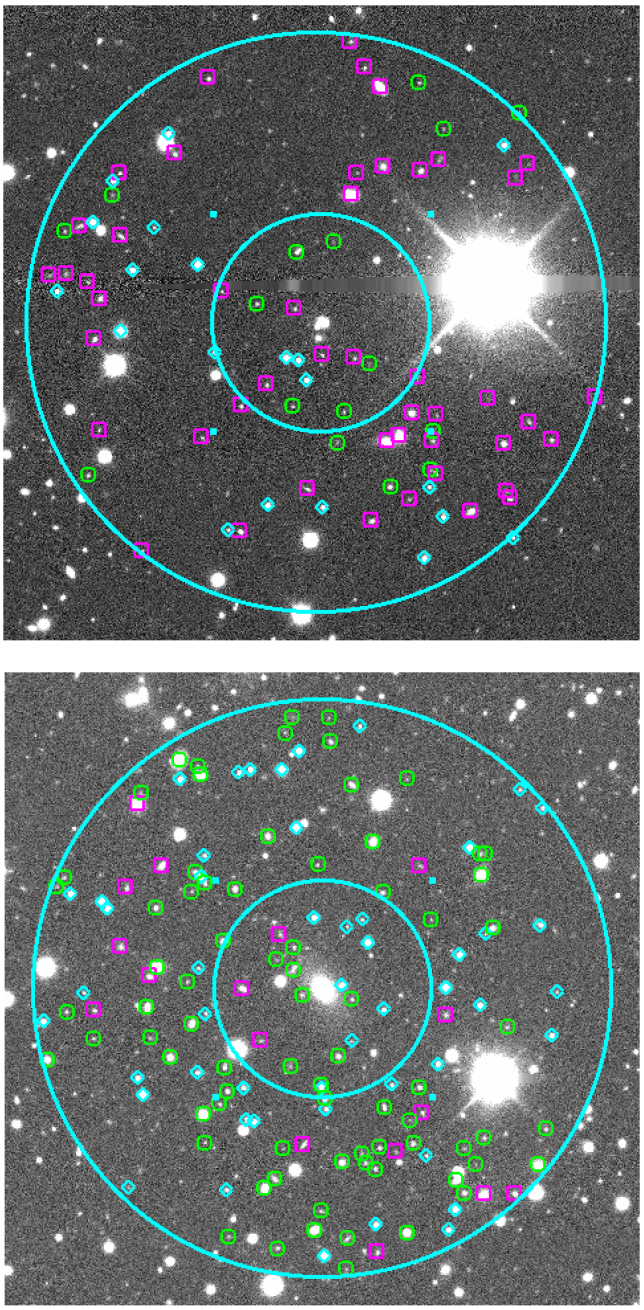

Figure 3. The 1000×1000 pixel field of view for DES J0408−5354 (upper figure) and WGD 2038−4008 (lower figure). North is up and East is left. The $i < 22.5$ galaxies inside the $120''$ radius aperture are indicated by magenta squares for the objects with a spectroscopic redshift and green circles for the objects with no spectroscopic redshift. Stars are indicated by the cyan diamonds. The two concentric cyan circles indicate the apertures of $120''$ and $45''$ radius respectively.

[4] When comparing with the available *HST* data, we found that five objects in the WGD 2038−4008 field are erroneously classified by this pipeline, mainly in the form of stars wrongly classified as galaxies. As some of these are close enough to the lens to bias the inference described below, we were careful to correct the classification.

3.1 Spectroscopic redshifts

The Gemini and Magellan data were processed to 2D and 1D spectra using the IRAF Gemini and COSMOS (Dressler et al. 2011; Oemler et al. 2017) reduction packages, respectively. Initial redshifts were determined automatically (without visual inspection) using the IRAF external package `rvsao` (Kurtz & Mink 1998) to cross correlate the 1D spectra against a set of SDSS galaxy templates. All processed 2D and 1D spectra, along with the corresponding automated redshift results, were visually inspected in order to assign final quality flags to the redshifts. If necessary, an automated redshift may be overridden and manually re-measured from the 2D or 1D spectrum. Only high-confidence redshifts were included in the subsequent analyses.

For DES J0408−5354, we obtained 101 high-confidence galaxy redshifts from Gemini South GMOS-S and 70 from Magellan LDSS-3. From the VLT MUSE data we obtained another 28 redshifts that were not already among the Gemini and Magellan redshifts, thus resulting in a total of 199 high-confidence redshifts for DES J0408−5354. For WGD 2038−4008 we obtained a total of 54 high-confidence galaxy redshifts, all obtained from the Gemini South GMOS-S data. The above counts include the two redshifts of the main lensing galaxies in the systems. Figure 4 shows histograms of the redshift distributions for each lensing system.

3.2 Redshift completeness

We define spectroscopic redshift completeness to be the fraction of DES Y3 Gold (Sevilla et al. in prep) galaxies that have redshifts (as described in §3.1). To define our photometric galaxy sample, we use the latest and best available version of the Y3 Gold catalog, version 2.2, and we also use the same magnitude and star-galaxy separation cuts as listed in target selection criteria (C) of §2.2 above.

For DES J0408−5354, the resulting spectroscopic redshift completeness is 0.68 for 18 <= `MOF_CM_MAG_CORRECTED_I` < 23 galaxies and 5″ <= radius < 3′; see the top panels of Figure 5. For WGD 2038−4008, the redshift completeness is 0.16 for the same *i*-band magnitude and radius ranges, as shown in the bottom panels of Figure 5. Within the plotted magnitude and radius ranges, the redshift completeness stays fairly constant for both systems. The inner radius cut of 5″ is intended to exclude the quasar images from consideration. The outer radius cut is set at 3′ as the redshift completeness drops very rapidly beyond this radius for either system.

3.3 Stellar masses

Stellar masses necessary for the computation of the flexion shift, the criterion used to separate between the structures which need to be accounted for in the lensing model, and those which can be incorporated inside $\kappa_{\rm ext}$ (see §6.1) were computed using the galaxy template fitting code Le PHARE (Arnouts et al. 1999; Ilbert et al. 2006). In the Le PHARE fits, we either used our spectroscopic redshifts when available, or DES Y3 Gold DNF photo-z's (`DNF_ZMEAN_SOF`), combined with MOF photometry (Drlica-Wagner et al. 2018) from the DES Y3 Gold (Sevilla et al. in prep) version 2.2 catalog. Specifically, we used the `MOF_CM_MAG_CORRECTED` magnitudes and their associated errors in the *griz* filters, as these magnitudes included Milky Way extinction and other small photometric corrections (see 2.2).

The galaxy template set used in the Le PHARE fits were taken from the BC03 (Bruzual & Charlot 2003) spectral energy distribution (SED) library. Specifically, we used a set of 27 BC03 simple stellar population models, computed using the Padova 1994 stellar evolution library (described in Bruzual & Charlot 2003) and the Chabrier (2003) initial mass function. The 27 models consisted of 9 exponentially declining star formation rate (SFR) histories (with decay times τ = 0.1, 0.3, 1, 2, 3, 5, 10, 15, 30 Gyr), each computed at 3 different metallicity values (0.4, 1, and 2.5 times solar). Each of the 27 models was also computed at different ages (ranging from 0.2 to 13.5 Gyr) and redshifts (up to a maximum redshift of 1.1, in steps of 0.03 in redshift). No dust extinction was included in the models, but recall the DES magnitudes already included correction for foreground Milky Way extinction. The stellar masses and uncertainties computed from the Le PHARE fits are tabulated in Table A1.

For a few of the close neighbor galaxies of the two lensed quasar systems, the original object deblending and resulting photometry in the DES Y3 catalog were clearly incorrect upon visual inspection of the images. In particular, for DES J0408−5354, the neighbor galaxy with ID number 488066768 (or name G5, in Table 4 or Table A1) had magnitudes that were too bright, and for WGD 2038−4008, the three neighbor galaxies with ID numbers 13, 14, and 15 (Table A1) were originally merged into a single object. To correct these photometry problems, we used the galaxy image fitting code GALFIT (Peng et al. 2010) to redo the galaxy model fitting and photometry for these objects, based on the DES Y3 coadd images in the *griz* filters. These GALFIT results were used to compute stellar masses via Le PHARE.

4 VELOCITY DISPERSIONS OF LENSING GALAXIES

The main lensing galaxies in both the DES J0408−5354 and WGD 2038−4008 systems were specifically targeted for stellar velocity dispersion measurements on a number of the spectroscopic masks listed above in Table 1. For these observations we describe below the details of the targeting on the spectroscopic slits, the procedures used to extract the lensing galaxy spectra, and the method employed to measure velocity dispersions.

4.1 DES J0408−5354 G1

The main lensing galaxy G1 in DES J0408−5354 was measured from four independently observed spectra: two from Magellan LDSS-3, one from Gemini South GMOS-S, and one from VLT MUSE.

G1 was targeted on two of the four Magellan LDSS-3 masks listed in Table1, "des0408a" and "des0408b"; hereafter these two masks will be denoted "Magellan a" and "Magellan b". The slit setup for G1 was the same on both masks, while the remaining targets were different on the two masks. Specifically, the slit was oriented so that it included both G1 and quasar image B (the naming convention for the lensing

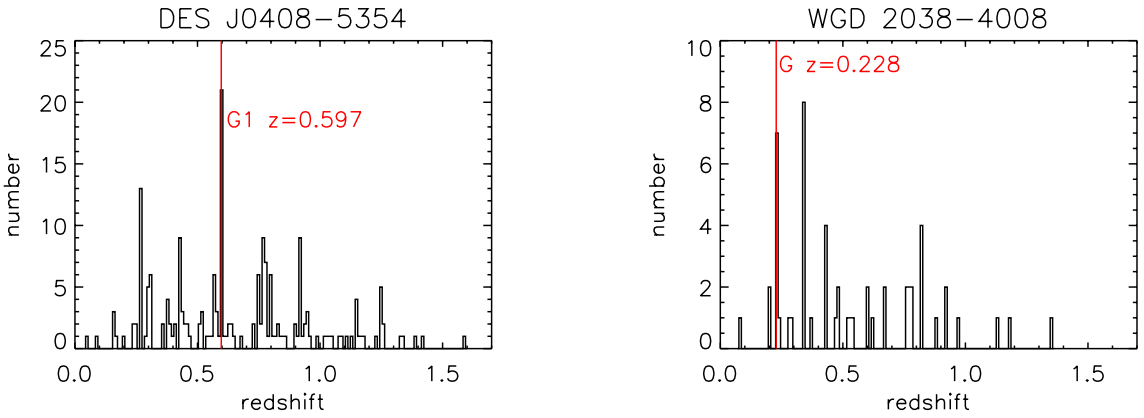

Figure 4. Histograms of line-of-sight galaxy spectroscopic redshifts (§3.1) for the (left) DES J0408−5354 and (right) WGD 2038−4008 systems. In each panel the red vertical line indicates the redshift of the main lensing galaxy in each system.

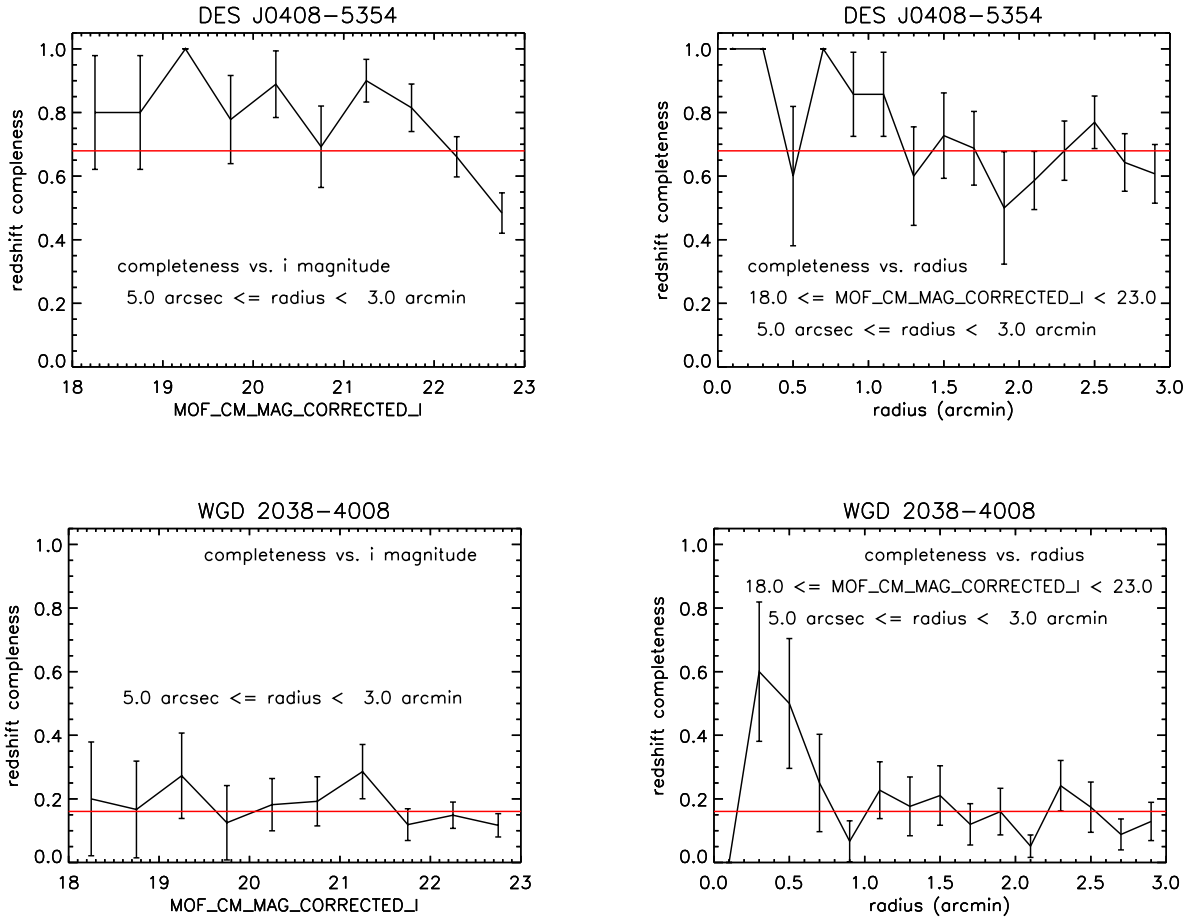

Figure 5. Spectroscopic redshift completeness (defined in §3.2) for DES J0408−5354 (top panels) and WGD 2038−4008 (bottom panels). The left panels show redshift completeness vs. i-band magnitude, within the radius range 5″to 3′ from the lens galaxy in each system. The right panels show redshift completeness vs. radius, within the i-band magnitude range 18 to 23. In all panels the red horizontal line indicates the overall redshift completeness within the indicated magnitude and radius ranges for each system.

galaxy G1 and the lensed quasar images A, B, and D are shown in Lin et al. 2017). In addition, some contaminating flux from quasar image A was also visible in the 2D spectrum from the slit. To extract the 1D spectrum of G1, we first fit the spatial profiles along the slit (at each wavelength) of G1, B, and A by two Moffat profiles and a Gaussian profile, respectively. Moffat profiles were adopted for G1 and B because Gaussian profiles gave worse fits as determined by visual inspection. We subtracted off the best-fit spatial profiles for B and A and summed the remaining flux over an extraction window along the slit of 1″ (approximately the FWHM of G1's Moffat profile) or 2″ (about the extent of G1's profile) in order to extract G1's 1D spectrum.

G1 was targeted on one of the Gemini South GMOS-S masks in Table 1, "DESJ0408-5354_A2" (R400 grating), hereafter denoted "Gemini A2," on a slit which also included quasar image D. The procedure to extract G1's 1D spectrum was entirely analogous to that described above for the Magellan data. To fit the spatial profiles of G1 and D, Moffat profiles were again found to be better than Gaussians.

In the VLT MUSE data cube, the quasar and source light components were first modeled and removed, and the region near C and G2 was masked out. The remaining light from G1 was then extracted to a 1D spectrum by summing the light over a $1'' \times 1''$ box or a $2.2'' \times 2.2''$ box.

The velocity dispersion of G1 was then measured from the above data using the ULySS (Koleva et al. 2009) galaxy spectral modeling package. In the rest wavelength range 4800Å to 5500Å, including the Hβ, Mg, and CaFe features, the G1 spectra were fit to Vazdekis et al. (2010) stellar population models, which used the MILES stellar library (Sánchez-Blázquez et al. 2006) and the Salpeter (1955) initial mass function. The wavelength dependent line spread function (LSF) in the Magellan and Gemini-South data were determined from the widths of the arc lamp lines in the respective wavelength calibration spectra, while the LSF of the MUSE data were taken from the fits given in §3.1 of Guérou et al. (2017). Because the Gemini-South and in particular Magellan LSFs were noticeably non-Gaussian, we modified the ULySS package so that it could make use of an empirical LSF, instead of an analytic Gaussian (or low-order Gauss-Hermite) LSF. The resulting velocity dispersion measurements and associated statistical errors are given in Table 2, showing good agreement among the results from the four independent data sets. Plots of the 1D spectra and best-fit models for the 1″ extraction window cases are shown in Figure 6.

4.2 WGD 2038−4008 G

The main lensing galaxy G in WGD 2038−4008 was measured from one spectrum observed using Gemini South GMOS-S, specifically on mask (14) listed in Table 1: "DESJ2038-4008_A" (B600 grating), hereafter denoted "Gemini A" for simplicity. One slit on this mask targeted galaxy G together with the quasar images C and D (the naming convention for the lensing galaxy and the lensed quasar images are shown in Figure 1 of Agnello et al. 2018). To extract the 1D spectrum of G, we used the same method described above in §4.1. Specifically, we fit the spatial profiles of G, C, and D with three Moffat profiles, subtracted off the best-fit profiles of C and D, and then summed the remaining flux over extraction windows of 1″ or 2″ along the length of the slit. The velocity dispersion of G was then measured with ULySS, using the same rest wavelength range and the same stellar population models as above in §4.1. The resulting velocity dispersion measurements and statistical errors are given in Table 2. The 1D spectrum and best-fit model for the 1″ extraction window case are shown in Figure 6.

Table 2. Velocity dispersion results for the main lensing galaxies in the DES J0408−5354 and WGD 2038−4008 systems. Details of the measurements are given in §4.

Data set	Velocity dispersion (km/s)	Slit width (arcsec)	Extraction window (arcsec)	Seeing FWHM (arcsec)	Moffat index β
DES J0408−5354					
Magellan a	230 ± 37	1.0	1.0	0.68	2.97
Magellan b	236 ± 42	1.0	1.0	0.76	3.20
Gemini A2	220 ± 21	0.75	1.0	0.52	3.06
MUSE	227 ± 9	1.0	1.0	0.61	1.55
Magellan a	209 ± 37	1.0	2.0	0.68	2.97
Magellan b	230 ± 47	1.0	2.0	0.76	3.20
Gemini A2	261 ± 21	0.75	2.0	0.52	3.06
MUSE	227 ± 9	2.2	2.2	0.61	1.55
WGD 2038−4008					
Gemini A	296 ± 19	0.75	1.0	0.90	1.74
Gemini A	303 ± 24	0.75	2.0	0.90	1.74

5 GALAXY GROUP IDENTIFICATION

5.1 Galaxy Group Identification Algorithm

For galaxy-group identification, we employed the same algorithm used in the spectroscopic analysis of the fields of H0LiCOW lenses HE 0435−1223 (Sluse et al. 2017) and WFI 2033−4723 (Sluse et al. 2019), which is based on the group-finding algorithms of Wilman et al. (2005) and Ammons et al. (2014). Wilson et al. (2016) uses a similar method, the results of which were used in the analysis of the H0LiCOW lens PG 1115+080 (Chen et al. 2019). We summarize the method here, and refer interested readers to Sluse et al. (2017) for a more complete description and explanation of parameter choices in this algorithm.

The first step towards identifying galaxy groups involves searching for candidate groups in the spectroscopic redshift distribution of the surveyed galaxy catalog. We begin by constructing a redshift histogram with bins of width 2000 km s^{-1}. We identify redshift bins with 5 or more members as candidate groups. To ensure that candidate group members are not split across two bins due to an arbitrary choice of bin boundaries, we construct a second redshift histogram with the bins shifted by half a width of a bin (1000 km s^{-1}), and count all non-duplicate redshift peaks from both histograms as candidate groups. We include all other galaxies that are within 1500 km s^{-1}of a candidate group member in that candidate group.

Once we have identified the candidate groups, we use a biweight location estimator (Beers et al. 1990) to calculate the mean (group) redshift of each candidate group. The group centroid is also calculated from the positions of the candidate group members. Since Sluse et al. (2019) found that using a luminosity-weighted scheme to calculate the

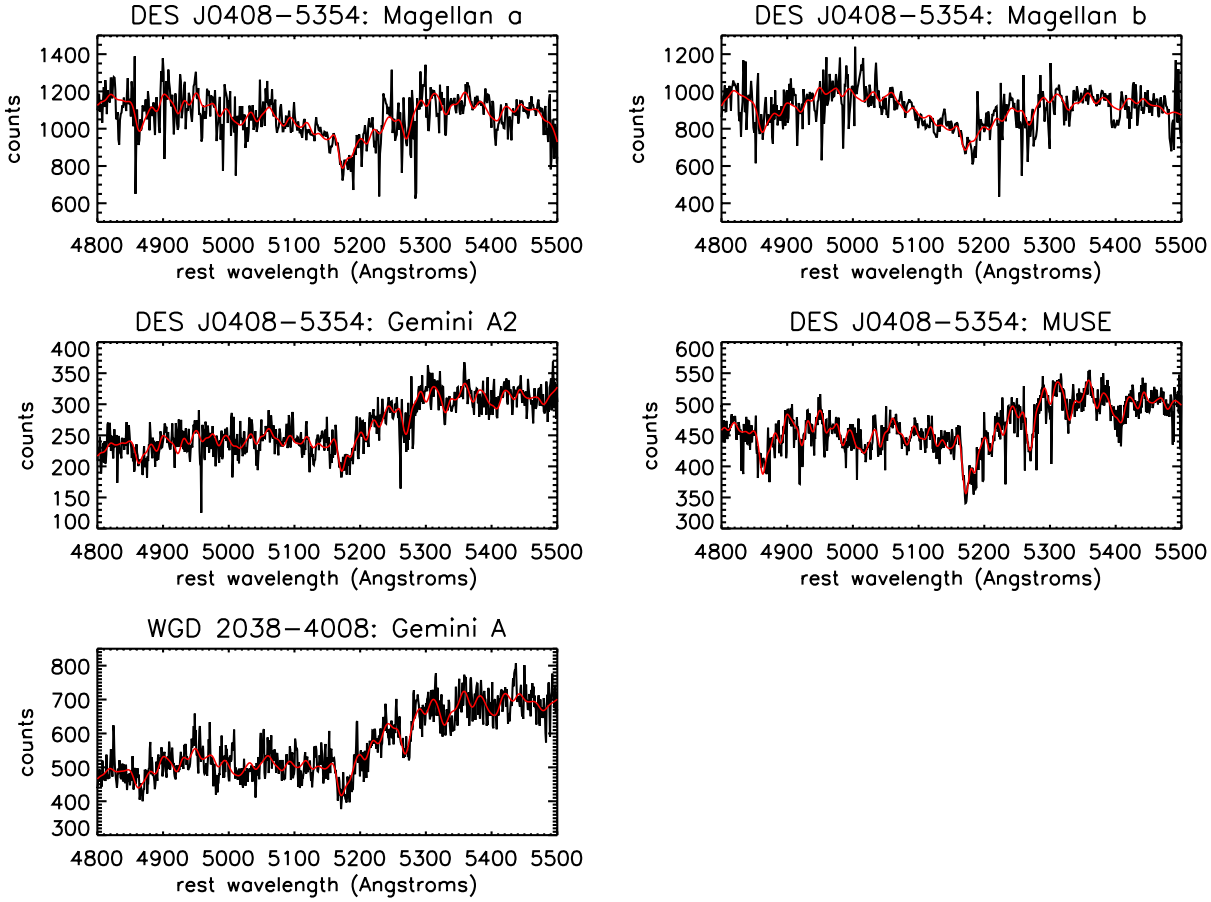

Figure 6. The 1D spectra and fits involved in the velocity dispersion measurements of the main lensing galaxies G1 in the DES J0408−5354 system (top and middle panels) and G in the WGD 2038−4008 system (bottom panel), as described in §4 and listed in Table 2. The black curves in the plots show the observed data, in units of counts vs. rest-frame wavelengths in Angstroms, while the red curves show the best-fit models (details in §4). All the data and fits shown are for the case of a 1″ extraction window (see §4 and Table 2).

centroid does not improve the match between the group centroid and brightest galaxy in this method, we do not use luminosity-weighted centroids here.

Once candidate groups have been identified, they are subjected to an algorithm that iteratively removes outliers in both redshift and angular space until the algorithm converges to a stable solution or a group membership of zero. The latter indicates that the candidate group is not gravitationally linked and is spurious. The algorithm is as follows:

(i) We set the initial observer-frame velocity dispersion, $\sigma_{\rm obs}$ to 500 km s^{-1}. This value will be revised in subsequent iterations.

(ii) Candidate group members that are further than twice the velocity dispersion away from the group redshift are excluded from the group. This corresponds to the following limit

$$\delta z_{\rm max} = n \times \sigma_{\rm obs}/c \qquad (1)$$

where $n = 2$. This redshift limit is converted into an angular separation limit

$$\delta\theta_{\rm max} = \frac{c \times \delta z_{\rm max}}{b(1+z)\,H(z)\,D_\theta(z)} \qquad (2)$$

where $H(z)$ is the Hubble parameter at redshift z and $D_\theta(z)$ is the angular diameter distance from the observer to redshift z. Following Sluse et al. (2017), we set the aspect ratio $b = 3.5$. Candidate group members that have an angular separation that is larger than $\delta\theta_{\rm max}$ from the group centroid are excluded from the group.

(iii) Once cuts have been made in both redshift and angular separation, we recalculate the group centroid, group redshift and observed-frame velocity dispersion $\sigma_{\rm obs}$ from the remaining candidate group members. We obtain the latter two quantities following this framework:

- If there are more than 10 galaxies remaining, we use the biweight location and scale estimators to calculate

the group redshift and velocity dispersion, respectively (Mosteller & Tukey 1977).

- If there are between 4 and 10 galaxies remaining (inclusive), we use the biweight location to calculate the group redshift and the gapper estimator to calculate the velocity dispersion (Wainer & Thissen 1976; Beers et al. 1990).
- If there are fewer than 4 galaxies, we use the mean redshift as the group redshift and the standard deviation as the velocity dispersion.

Steps (ii) and (iii) are repeated until we reach a stable solution. Galaxies that are members of these identified groups are then used to infer group properties, such as the group redshift, centroid, velocity dispersion, and flexion shift (following the method described in §6.1. The rest-frame velocity dispersions are calculated from the observer-frame velocity dispersions using

$$\sigma_{\rm rest} = \frac{\sigma_{\rm obs}}{1 + \bar{z}_{\rm group}}. \quad (3)$$

We then estimate uncertainties in the group properties by bootstrapping (i.e. random sampling with replacement) the group members of each group 1000 times. We recalculate the group properties of the resampled groups, and use the bootstrapped distribution in those quantities to estimate their uncertainties.

Because the associated measurement uncertainties of the galaxies in the spectroscopic redshift catalog ($\Delta v_{\rm err} \sim 100$ km s^{-1}, see §3) are of order the measured velocity dispersion of many of the identified groups, care must be given to account for these uncertainties. To this end, we forward-model the kinematic datasets to infer the velocity dispersion given measurement uncertainties, following techniques used in dwarf-galaxy studies (e.g. Koposov et al. (2011); Walker & Peñarrubia (2011); Amorisco & Evans (2012)), where it has been found to be especially relevant for systems with small numbers of discrete kinematic tracers (Martin et al. 2018; Laporte et al. 2019). We construct a generative likelihood model for the data and evaluate the posterior probability distribution for the intrinsic velocity dispersion, $\sigma_{\rm int}$. The likelihood function is

$$\mathcal{L} = \prod_{\rm i} \frac{1}{\sqrt{2\pi}\sigma_{\rm obs}} \exp\left(-0.5\left(\frac{v_i - \langle v\rangle}{\sigma_{\rm obs}}\right)^2\right) \quad (4)$$

where $\langle v\rangle$ is the mean velocity, the product is over all member galaxies i of the galaxy group, and $\sigma^2_{\rm obs} = \sigma^2_{\rm int} + \Delta v^2_{\rm err}$. We assume $\Delta v_{\rm err} = 100$ km s^{-1}, and a non-informative Jeffreys prior for the intrinsic velocity dispersion $\sigma_{\rm int}$ (i.e. $p(\sigma_{\rm int}) \propto 1/\sigma_{\rm int}$) over the range 1 to 1000 km s^{-1}. We also assume a uniform prior for the mean group velocity $\langle v\rangle$ over the range -500 to 500 km s^{-1}and treat it as a nuisance parameter. We then sample the posterior PDF using the `emcee` affine invariant Markov Chain Monte Carlo sampler (Foreman-Mackey et al. 2013; Goodman & Weare 2010). We then report the median and 68th percentile confidence intervals of the posterior PDF for $\sigma_{\rm int}$ in Table 3. For groups where the posterior PDF for $\sigma_{\rm int}$ peaks near zero and the lower bounds are not well-constrained, we report only the 68th percentile upper limits.

5.2 Identified Groups in the Environment of DES J0408−5354

We applied the galaxy-group identification algorithm to the combined catalog of 199 galaxies with high-confidence redshifts in the field of DES J0408−5354 described in §3. We identified 10 galaxy groups comprising of 76 galaxies from this spectroscopic sample, which we label Group 1-10 in order of increasing group redshift. Their properties are summarized in Table 3, and Figure 7 shows, for each identified galaxy group, the positions of both accepted and rejected trial member galaxies of that group in right ascension and declination, as well as the distances and velocities relative to the converged group centroid.

The largest galaxy group identified in this spectroscopic sample is Group 5, which contains 17 member galaxies, including the lens galaxy of DES J0408−5354 . The centroid of this group is close to DES J0408−5354 (26^{+16}_{-12} arcsec), which is also the most luminous member galaxy in the group.

Aside from group 5, the the identified groups are generally small, with no identified group containing more than 11 member galaxies. For Groups 1, 3, 4, 6 and 7, the posterior PDFs for the intrinsic velocity dispersions peak at or near zero, and the lower limits are not well-constrained. For these distributions, we report the upper 68th percentile confidence intervals for these distributions and treat it as the upper limit of the intrinsic velocity dispersion for that group.

For groups 8 and 9, the distribution of member galaxies in velocity space appears to be bimodal, with two separate subgroups separated by $\sim$ 1000km s^{-1}. However, there are not enough member galaxies in that redshift range to successfully separate these two subgroups into separate groups as none of the individual subgroups have more than 5 potential members.

The choice of parameters used in the group-finding algorithm described in §5.1 can impact the final membership of each galaxy group. As mentioned in §5.1, the choice of fiducial values for the initial observer-frame velocity dispersion $\sigma_{\rm obs} = 500$ km s^{-1}, velocity threshold $n = 2$ (Eq. 1), aspect ratio $b = 3.5$ (Eq. 2) follow that of previous group-finding analyses (Sluse et al. 2017; Sluse et al. 2019; Wilman et al. 2005). We relaxed the parameter n to $n = 3$ to investigate the effect of a more conservative (i.e. more inclusive) choice in the group finding algorithm and found that relaxing the parameters results in groups that contain outlier members, or have bi- or multimodal configurations, all of which are likely to be spurious.

As an additional sanity check, we inspected the Chandra X-ray images of the field (PI: Pooley; Program 20419; ACIS-S; 25ks). No diffuse emission is detected (Pooley, D & Gallo, E. 2019, private communication), with an upper limit (90% CL) of $\sim 10^{44}$ erg/s within a 1Mpc radius (with considerable error bars depending on the assumed temperature). The non-detection makes it unlikely that the lens galaxy is a member of a galaxy cluster.

5.3 Identified Groups in the Environment of WGD 2038−4008

We applied the group-finder to the 54 galaxies with high confidence redshifts in the field of WGD 2038−4008 . From this sample, we identified 2 galaxy groups. The results and

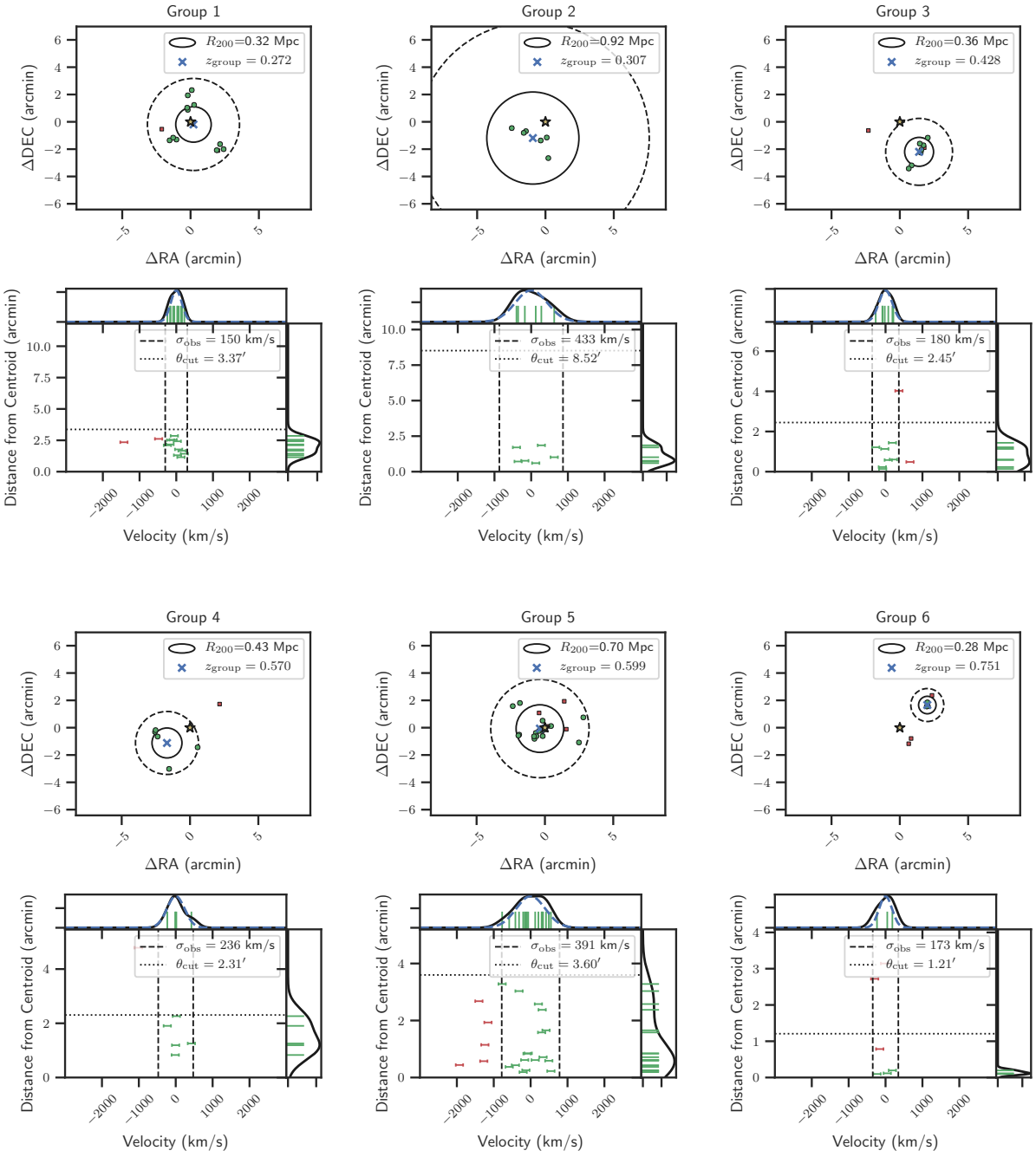

Figure 7. Galaxy groups identified in the spectroscopic sample of galaxies in the field of view of DES J0408−5354 . For each group, the first plot (above) shows the positions of the candidate member galaxies associated with that group relative to the lens galaxy, with rejected group members represented as red squares and accepted group members represented as green circles. The lens galaxy DES J0408−5354 (star) and group centroid (cross) are also displayed. The R_{200} radius of the group is represented by a solid line, while the dashed circle represents the angular separation cut of the group-finding algorithm in its final iteration. The second plot (below) shows the observer-frame velocity of individual member galaxies relative to the group centroid as a function of that galaxy's angular distance from the centroid. Galaxies that passed the iterative algorithm described in §5.1 are shown in green, while trial galaxy members that were cut through the algorithm are shown in red. Horizontal error bars represent the measurement error for each galaxy (see §3). The final observer-frame velocity dispersion and angular separation cuts from the group-finding algorithm are presented as dashed and dotted lines respectively. We also show 1-D histograms and rug plots of the velocity and distance distributions of the member galaxies. The 1-D histograms are produced using a Kernel Density Estimate (KDE) with a bandwidth determined using Scott's Rule. In the 1D velocity histogram, the dashed blue line shows a gaussian with width equal to the observer-frame velocity dispersion of the group.

Table 3. Group properties in the field of view of DES J0408−5354 and WGD 2038−4008 . The columns show the group ID, group redshift, number of spectroscopically identified galaxies in that group, the group rest-frame velocity dispersion (rounded to the nearest 10 km s^{-1}), the group centroid (in RA and Dec), projected distance of the centroid to the lens ($\Delta\theta$), and median flexion shift $\log(\Delta_3 x(\mathrm{arcsec}))$ (see §6.1 for methodology). All reported values are median quantities of 1000 bootstrapped samples, with uncertainties given by the 16th and 84th confidence intervals of the distribution of the bootstrapped quantity. Velocity dispersion estimates are rounded to nearest 10 km s^{-1}. See §6.1.2 for further discussion.

ID	$\bar{z}_{\mathrm{group}}$	N	σ_{rest} (km s^{-1})	σ_{int} (km s^{-1})	R_{200} (Mpc)	RA$_{\mathrm{ctr}}$, DEC$_{\mathrm{ctr}}$ (deg)	error(RA$_{\mathrm{ctr}}$, DEC$_{\mathrm{ctr}}$) (arcmin)	$\Delta\theta$ (arcsec)	$\log_{10}(\Delta_3 x)$ ($\log_{10}$(arcsec))
					DES J0408−5354				
1	0.272	11	110 ± 20	< 70	$0.30^{+0.05}_{-0.06}$	62.096099, -53.903136	0.67, 0.46	32^{+22}_{-16}	< -5.88
2	0.307	6	290^{+60}_{-90}	300^{+160}_{-80}	$0.81^{+0.15}_{-0.24}$	62.065082, -53.919339	0.71, 0.31	94^{+10}_{-10}	$-4.79^{+0.74}_{-0.63}$
3	0.428	7	110 ± 30	< 70	$0.31^{+0.07}_{-0.09}$	62.130389, -53.936509	0.29, 0.29	156^{+10}_{-8}	< -8.04
4	0.570	5	140^{+30}_{-90}	< 160	$0.41^{+0.09}_{-0.25}$	62.042510, -53.918109	1.00, 0.52	122^{+28}_{-21}	< -6.53
5 ★	0.599	17	240^{+30}_{-40}	220^{+60}_{-50}	$0.68^{+0.08}_{-0.11}$	62.079749, -53.901149	0.54, 0.18	26^{+16}_{-12}	$-3.86^{+0.97}_{-0.72}$
6	0.751	3	80 ± 40	< 100	$0.21^{+0.11}_{-0.11}$	62.147320, -53.872270	0.05, 0.09	156^{+3}_{-2}	< -8.06
7	0.768	5	120^{+30}_{-50}	< 120	$0.34^{+0.10}_{-0.15}$	62.084144, -53.898689	0.28, 0.24	17^{+12}_{-7}	< -4.83
8	0.799	6	340^{+60}_{-80}	370^{+170}_{-100}	$0.96^{+0.18}_{-0.22}$	62.143634, -53.894864	0.64, 0.71	120^{+22}_{-22}	$-5.46^{+0.72}_{-0.59}$
9	0.918	9	300^{+40}_{-50}	310^{+120}_{-70}	$0.86^{+0.10}_{-0.15}$	62.051793, -53.892228	0.49, 0.45	90^{+16}_{-17}	$-5.70^{+0.58}_{-0.52}$
10	1.252	7	240^{+30}_{-50}	240^{+110}_{-70}	$0.67^{+0.09}_{-0.15}$	62.124690, -53.913336	0.69, 0.12	87^{+22}_{-21}	$-6.92^{+0.80}_{-0.71}$
					WGD 2038−4008				
1 ★	0.229	7	200^{+70}_{-60}	200^{+90}_{-70}	$0.53^{+0.18}_{-0.16}$	309.528309, -40.126006	0.41, 0.28	62^{+23}_{-24}	$-5.30^{+0.90}_{-0.83}$
2	0.342	8	380^{+70}_{-90}	400^{+150}_{-100}	$1.05^{+0.19}_{-0.26}$	309.543495, -40.142963	0.54, 0.28	91^{+26}_{-27}	$-5.39^{+0.73}_{-0.59}$

Note: ★ Group contains the lens galaxy.

properties of these galaxy groups are summarized in Table 3, and Figure 8 show, for each identified galaxy group, the positions of both accepted and rejected member galaxies of that group, as well as the distances and velocities of individual galaxies relative to the group centroid. Group 1 in WGD 2038−4008 's field contain the eponymous lens galaxy of that field.

6 CONTRIBUTION OF ENVIRONMENT GALAXIES AND GALAXY-GROUPS TO THE LENS STRUCTURE

6.1 Flexion Shift Formalism

A major objective of this analysis is to identify galaxies or galaxy groups along the line of sight or in the environment of lensing systems that significantly perturb the lensing potential of that system and therefore require explicit modeling in the cosmological analysis. Specifically, we want to identify structure that cannot be well-approximated by a uniform perturbation of the lens potential at the position of the lensed images (i.e. external convergence/shear). To do that, we use the "*flexion shift*" diagnostic proposed by McCully et al. (2017), given by

$$\Delta_3 x = f(\beta) \times \frac{(\theta_{\mathrm{E}}\,\theta_{\mathrm{E,p}})^2}{\theta^3}, \tag{5}$$

where θ_{E} and $\theta_{\mathrm{E,p}}$ are the Einstein radii of the main lens and perturber respectively, and θ is the angular separation on the sky between them. The function $f(\beta)$ is

$$f(\beta) \in \left\{ \begin{array}{ll} (1-\beta)^2 & \text{if perturber is behind the lens} \\ 1 & \text{if perturber is in the foreground} \end{array} \right\}, \tag{6}$$

where

$$\beta = \frac{D_{\mathrm{dp}} D_{\mathrm{os}}}{D_{\mathrm{op}} D_{\mathrm{ds}}}, \tag{7}$$

is a combination of angular diameter distances involving the observer (o), deflector (d), perturber (p), and source (s), where the subscripts $D_{ij} = D(z_i, z_j)$ indicate the angular diameter distance between redshifts z_1 and z_2.

This diagnostic provides a simple quantity to estimate the difference in lensed image positions caused by the leading order non-tidal (i.e. third-order) perturbation produced from a perturber. McCully et al. (2017) showed that by explicitly modeling perturbers with flexion shifts larger than the conservative limit of $\Delta_3 x > 10^{-4}{}''$, we can constrain the bias on H_0 due to this uncertainty to the percent level. We explain how the Einstein radii, $\theta_{\mathrm{E,p}}$, as well as the flexion shift uncertainties for each perturber, are determined for galaxies in §6.1.1, and for galaxy groups in §6.1.2.

We calculated the flexion shift for all galaxies in the spectroscopic survey, as well as the flexion shift of all galaxy groups identified from the survey (§6.1.2). For individual galaxies, we exclude 4 objects that are in DES Y1 Gold catalog but not in the DES Y3 Gold catalog. We also exclude 12 galaxies with spectroscopic redshifts from MUSE because they do not have DES Y3 photometry. In addition, one galaxy in the spectroscopic sample (`488065214`) was found to have bad MOF magnitudes (`MOF_CM_MAG_CORRECTED` magnitudes of -9999 for all bands), and two other galaxies (`488069251, 488066060`) were found to have bad MOF fits, with unrealistically large sizes (`MOF_CM_T` values on the order of ~5000 square arcseconds) and `MOF_CM_MAG_CORRECTED_I` magnitudes that are brighter than their `MAG_AUTO_CORRECTED_I` magnitudes by more than 4 magnitudes (18.638176 and 17.868253 com-

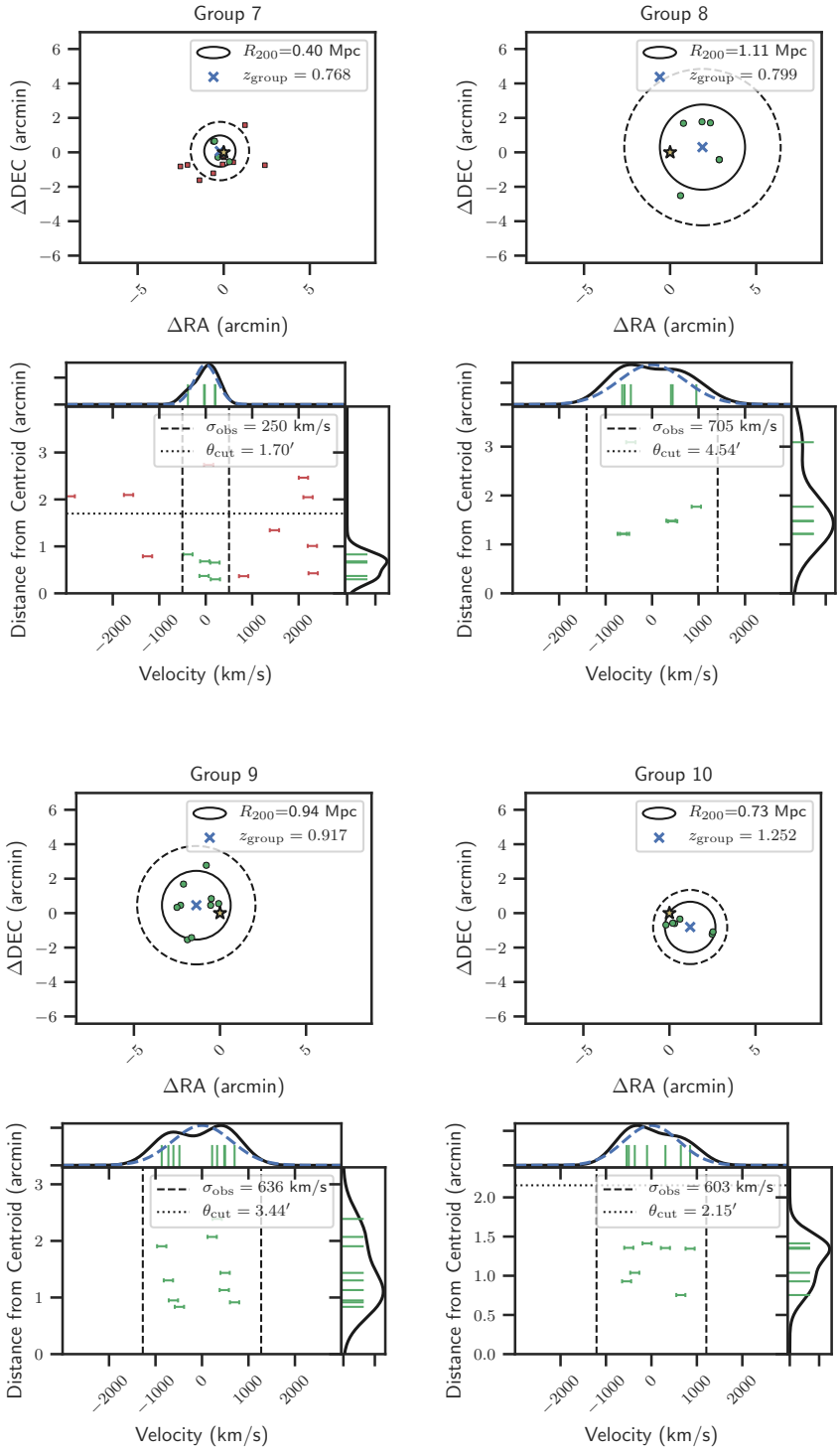

Figure 7. (continued)

pared to 23.349312 and 22.776083 respectively). For these three galaxies with spurious MOF photometry, we used the `MAG_AUTO_CORRECTED` photometry to calculate the stellar masses of these galaxies instead.

For completeness, we also calculated the flexion shifts of all likely galaxies with photometric redshift estimates in the DES "Y3 Gold" photometric catalog within 10′ of the lens galaxies, excluding galaxies that are in the spectroscopic sample. To do this, we made the following selections to the DES Y3 Gold catalog: First, we selected all objects within 10′ of the lens galaxies in the Y3 Gold catalog that satisfied `FLAGS_GOLD = 0` and `EXTENDED_CLASS_MASH_MOF`

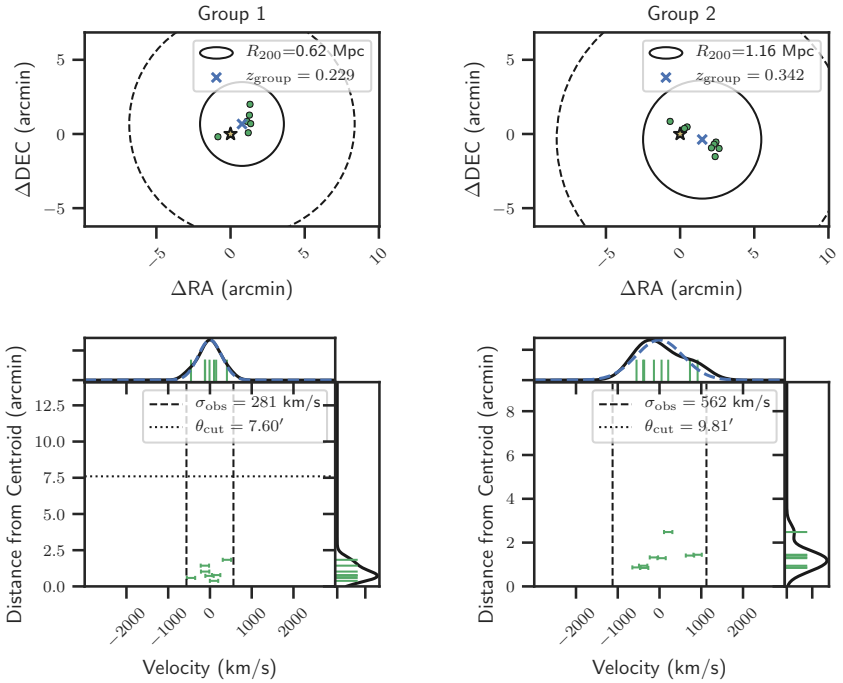

Figure 8. Galaxy groups identified using the spectroscopic sample of galaxies in the environment of WGD 2038−4008 . See Figure 7 for an explanation of the figures.

≥ 2, which selected likely galaxies. From this catalog, we excluded all galaxies that have `COADD_OBJECT_ID`s that matched galaxies already in the spectroscopic sample. We then selected objects with DNF photometric redshifts that satisfied `DNF_ZMEAN_SOF > 0` and `DNF_ZSIGMA_SOF < 10`, which removed several objects with spurious redshifts. Finally, we made the following cuts specific to the field of each lens galaxy: For DES J0408−5354 , we removed objects with `COADD_OBJECT_ID = 488068193, 488069583, 488067795`, as they are features of the lens system and not galaxies in the environment of the lens. For WGD 2038−4008 , we removed objects with `COADD_OBJECT_ID = 169192447, 169193208, 169192589, 169193438` as they are misclassified stars, and reincluded `169190696`, which is a galaxy misclassified as a star (see footnote in §2.3.2). After applying these selection criteria, we obtained a photometric catalog of 5082 objects within 10′ of DES J0408−5354 and 4438 objects within 10′ of WGD 2038−4008 . We then performed the same analysis on these objects as on the spectroscopic sample, using `DNF_ZMEAN_SOF` in lieu of spectroscopic redshift when necessary.

For the lens galaxies, we use the following quantities in our analysis: For DES J0408−5354 , we use coordinates {RA, DEC} = {62.090417, −53.899889}, lens redshift $z_{\rm d}$ = 0.59671, source redshift $z_{\rm s}$ = 2.375, and Einstein radius $\theta_{\rm E}$ = 1.80 (Lin et al. 2017; Shajib et al. 2019b). For WGD 2038−4008 , we use {RA, DEC} = {309.511379, −40.137024}, $z_{\rm d}$ = 0.22829, $z_{\rm s}$ = 0.777, $\theta_{\rm E}$ = 1.38 (Agnello et al. 2018; Shajib et al. 2019b).

6.1.1 *Individual Galaxies*

We follow the general methodology described in Sluse et al. (2019) to estimate the Einstein radii of galaxies.

First, we inferred the stellar masses of galaxies from DES photometry using the galaxy template fitting code Le PHARE (see §3.3). We then use an empirical scaling relation to estimate the line-of-sight central velocity dispersion of the galaxy, σ. In this work, we use and compare results derived from two different scaling relations, one from Zahid et al. (2016) and another from Auger et al. (2010). The Zahid et al. (2016) relation was derived from a sample of $\sim 3.7\times10^5$ SDSS elliptical galaxies at $z < 0.7$ with stellar masses in the range $\log_{10}(M_\star/M_\odot) \in [9.5, 11.5]$. The relation is fit with a broken power law given by Eqn 5 of Zahid et al. (2016), which we rewrite here in logarithmic form:

$$\begin{aligned}\log_{10}(\sigma) &= \log_{10}(\sigma_b) + \alpha_1 \left(\log_{10}(M_\star) - \log_{10}(M_b)\right) \text{ for } M_\star \le M_b \\ \log_{10}(\sigma) &= \log_{10}(\sigma_b) + \alpha_2 \left(\log_{10}(M_\star) - \log_{10}(M_b)\right) \text{ for } M_\star > M_b\end{aligned} \tag{8}$$

where $\log_{10}(\sigma_b) = 2.073$, $\log_{10}(M_b/M_\odot) = 10.26$, $\alpha_1 = 0.403$, and $\alpha_2 = 0.293$. Since Zahid et al. (2016) found no significant change of the scaling relation at different redshift bins, we assume that the stellar-mass-to-velocity-dispersion scaling relation does not evolve with redshift.

Alternatively, we also used the scaling relation from Auger et al. (2010), which was obtained from fitting a sample of 73 elliptical galaxy lenses from the SLACS survey. The best-fit relation is

$$\log_{10}(\sigma) = 0.18 \log_{10}\left(M_\star/(10^{11} M_\odot)\right) + 2.34 \tag{9}$$

where we have opted to use the best fit parameters for the model that includes the intrinsic scatter, which is 0.04 ± 0.01 in the fit. The elliptical galaxies used for this fit are generally more massive compared to the sample used in the Zahid et al. (2016) analysis, and have stellar masses in the range $\log_{10}(M_\star/M_\odot) \in [10.5, 12]$. We also assume that the stellar-mass-to-velocity-dispersion scaling relation does not evolve with redshift.

Once we obtain line-of-sight velocity dispersion estimates for each galaxy, we convert the velocity dispersion to the Einstein radius, $\theta_{\rm E,p}$, assuming a Singular Isothermal Sphere (SIS) model

$$\theta_{\rm E,p} = 4\pi \left(\frac{\sigma}{c}\right)^2 \frac{D_{\rm ps}}{D_{\rm os}} \tag{10}$$

, from which the flexion shift can be calculated with Eq.(5).

The uncertainties for the flexion shifts are calculated by adding two different sources of uncertainty in quadrature. The first source comes from the uncertainty in the stellar mass estimates from Le PHARE. The second source of uncertainty comes from the intrinsic scatter in the scaling relation between stellar mass and velocity dispersion. For the Zahid et al. (2016) relation, we quantify this uncertainty by taking half the difference in the central 68th percentile limits of the velocity dispersion distribution at a given stellar mass and use that as the uncertainty from the intrinsic scatter of the scaling relation (see Figure 9(A) of Zahid et al. 2016). For the Auger et al. (2010) relation, we use their fit for the intrinsic scatter, which is $\Delta \log_{10}(\sigma) = 0.05$ (taking the more conservative limit). The two sources of uncertainties are added in quadrature, and then propagated forward into an uncertainty in the flexion shift.

Flexion shift estimates for galaxies in the spectroscopic sample with stellar mass estimates that are significantly outside the mass ranges used to derive the Zahid et al. (2016) and Auger et al. (2010) scaling relations should be treated with caution, as the scaling relations (and errors) are extrapolated. Therefore, flexion shift estimates for galaxies in our sample with stellar masses $\log_{10}(M_\star/M_\odot) < 9.5$ should be treated with caution, as both the scaling relations from Zahid et al. (2016) and Auger et al. (2010) may not be valid at the lower end of the stellar mass range. However, the validity of this extrapolation does not affect the main results of this study, since the most significant perturbers (i.e. galaxies that contribute the largest flexion shift contributions) tend to be more massive. The 10 galaxies with the largest flexion shift contributions at the lens positions of DES J0408−5354 and WGD 2038−4008 (Table 4) are within the stellar mass ranges used to derive at least one of the two scaling relations.

6.1.2 Galaxy Groups

For galaxy-groups, we obtain a probability density function for the Einstein radius by adopting the same SIS approximation described in Eq. (10), and sampling 1000 values from the posterior PDF of the intrinsic velocity dispersion of the groups identified in §5.1 as well as from the bootstrapped PDF of the redshift of each group.

To obtain the flexion shifts of the galaxy groups and corresponding uncertainties, we use Eq. (5), sampling from the PDF of the Einstein radius as well as the bootstrapped group centroid position.

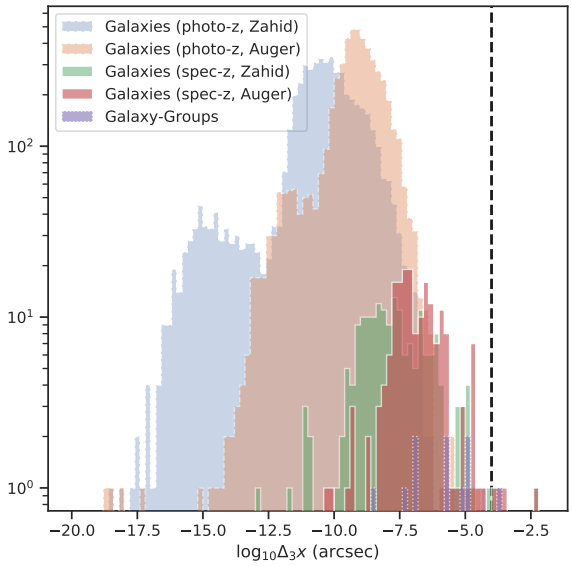

Figure 9. Flexion shift histograms for galaxies and galaxy groups in the environment of DES J0408−5354 .

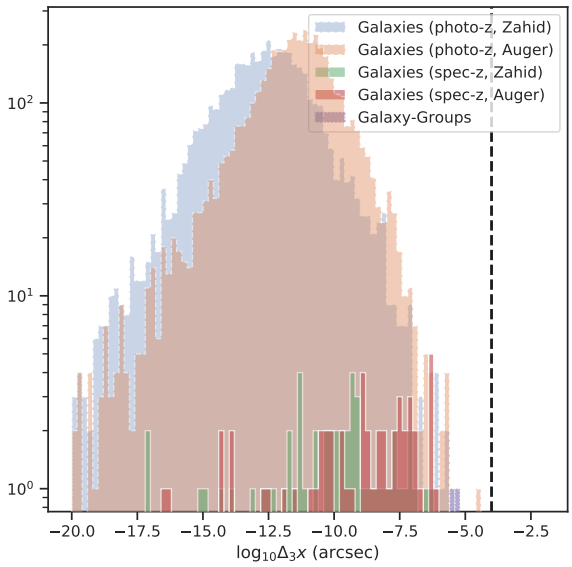

Figure 10. Flexion shift histogram for galaxies and galaxy groups in the environment of WGD 2038−4008 .

6.2 Flexion shifts for galaxies and galaxy groups in the field of DES J0408−5354 and WGD 2038−4008

We present a table of the properties of the 10 galaxies with the largest flexion shifts at the lens position in the fields of DES J0408−5354 and WGD 2038−4008 . Comparing the results from the two scaling relations, The scaling relation from Auger et al. (2010) is shallower than the fit by Zahid et al. (2016), but produces larger estimates of the line-

Table 4. Properties of the 10 galaxies with the largest flexion shifts, sorted in order of decreasing 68th percentile upper limits, in the field of DES J0408−5354 and WGD 2038−4008 . The columns display, in order, the DES Y3 Object ID (and ID used in future papers), coordinates (RA, DEC in degrees; ICRS), redshift z, distances to the lensing galaxy and flexion shifts, calculated using the scaling relations by Zahid et al. (2016) and Auger et al. (2010) respectively. Galaxies marked with ∗ are not in the spectroscopic survey and only have photometric redshifts; we report the `DNF_ZMEAN_SOF` redshift value and `DNF_ZSIGMA_SOF` uncertainties. Spectroscopic redshift uncertainties are about 100 km s^{-1}, or 0.00033 in redshift. Stellar masses and corresponding uncertainties were calculated using the `Le PHARE` galaxy template fitting code and DES Y3 photometry (see §3.3). Galaxies marked with † have spurious `MOF` magnitudes. For these galaxies, we use `MAG_AUTO_CORRECTED` photometry to calculate stellar masses instead. Flexion shifts and uncertainties are calculated following the method described in §6.1-6.1.1. For a complete list of galaxies, see Table A1

ID	RA (deg)	DEC (deg)	z	i-band Magnitude	$\log_{10}(M_*)$ ($log_{10}(M_\odot)$)	$\Delta\theta$ (arcsec)	$\log_{10}(\Delta_3 x_{\rm Zahid})$ ($\log_{10}$(arcsec))	$\log_{10}(\Delta_3 x_{\rm Auger})$ ($\log_{10}$(arcsec))
				DES J0408−5354				
488068102 (G3)	62.090965	-53.901634	0.76866	20.096	$11.42^{+0.10}_{-0.12}$	6.4	$-2.21^{+0.25}_{-0.29}$	$-2.20^{+0.21}_{-0.22}$
488065185 (G6)	62.095575	-53.898291	0.59441	21.867	$10.29^{+0.10}_{-0.17}$	12.4	$-3.95^{+0.42}_{-0.58}$	$-3.42^{+0.21}_{-0.24}$
488066144 (G4)	62.090243	-53.903609	0.77069	22.015	$10.66^{+0.13}_{-0.17}$	13.4	$-4.07^{+0.38}_{-0.51}$	$-3.72^{+0.22}_{-0.24}$
488066768 (G5)	62.092923	-53.900091	1.03197	23.682	$9.68^{+0.24}_{-0.25}$	5.4	$-4.93^{+0.63}_{-0.93}$	$-3.87^{+0.26}_{-0.27}$
488066462	62.083912	-53.903969	0.60048	22.304	$9.88^{+0.12}_{-0.19}$	20.2	$-5.24^{+0.52}_{-0.79}$	$-4.37^{+0.22}_{-0.25}$
MUSE6 / 488065214 †	62.077898	-53.903878	0.59797	22.303	$10.37^{+0.11}_{-0.16}$	30.2	$-5.02^{+0.41}_{-0.56}$	$-4.53^{+0.21}_{-0.23}$
488070148	62.084648	-53.885204	0.27247	18.309	$10.99^{+0.04}_{-0.04}$	54.3	$-4.81^{+0.31}_{-0.37}$	$-4.61^{+0.20}_{-0.20}$
488066886	62.090541	-53.904725	0.77568	22.925	$9.91^{+0.16}_{-0.30}$	17.4	$-5.46^{+0.53}_{-0.90}$	$-4.61^{+0.23}_{-0.30}$
488070807	62.072770	-53.910296	0.59811	19.975	$11.27^{+0.05}_{-0.06}$	53.0	$-4.69^{+0.25}_{-0.30}$	$-4.61^{+0.20}_{-0.21}$
MUSE8 / 488067782	62.103108	-53.897861	0.59832	22.100	$10.11^{+0.13}_{-0.20}$	27.9	$-5.29^{+0.48}_{-0.71}$	$-4.62^{+0.22}_{-0.25}$
				WGD 2038−4008				
169192350 ∗	309.514393	-40.137815	0.349 ± 0.033	21.999	$9.53^{+0.15}_{-0.29}$	8.8	$-5.71^{+0.59}_{-1.03}$	$-4.52^{+0.22}_{-0.30}$
169193255 ∗	309.529391	-40.151522	0.240 ± 0.138	18.806	$10.76^{+0.06}_{-0.10}$	72.0	$-5.94^{+0.35}_{-0.45}$	$-5.63^{+0.20}_{-0.21}$
169190952 ∗	309.503723	-40.120144	0.277 ± 0.021	19.052	$10.78^{+0.05}_{-0.09}$	64.3	$-6.02^{+0.34}_{-0.44}$	$-5.72^{+0.20}_{-0.21}$
169192931 ∗	309.508988	-40.144869	0.421 ± 0.044	20.446	$10.62^{+0.05}_{-0.07}$	29.0	$-6.17^{+0.37}_{-0.47}$	$-5.80^{+0.20}_{-0.21}$
169191098 ∗	309.487406	-40.124006	0.238 ± 0.016	18.360	$10.69^{+0.04}_{-0.03}$	80.9	$-6.16^{+0.36}_{-0.45}$	$-5.82^{+0.20}_{-0.20}$
169191973 ∗	309.536238	-40.134562	0.331 ± 0.011	18.444	$11.15^{+0.03}_{-0.03}$	69.0	$-6.05^{+0.27}_{-0.33}$	$-5.92^{+0.20}_{-0.20}$
169193929 ∗	309.520149	-40.160086	0.250 ± 0.005	19.137	$10.63^{+0.05}_{-0.09}$	86.5	$-6.41^{+0.36}_{-0.47}$	$-6.04^{+0.20}_{-0.21}$
169190452	309.539131	-40.115839	0.22917	18.213	$10.76^{+0.04}_{-0.04}$	107.9	$-6.39^{+0.35}_{-0.43}$	$-6.08^{+0.20}_{-0.20}$
169192596	309.492815	-40.140131	0.23003	21.389	$9.28^{+0.11}_{-0.18}$	52.3	$-7.61^{+0.60}_{-0.96}$	$-6.21^{+0.21}_{-0.24}$
169191228	309.535586	-40.122881	0.22900	20.025	$10.13^{+0.07}_{-0.11}$	83.9	$-6.86^{+0.45}_{-0.62}$	$-6.21^{+0.21}_{-0.22}$

Note: ∗ Galaxy is not in the spectroscopy survey; stellar masses and flexion shift estimates are from photometric redshifts.
† Galaxy has spurious `MOF` photometry. For these galaxies, we use `MAG_AUTO_CORRECTED` photometry to calculate stellar masses instead.

of-sight velocity dispersion for galaxies with stellar masses $\log_{10}(M_\star/M_\odot) \lesssim 11.45$. Since the majority of galaxies in the sample have smaller stellar mass estimates than that, the Auger et al. (2010) scaling relation produces larger flexion shifts than that from the Zahid et al. (2016) for this sample, and can be treated as the more conservative estimate of the two. In figures 9 and 10, we show the distribution of flexion shifts of the spectroscopic and photometric catalogs for the environment of DES J0408−5354 and WGD 2038−4008 , using both the Zahid et al. (2016) and Auger et al. (2010) scaling relations. The $\log_{10}(\Delta_3 x) > -4$ criteria is indicated by the dashed vertical line.

When calculating flexion shifts for the photometric catalog, we found some objects with spurious `MOF_CM_MAG_CORRECTED` photometry. For these objects we instead used stellar masses computed from `MAG_AUTO` photometry, including the same Milky Way extinction and other photometric corrections as for the MOF magnitudes.

Using this criterion, for DES J0408−5354 , there are four galaxies (G3, G4, G5, G6) with flexion shift contributions above $\log_{10}(\Delta_3 x) > -4$ when using the stellar masses from the Auger et al. (2010) scaling relation. These four galaxies are explicitly modeled in the‘ lens model analysis (Shajib et al. 2019a). In addition, the group including the lensing galaxy, group 5, has a flexion shift of $-3.86^{+0.97}_{-0.72}$ ″. The large uncertainties in the flexion shift of group 5 is due to a combination of the close proximity of the group centroid to DES J0408−5354 and the uncertainty in the centroid location, with the upper limits of the flexion shift being produced when the group centroid is near the lens galaxy.

For WGD 2038−4008 , we did not identify any galaxies or galaxy groups with a flexion shift $\log_{10}(\Delta_3 x) > -4$.

6.3 Photometrically Identified Galaxy-Groups

6.3.1 RedMaPPer Clusters in the Field of the Lenses

Due to the low spectroscopic completeness of the survey of WGD 2038−4008 , we complemented our spectroscopic group-identification efforts with a search of all photometrically-identified clusters with richness $\lambda >$

5 in the field of view of WGD 2038−4008 using the redMaPPer algorithm Rykoff et al. (2014). We used the sixth release of the redMaPPer cluster catalog on DES Y3A2 data (v6.4.22+2) and found two redMaPPer clusters within 3′ of WGD 2038−4008 (with unique IDs `MEM_MATCH_ID = 62659, 138669`).

One of the clusters (`62659`) has a photometric cluster redshift of $z_{\rm photo} = 0.221 \pm 0.008$ and a richness of $\lambda = 5.1 \pm 1.7$. The photometric cluster redshift of cluster `62659` is consistent with the spectroscopically-identified Group 1 ($z_{\rm group} = 0.229$), and its algorithmically-identified central galaxy, `COADD_OBJECT_ID = 169190452`, is also a member of Group 1 (see Table A2), suggesting that redMaPPer cluster `62659` and Group 1 are the same group. Only two of the seven spectroscopically-identified group members in Group 1 (`COADD_OBJECT_ID = 169190452, 169189459`) are also members of the redMaPPer cluster `62659`. However, this could be simply due to bad photometric redshift estimates, as 4 of the 5 group members have `DNF_ZMEAN_SOF` photometric redshift estimates that range from 0.38 − 0.44, and the lens galaxy (`169191076`) has a spurious redshift estimate of 0.00977.

The second redMaPPER cluster (`138669`) has a cluster redshift of $z_{\rm photo} = 0.405 \pm 0.017$ and a richness of $\lambda = 10.8 \pm 2.0$. None of the galaxies in this cluster share group membership with the spectroscopically-identified Group 2, suggesting that this group is distinct from Group 2.

For completeness, we also searched for redMaPPer clusters in the field of DES J0408−5354 , though the spectroscopic completeness of the field of DES J0408−5354 is much higher than that of WGD 2038−4008 . However, we did not find any clusters within 3′of DES J0408−5354 . One reason for this paucity is that a nearby region of the lens has been flagged and precluded from redMaPPer analysis due to a bright star in the foreground.

6.3.2 *Flexion Shifts for redMaPPer Clusters near the lenses*

We performed the same flexion shift calculations on the redMaPPer clusters as the spectroscopic groups, following the procedure outlined in §6.1, using the same lens parameter quantities, and using the same conservative SIS approximation described by Eq. 10 for the perturber. We use the scaling relation given by Eq. (17) of Andreon & Hurn (2010) to convert the cluster richness into a velocity dispersion estimates for the SIS model. From this, we obtain flexion shifts for the redMaPPer clusters. For cluster `62659`, we obtain a flexion shift of $\log_{10}(\Delta_3 x) = -5.1^{+0.3}_{-0.4}$. For cluster `138669`, we obtain a flexion shift of $\log_{10}(\Delta_3 x) = -6.0 \pm 0.2$. The estimated uncertainties come from propagating both the uncertainties in cluster richness, as well as the uncertainties in the scaling relation. The properties of both groups are summarized in Table A3. Neither redMaPPer groups in the field of WGD 2038−4008 exceeds the threshold of $\log_{10}(\Delta_3 x) > -4$.

7 DETERMINING LINE-OF-SIGHT UNDER/OVERDENSITIES USING WEIGHTED NUMBER COUNTS

7.1 Description of the technique

To determine the line-of-sight under/overdensities we follow the technique described in section 5 of Rusu et al. (2017). Like the CFHTLens control fields used in Rusu et al. (2017), the DES fields also have saturated stars and other artifacts that are masked. Each DES coadd tile contains a mask plane that contains the bleed trails for the saturated stars but not the mask for the stars themselves. The masks for the stars and other artifacts such as dead CCD regions are contained in the `mangle` masks (Swanson et al. 2008; Hamilton & Tegmark 2004) that are computed by DESDM for each tile. As can be seen from the upper image in Figure 3 there is a large saturated star in the DES J0408−5354 field close to the lens. The $i-$band and $z-$band `mangle` masks defined a very large mask around this star such that the entire 1000×1000 pixel area around the lens was masked. We therefore chose to use the `mangle` masks for the $r-$band images for both the target field and the control fields which did not have this problem. We also chose to use the r-band mask for WGD 2038−4008 for consistency. For each field (target and control) we combine the mask plane and the `mangle` mask to obtain the complete mask. We also use a 5.26″radius mask at the center of the DES J0408−5354 target field and a 2.63″radius mask for WGD 2038−4008 to remove the lensing galaxy and quasar images from the calculation. We then apply each control field mask to the target field and apply the target field mask to each control field, as described in section 5.1 of Rusu et al. (2017). Following the example of (Rusu et al. 2019), for DES J0408−5354 we are manually removing from the target field catalogue four galaxies that are incorporated in the mass models of Shajib et al. (2019a), in order to avoid double-counting their contribution to $\kappa_{\rm ext}$.

We compute the median of the weighted counts for the target field $W_q^{meds,t} = N^t_{gal} \times median(q^t_i)$, where q_t is the chosen weighting scheme, with $i = 1, ..., N^t_{gal}$ and N^t_{gal} is the number of galaxies in the aperture. We compute the same quantity for the control field $W_q^{meds,c} = N^c_{gal} \times median(q^c_i)$. For each target field and control field combination we calculate the ratio $\zeta_q = W_q^{meds,t}/W_q^{meds,c}$ for each target and control field combination. Our final weighted count for weighting scheme q is the median of this ratio over all target/control field combinations $\overline{\zeta_q^{meds}}$.

We focus on four weighting schemes we used in Birrer et al. (2019), $q = 1$ which is just the raw counts N^t_{gal}/N^c_{gal}, weighting by redshift $q_z = z_s \times z_i - z_i^2$, weighting by distance to the lens/center of the field $q_r = 1/r$ and weighting by distance to the lens/center of the field and redshift $q_{z/r} = (z_s \times z_i - z_i^2)/r$. We have used two apertures, one of radius 120″ and the other of radius 45″. In Figure 11 and Figure 12 we show the relative weights of each galaxy in the DES J0408−5354 and WGD 2038−4008 fields for $i < 22.5$ and the two apertures 120″ and 45″.

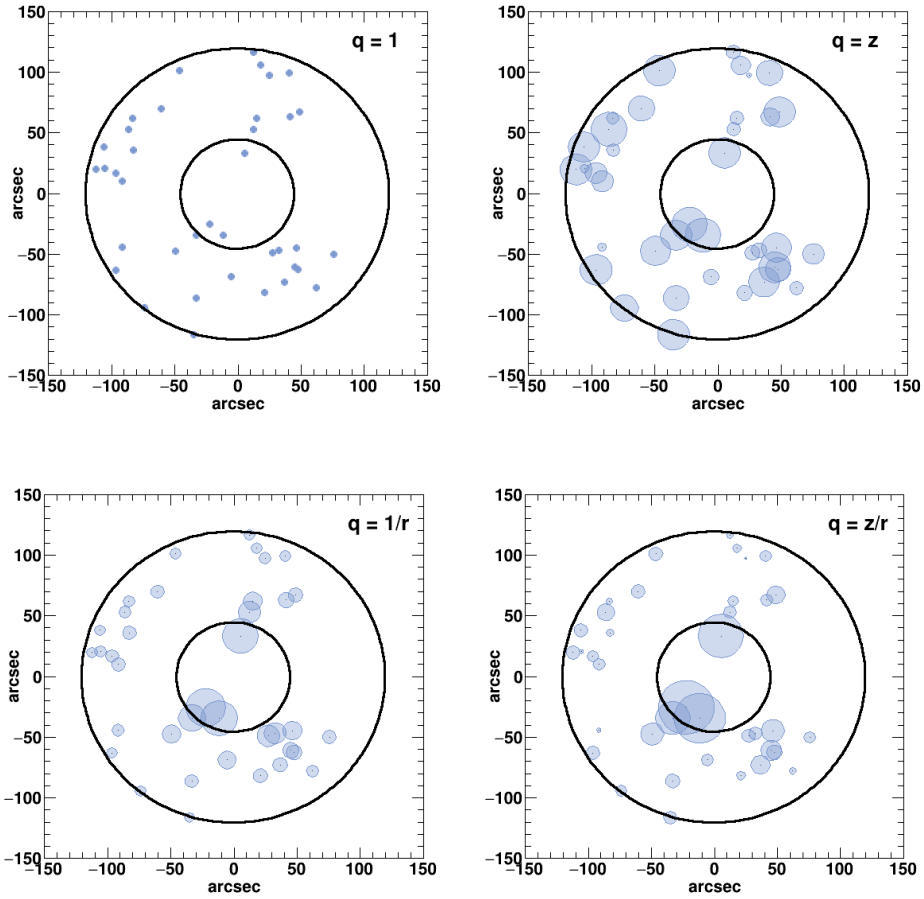

Figure 11. The relative weights of the galaxies around DES J0408−5354 for the four weighting schemes $q = 1$, $q_z = z_s \times z_i - z_i^2$, $q_r = 1/r$ and $q_{z/r} = (z_s \times z_i - z_i^2)/r$. The galaxies satisfy $i < 22.5$ and are represented by circles with areas proportional to their weights. The black circles indicate the 120″and 45″apertures.

7.2 Resulting distribution for ζ_q

We present our results for $\overline{\zeta_q^{meds}}$ in Table 5. The uncertainties are derived from taking 20 samplings of the redshift and magnitude errors from a Gaussian PDF distribution corresponding to each galaxy. We show the results for both apertures and for both the DNF and BPZ redshift selections. In Figure 13 we show the ratio ζ_q^{meds} for the four weighting schemes for both DES J0408−5354 and WGD 2038−4008 . Figure 14 shows a radial plot of the measured over/underdensity for each weight for four different aperture radii: 45″, 60″, 90″ and 120″ for both DES J0408−5354 and WGD 2038−4008 . Our analysis shows that the field of DES J0408−5354 is significantly under-dense (more so than any of the existing H0LiCOW lenses), and this is expected to lead to a tight, negative-value distribution of $\kappa_{\rm ext}$ (e.g., Greene et al. 2013). On the other hand the field of WGD 2038−4008 is of about unit density in the 45″-aperture, and over-dense in the 120″-aperture compared to the random fields.

7.3 Computing simulated ζ_q in the MS

We follow the approached described in Rusu et al. (2017), in order to implement the same observational constraints to the galaxies in the MS as are relevant to the computation of ζ_q in the DES data. MS is a dark matter-only simulation of the ΛCDM cosmology, having a periodic box of 500 h^{-1}Mpc on a side with $2160^3 \approx 1.0078 \times 10^{10}$ particles. The simulation run was performed with a modified version of the GADGET-2 code Springel et al. (2005); Lemson & Virgo Consortium (2006) and has the spatial resolution limit of $5h^{-1}$kpc (Plummer-equivalent). The mass resolution $8.6 \times 10^8\, h^{-1} M_\odot$ and the volume are enough to include a large variety of well-resolved objects from faint quasars to galaxy-clusters. Galaxies can be painted onto these dark matter-only halos using semi-analytical models. Previous H0LiCOW work has employed the models by De Lucia & Blaizot (2007), but here we are also exploring, for comparison, the newer models of Henriques et al. (2015). The assignment of these galaxies to halos follows different physical prescriptions, which are adjusted to fit typically low redshift observables. The available catalogues contain synthetic photometry in various bands; we select the *griz* magnitudes for each galaxy, and sample from them by assigning uncertain-

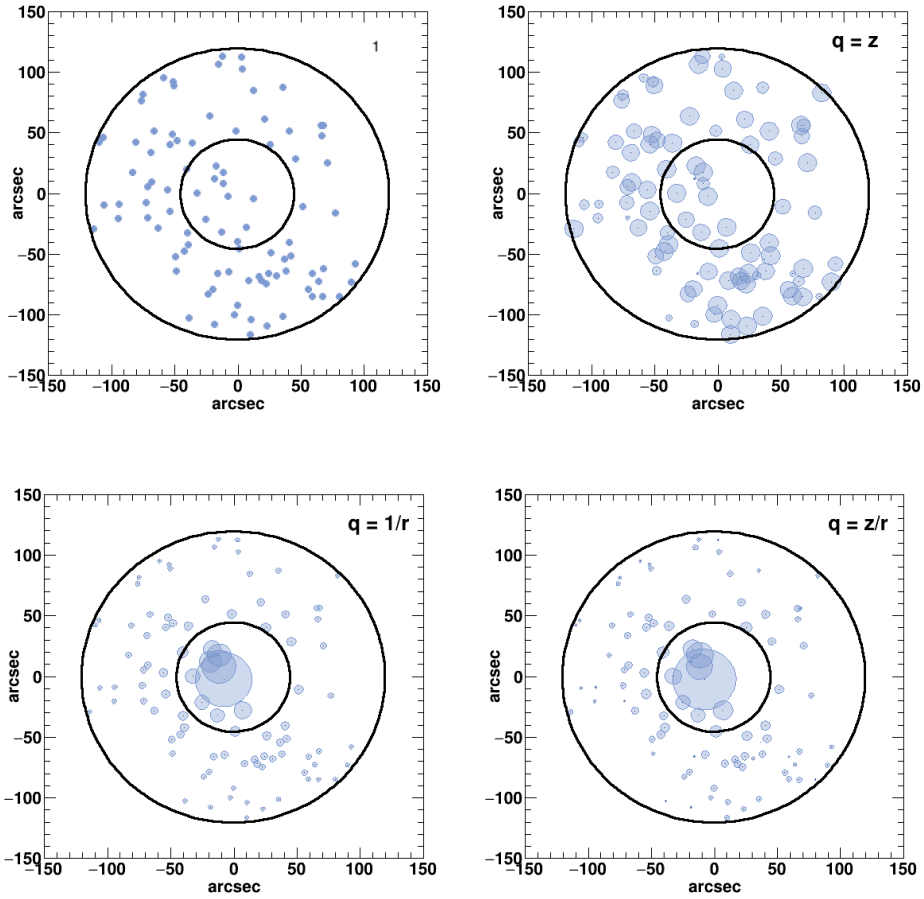

Figure 12. The relative weights of the galaxies around WGD 2038−4008 for the four weighting schemes $q = 1$, $q_z = z_s \times z_i - z_i^2$, $q_r = 1/r$ and $q_{z/r} = (z_s \times z_i - z_i^2)/r$. The galaxies satisfy $i < 22.5$ and are represented by circles with areas proportional to their weights. The black circles indicate the 120″and 45″apertures.

ties taken from observed DES galaxies, over the same range of magnitude bins. We account for the fraction of galaxies in the target fields that have available spectroscopy, and also for the known DES galaxy-star contamination and incompleteness fractions. The latter fractions are corrected to account for the fraction of the target field apertures covered by *HST*, as *HST* imaging is assumed to result in the most reliable classification.

In Figure 15 we plot the resulting comparison of photometric redshifts and catalogue redshifts for a representative sample of the De Lucia & Blaizot (2007) and Henriques et al. (2015) galaxies, up to the redshift of DES J0408−5354 (including for the redshift limit of WGD 2038−4008). Our photometric redshifts measured with BPZ have negligible bias up to a redshift of $z \sim 1$, above which there is significant scatter, due to the absence of infrared photometry beyond $z-$band. For the De Lucia & Blaizot (2007) models this is a small effect, as there are very few galaxies above this redshift (Figure 16), but the effect may be more pronounced for the Henriques et al. (2015) models, which predict a significant number of galaxies at large redshift.

8 DETERMINING $P(\kappa_{\rm EXT})$

Our method of obtaining $P(\kappa_{\rm ext})$ relies on selecting lines of sight from the MS which match the observed ζ_q constraints, and constructing the PDF of their associated $\kappa_{\rm ext}$ distributions, using the $\kappa_{\rm ext}$ maps produced by the ray tracing technique of Hilbert et al. (2009). This method has been described in detail in Rusu et al. (2017), and updated in Birrer et al. (2019) and Rusu et al. (2019). One point we wish to emphasize is that when we computed the relative over/underdensity of the DES J0408−5354 lens fields in Section 7.1 we removed individual galaxy perturbers that were explicitly incorporated into the lens modeling. By doing so, we ensure that these galaxies do not contribute to the $P(\kappa_{\rm ext})$ we estimate, and we therefore avoid biasing our estimate high. This is accomplished without the need to alter the input $\kappa_{\rm ext}$ maps.

Furthermore, we have shown in Section 6.2 that the group of galaxies at the redshift of the lens in DES J0408−5354 contributes a flexion shift close to our threshold for incorporating this structure into the mass models. We therefore compute $P(\kappa_{\rm ext})$ for two cases. In the first case, "w/ group", we ignore the existence of this structure, and we include the LOS contribution of the constituent

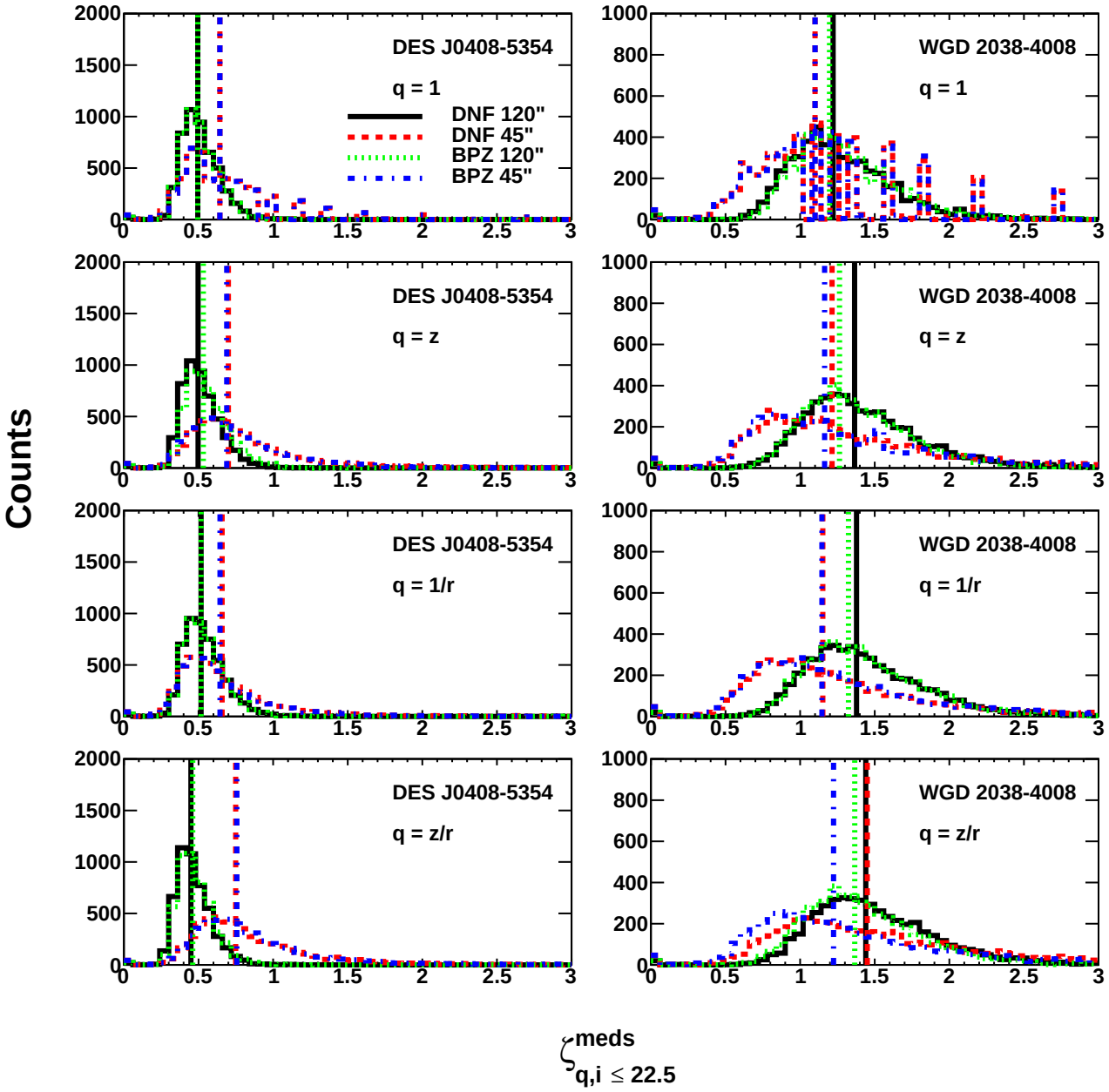

Figure 13. The histograms of the weighted ratios for all ζ_q^{meds} for DES J0408−5354 and WGD 2038−4008 . The vertical lines mark the median of the corresponding distributions. Black solid line - 120″ aperture and DNF redshifts. Green dotted line - 120″ aperture and BPZ redshifts. Red dashed line - 45″ aperture and DNF redshifts. Blue dashed-dotted line - 45″ aperture and BPZ redshifts.

galaxies to $P(\kappa_{\rm ext})$. In the second case, "w/o group", we expect that the structure will be included in the lensing models of Shajib et al. (2019a), Yildirim et al. in prep. and Wong et al. in prep, and we therefore exclude it from the LOS analysis. This is accomplished by removing the galaxy group members from the catalogue of galaxies around the lens, when computing the weighted count ratio constraints reported in Table 5. We adopt the technique from Rusu et al. (2019) and Chen et al. (2019) to account for spectroscopic incompleteness. That technique consists of two different methods, one which uses the Andreon & Hurn (2010) relation between group velocity dispersion and richness, and one which assumes Poisson statistics to compute the number of additional galaxy members potentially missed due to sparse spec-

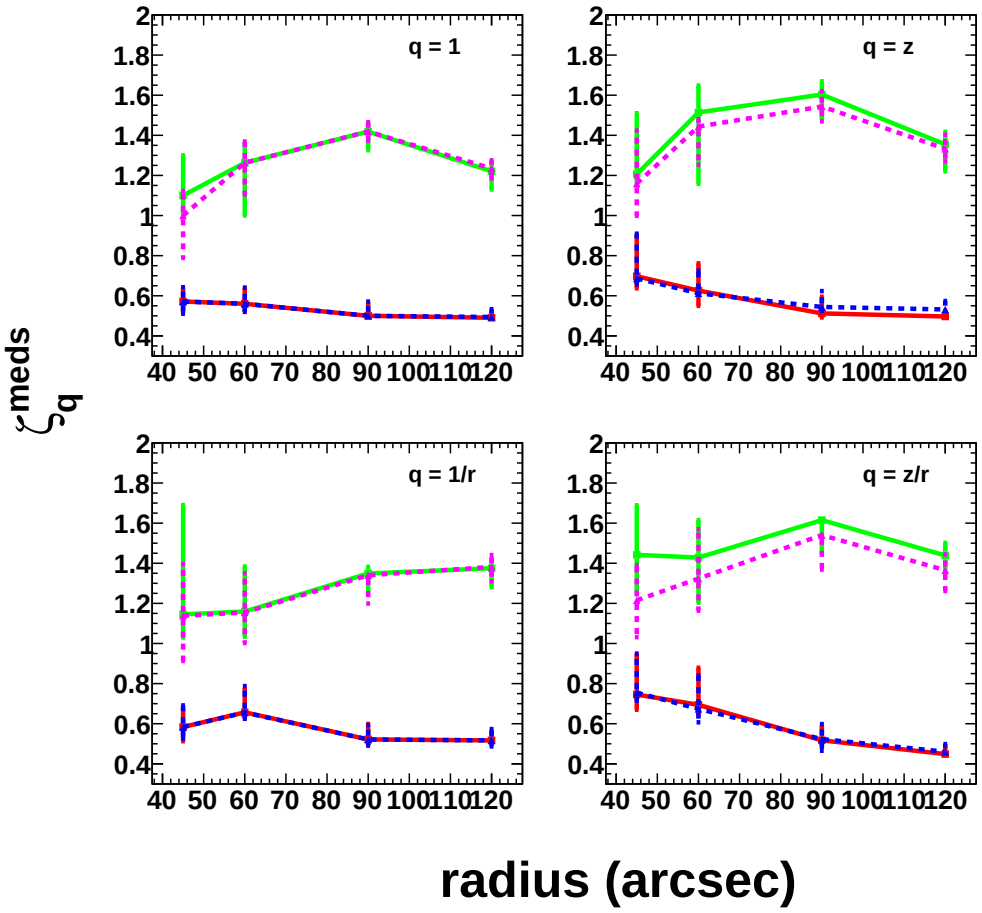

Figure 14. Radial plots of the measured weighted count ratios ζ_q^{meds} calculated for aperture radii of 45″, 60″, 90″ and 120″. DES J0408−5354 : Red - DNF photometric redshifts, Blue - BPZ photometric redshifts. WGD 2038−4008 : Green - DNF photometric redshifts, Magenta - BPZ photometric redshifts

troscopy. We choose to use only the second method, as the first relies on numerous physical assumptions, and cannot reconcile the small velocity dispersion of the group (∼ 230 km/s) with the large number of observed members (17). We found a similar mismatch between the two methods in Chen et al. (2019) for the lens PG 1115+080.

In Figures 17 and 18 we plot the resulting distributions of $P(\kappa_{\rm ext})$ for DES J0408−5354 and WGD 2038−4008 , respectively, for a selection of weights, using the De Lucia & Blaizot (2007) galaxy models. The ζ_q constraints are taken from Table 5, where we marginalize over the DNF and BPZ values. As in Birrer et al. (2019); Rusu et al. (2019), we combine the ζ_q constraints from the 45″and 120″apertures. We consider as fiducial distributions, to be used in the cosmological analysis, the ones which use as constraints the most robust ζ_q constraints, i.e. those with $q = 1$ and $q = 1/r$ in both apertures. In previous work we also used the external shear values corresponding to the best-fit mass models as an additional constraint. At the time our analysis was completed, the final shear values from Yildirim et al. in prep. and Wong et al. in prep, which will complement the cosmographic inference of Shajib et al. (2019a), as well as for WGD 2038−4008 , were unknown. Therefore, we choose to report the statistics of $P(\kappa_{\rm ext}|\zeta_1^{45''}, \zeta_{1/r}^{45''}, \zeta_1^{120''}, \zeta_{1/r}^{120''}, \gamma)$ for a variety of γ values, in Table 6.

For the choices in Figure 17, we found that the use of the Henriques et al. (2015) models results in $P(\kappa_{\rm ext})$ lower by $\kappa_{\rm ext} \lesssim 0.01$, therefore at the $\lesssim 1\%$ level. Based on the fact that the photometric redshift distribution of the DES galaxies in Figure 16 is more consistent with that of the De Lucia & Blaizot (2007) models (e.g., the large peak at $z \sim 0.5$ and the absence of galaxies above $z \sim 1.5$), as well as for consistency with our previous work on H0LiCOW lenses, we adopt the De Lucia & Blaizot (2007) models. We will test in more detail the impact of a particular choice of semi-analytical galaxy models, which appears to be comparatively larger for large source redshifts and over/under-densities, in another work, Mukherjee et al., in prep.

As expected from the significantly underdense field of

Table 5. Weighted galaxy count ratios $\overline{\zeta_q}$ for DES J0408−5354 and WGD 2038−4008 .

Weight q	45″ $i < 22.5$ DNF	120″ $i < 22.5$ DNF	45″ $i < 22.5$ BPZ	120″ $i < 22.5$ BPZ
DES J0408−5354 w/ group				
1	$0.643^{+0.071}_{-0.06}$	$0.495^{+0.029}_{-0.01}$	$0.643^{+0.071}_{-0.06}$	$0.495^{+0.039}_{-0.01}$
z	$0.7^{+0.207}_{-0.06}$	$0.497^{+0.029}_{-0.017}$	$0.689^{+0.223}_{-0.029}$	$0.532^{+0.042}_{-0.01}$
$1/r$	$0.658^{+0.095}_{-0.071}$	$0.517^{+0.048}_{-0.018}$	$0.644^{+0.108}_{-0.057}$	$0.517^{+0.056}_{-0.03}$
z/r	$0.749^{+0.204}_{-0.076}$	$0.449^{+0.033}_{-0.009}$	$0.757^{+0.193}_{-0.04}$	$0.461^{+0.038}_{-0.011}$
DES J0408−5354 w/o group				
1	$0.286^{+0.298}_{-0.209}$	$0.388^{+0.068}_{-0.068}$	$0.286^{+0.214}_{-0.209}$	$0.388^{+0.058}_{-0.068}$
z	$0.389^{+0.376}_{-0.288}$	$0.373^{+0.100}_{-0.106}$	$0.394^{+0.278}_{-0.287}$	$0.388^{+0.093}_{-0.10}$
$1/r$	$0.282^{+0.306}_{-0.207}$	$0.370^{+0.085}_{-0.070}$	$0.282^{+0.230}_{-0.207}$	$0.368^{+0.081}_{-0.069}$
z/r	$0.379^{+0.346}_{-0.278}$	$0.342^{+0.065}_{-0.079}$	$0.391^{+0.276}_{-0.286}$	$0.345^{+0.068}_{-0.076}$
WGD 2038−4008				
1	$0.90^{+0.20}_{-0.10}$	$1.169^{+0.039}_{-0.052}$	$0.833^{+0.556}_{-0.167}$	$1.184^{+0.066}_{-0.064}$
z	$1.066^{+0.191}_{-0.123}$	$1.286^{+0.061}_{-0.055}$	$0.919^{+0.084}_{-0.154}$	$1.237^{+0.078}_{-0.065}$
$1/r$	$0.943^{+0.494}_{-0.114}$	$1.288^{+0.046}_{-0.065}$	$0.881^{+0.059}_{-0.164}$	$1.296^{+0.060}_{-0.077}$
z/r	$1.187^{+0.150}_{-0.131}$	$1.362^{+0.083}_{-0.115}$	$0.999^{+0.144}_{-0.131}$	$1.278^{+0.123}_{-0.116}$

DES J0408−5354 , the resulting fiducial $P(\kappa_{\rm ext})$ distributions are tight (approximately 0.03 width in $\kappa_{\rm ext}$), with medians around $\kappa_{\rm ext} \sim -0.04$ - -0.05, or 4 - 5%.[5] As the group contribution is removed from the LOS, $P(\kappa_{\rm ext})$ decreases by $\lesssim 0.01$.

The distributions for WGD 2038−4008 are much tighter, with width $\sim$ 1%. This is expected due to the significantly lower source redshift, as there are fewer structures in the MS along the LOS to contribute convergence. The tightening of the distributions as information from multiple apertures is used is evident (see also Figure E2 in Rusu et al. 2019). The medians of the distributions are close to null.

Appendix C of Rusu et al. (2017) shows that our use of the MS to derive $P(\kappa_{\rm ext})$ can bias the inference because of the different set of assumed cosmological parameters. However, since our $P(\kappa_{\rm ext})$ is close to zero, the expected value of the bias, if we assume the cosmological parameters derived from *Planck* (e.g., Planck Collaboration et al. 2016), is at a level of $\sim$ 0.5%, below the 1% level of accuracy currently aimed at from time delay cosmography (Suyu et al. 2017).

[5] The distributions of $P(\kappa_{\rm ext})$ presented in this paper differ slightly from the ones used in the blind cosmographic analysis of DES J0408−5354 by Shajib et al. (2019a). In addition to that work using the shear constraint derived therein, there is a minor difference owing to a clerical error discovered after unblinding, which corresponds to a change in H_0 of 0.13%, much smaller than the statistical uncertainty of 3.9%. In order to preserve the blindness of the H_0 measurement, this correction has not been propagated through the Shajib et al. (2019a) measurement. However, future measurements based on DES J0408−5354 should use the corrected distribution of $P(\kappa_{\rm ext})$ given in this paper.

9 CONCLUSIONS

In this paper we have presented work on three of the ingredients that are necessary to make a high-precision measurement of the Hubble constant H_0 using the lensed quasars DES J0408−5354 and WGD 2038−4008 . These are 1) determining the velocity dispersion of the lensing galaxy, 2) identifying galaxies and groups along the line of sight that are close enough to the lens and massive enough that they need to be included in the mass model, and 3) estimating the external convergence $\kappa_{\rm ext}$ due to less massive structures that do not need to be included explicitly in the mass model. These ingredients require spectroscopic redshifts for the galaxies in the fields of the two lenses. To obtain these we have carried out spectroscopic observations using Gemini South/GMOS-S, Magellan/LDSS-3 and VLT/MUSE. As detailed in §3.1-3.2, we obtained a total of 199 high-confidence redshifts from the three instruments for DES J0408−5354 , corresponding to a redshift completeness of 68% for galaxies with $18 \leq i < 23$ and $5'' \leq$ radius $< 3'$. For WGD 2038−4008 we obtained 54 high-confidence redshifts from the Gemini South/GMOS-S data, with a 16% redshift completeness for the same i-band magnitude and radius ranges.

As described in §4, in our redshift survey observations we also set aside slits to measure the stellar velocity dispersions of the main lensing galaxies in our two systems. The velocity dispersion of the main deflector G1 in DES J0408−5354 was measured using four independent spectra from the above three instruments, with a consistent result of about 230 km s^{-1} (see Table 2). The velocity dispersion for the main lensing galaxy G in WGD 2038−4008 was obtained from one spectrum taken using Gemini South/GMOS-S, with a resulting value of about

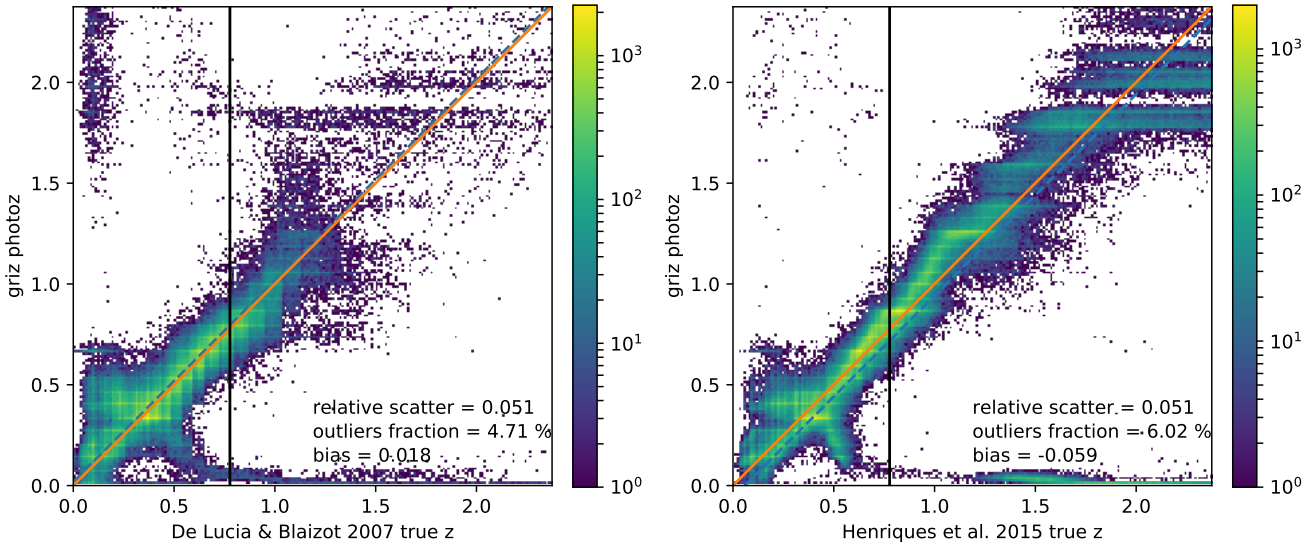

Figure 15. Comparison of catalogue versus photometric redshifts computed for a representative fraction of the MS galaxies painted over the dark matter halos, using the De Lucia & Blaizot (2007) *(left)* and Henriques et al. (2015) *(right)* semi-analytical galaxy models and resulting synthetic photometry. The photometric redshifts are computed using BPZ, with the errors on the photometry being representative of the DES measurement uncertainties for similar magnitudes. The limiting magnitude used is $i < 22.5$ mag. The orange orange solid line marks the true z = photoz identity, and the blue dashed line marks the best linear fit. The plotting range extends to the redshift of DES J0408−5354 . The vertical black line marks the redshift of WGD 2038−4008 . For this lower redshifts, the scatter, fraction of outliers and bias become 0.051 (0.050 for Henriques et al. (2015)), 4.26% (3.08%) and 0.023 (−0.005), respectively.

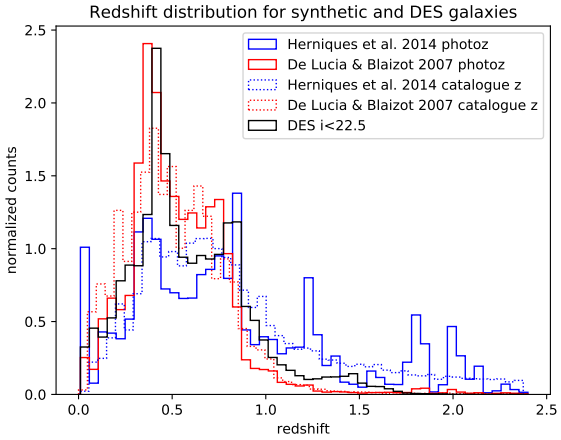

Figure 16. Histograms of the catalogue and BPZ-based photometric redshift distributions for a representative fraction of ∼ 500000 galaxies in the MS, using the semi-analytical models of De Lucia & Blaizot (2007) and Henriques et al. (2015). The BPZ-based photometric redshift distribution for a similar number of DES galaxies, down to the same $i < 22.5$ mag limit, is also shown.

300 km s^{-1}. The detailed velocity dispersion measurements and uncertainties are given in Table 2.

The galaxy group identification uses the spectroscopic redshifts described above and the same algorithm that was used for the analysis of the H0LiCOW lenses HE 0435−1223 (Sluse et al. 2017) and WFI 2033−4723 (Sluse et al. 2019). We find 10 galaxy groups in DES J0408−5354 for which we then compute the flexion shift $\Delta_3 x$ proposed by McCully et al. (2017). McCully et al. (2017) showed that explicitly modeling perturbers with flexion shifts larger than $\Delta_3 x > 10^{-4}{}''$ allows one to constrain the bias on H_0 due to this uncertainty to the percent level. Out of our 10 groups in DES J0408−5354 we find one group (labelled 5 in Table 3) that has a flexion shift of $\log_{10} \Delta_3 x = -3.86^{+0.97}_{-0.72}$. This group has 17 members, one of which is the lensing galaxy G1 and the centroid of this group is close to the lens. However Shajib et al. (2019a) show that the change in H_0 of including this group would result in a decrease of approximately 0.4 percent so it is not explicitly included in the mass model. For WGD 2038−4008 , we find two galaxy groups from our spectroscopic redshift sample, but neither group has flexion shift above our cut.

To calculate the flexion shift for individual galaxies we start with the general methodology described in Sluse et al. (2019) and then use two different scaling relations (Zahid et al. 2016; Auger et al. 2010) to estimate the line-of-sight central velocity dispersion of the galaxy from its stellar mass. The stellar masses are calculated using galaxy model fitting to DES photometry, as detailed in §3.3. The Auger et al. (2010) relation between velocity dispersion and stellar mass gives more conservative, larger flexion shift values, resulting in four galaxies in DES J0408−5354 with flexion shifts larger

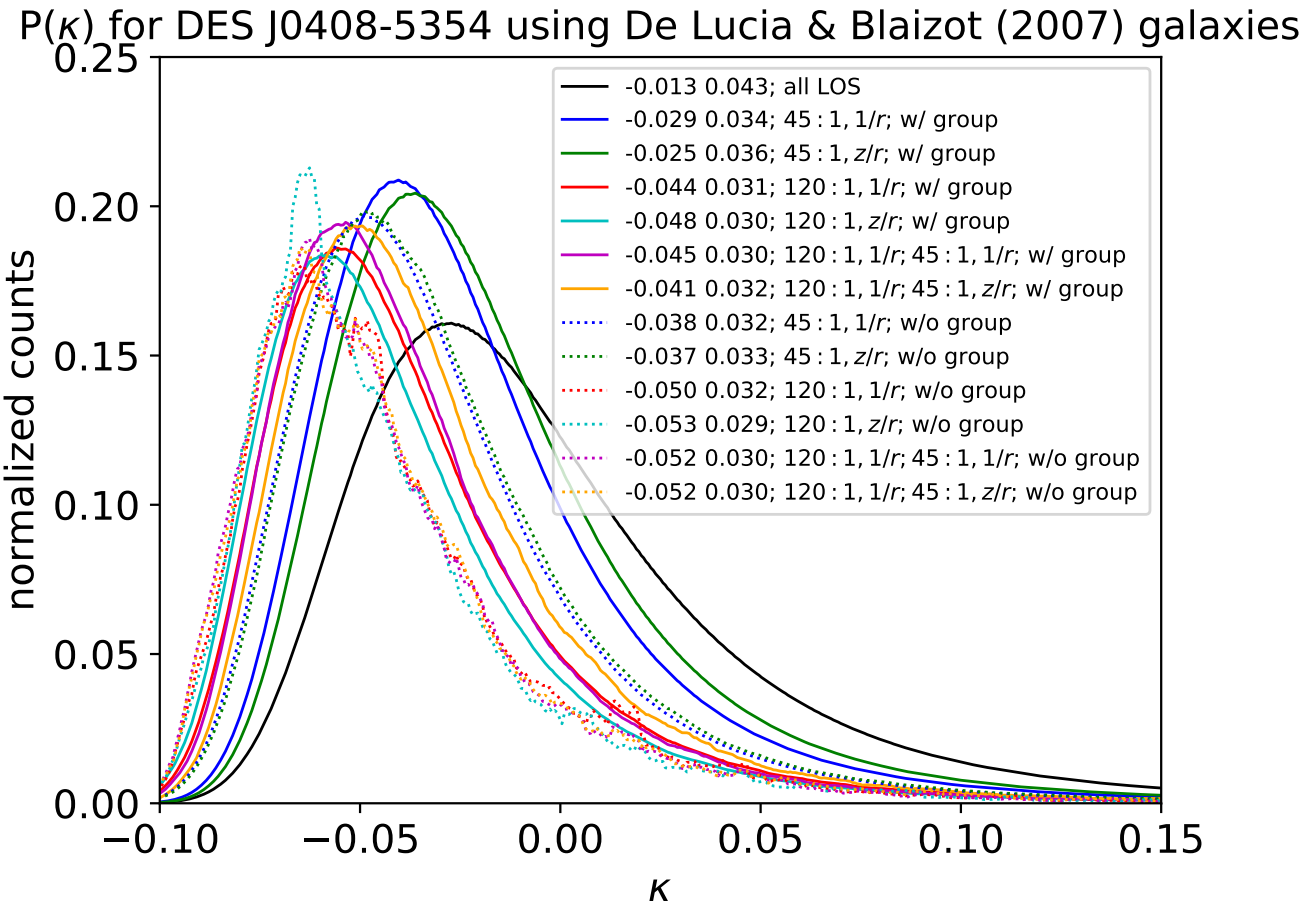

Figure 17. Histograms of smoothed $\kappa_{\rm ext}$ distributions for DES J0408−5354 for a variety of constraints, using the De Lucia & Blaizot (2007) semi-analytical galaxy models. "w/ group" and "w/o group" refer to the case when the member galaxies of the lens group are kept or not kept as part of the LOS, respectively. The first distribution shown is for the case when all LOS from MS are used, without constraints. The first two numbers in the legend are the median and the semi-difference between the 16th and the 84th percentiles of each distribution, respectively.

than our $\log_{10}\Delta_3 x = -4.0$ cut; these galaxies (G3, G4, G5, and G6 in Table 4) are therefore selected for explicit modeling by Shajib et al. (2019a). For WGD 2038−4008 , we do not find any individual galaxies with flexion shift greater than our cut.

Our measurement of the external convergence $\kappa_{\rm ext}$ starts with determining the line-of-sight under/overdensities for DES J0408−5354 and WGD 2038−4008 using weighted number counts. We use a catalog of galaxy properties for the two fields from the DES Year 3 Gold version 2.2 catalog. As both of these fields are within the DES footprint we are able to select the control fields from the DES catalog as well. This helps us to avoid potential biases due to mismatches in, for example, image resolution between the target and control fields. Where available we use the spectroscopic redshifts for the galaxies in the target fields. As detailed in §7, for the galaxy counts we use four different sets of weights (including weighting by redshift and/or radius), two different apertures (one of radius 120″ and the other of radius 45″), as well as two photometric redshift schemes (DNF and BPZ). For DES J0408−5354 we remove the four galaxies (G3-G6 in Table 4) which are explicitly incorporated into the lens model. Also for DES J0408−5354 we calculate the weighted counts for both the case where the galaxy group containing the main deflector G1 is included in the count and the case where we explicitly exclude the group. We find that DES J0408−5354 lives in a significantly under-dense environment whereas WGD 2038−4008 is in an environment that is closer to mean density. As described in §8, we then apply the same observational constraints to the MS, with galaxies from the De Lucia & Blaizot (2007) semi-analytical model, to compute ζ_q, the ratio of weighted galaxy counts of target to control fields. We obtain $P(\kappa_{\rm ext})$, the probability distribution of the external convergence $\kappa_{\rm ext}$, by selecting lines of sight from the MS that match the observed ζ_q constraints. As expected from the significantly underdense field of DES J0408−5354 , the resulting fiducial $P(\kappa_{\rm ext})$ distributions are tight (with width ≈ 0.03 in $\kappa_{\rm ext}$) and medians around $\kappa_{\rm ext} \sim -0.04$ - -0.05. For the case excluding the group containing G1 from the number counts, the median $\kappa_{\rm ext}$ decreases by $\lesssim 0.01$. The distributions for WGD 2038−4008 are much tighter, with width

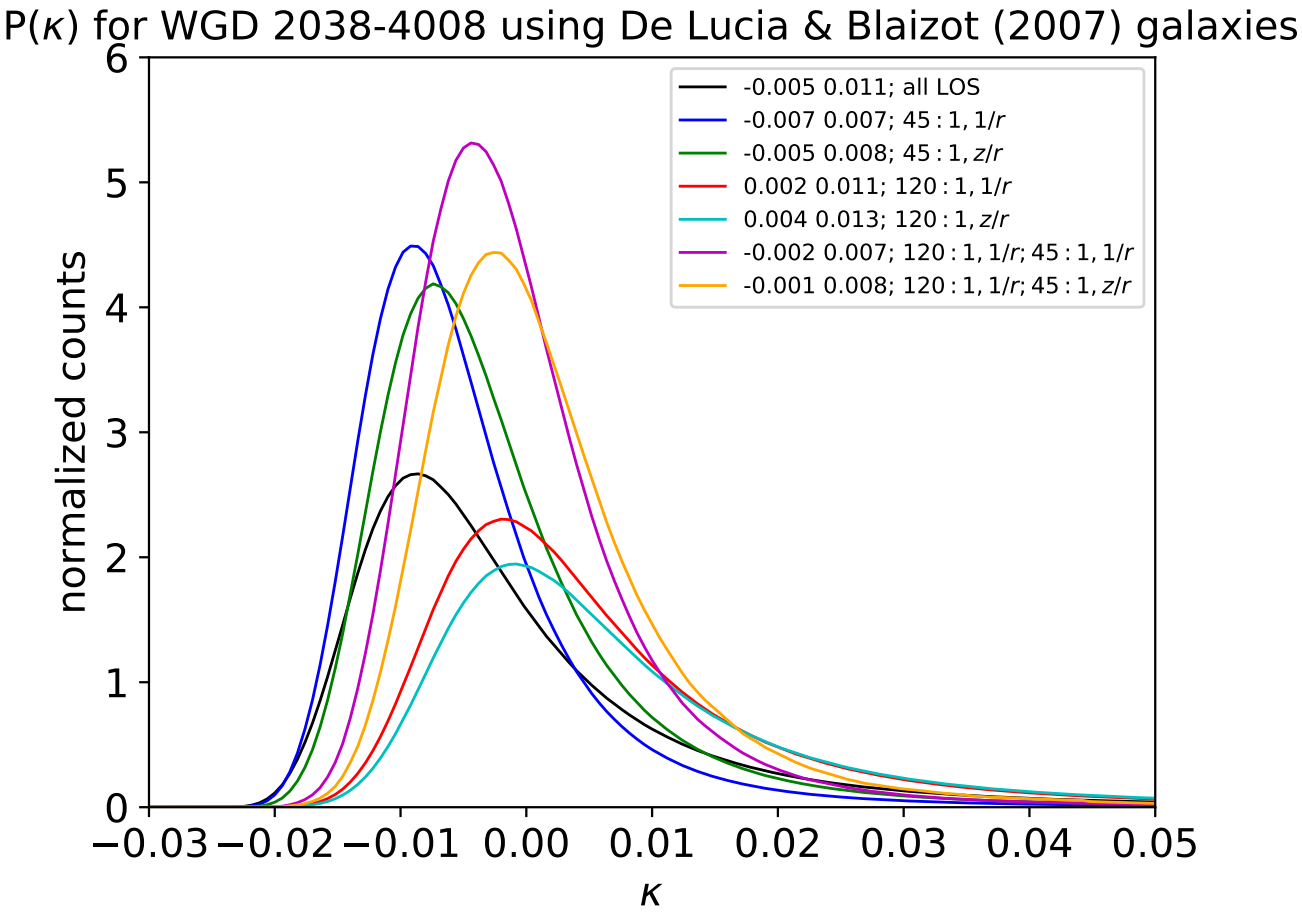

Figure 18. Similar to Figure 17, for the case of WGD 2038−4008 .

~ 1%. This is expected due to the significantly lower source redshift ($z_s = 0.777$ for WGD 2038−4008 vs. $z_s = 2.375$ for DES J0408−5354), as there will be fewer structures along the line of sight to contribute to the convergence.

ACKNOWLEDGMENTS

J.P. would like to thank Gourav Khullar for their help and insightful discussions that helped improve the analysis in this paper. This work made use of computing resources and support provided by the Research Computing Center at the University of Chicago. J.P. is supported in part by the Kavli Institute for Cosmological Physics at the University of Chicago through grant NSF PHY-1125897 and an endowment from the Kavli Foundation and its founder Fred Kavli.

AJS was supported by the National Aeronautics and Space Administration (NASA) through the Space Telescope Science Institute (STScI) grant HST-GO-15320. AJS was also supported by the Dissertation Year Fellowship from the University of California, Los Angeles (UCLA) graduate division.

TA acknowledges support from Proyecto FONDECYT N: 1190335.

This work was supported by World Premier International Research Center Initiative (WPI Initiative), MEXT, Japan.

CDF acknowledges support for this work from the National Science Foundation under Grant No. AST-1715611.

SM acknowledges the funding from the European Research Council (ERC) under the EUs Horizon 2020 research and innovation program (COSMICLENS; grant agreement No. 787886).

Funding for the DES Projects has been provided by the U.S. Department of Energy, the U.S. National Science Foundation, the Ministry of Science and Education of Spain, the Science and Technology Facilities Council of the United Kingdom, the Higher Education Funding Council for England, the National Center for Supercomputing Applications at the University of Illinois at Urbana-Champaign, the Kavli Institute of Cosmological Physics at the University of Chicago, the Center for Cosmology and Astro-Particle Physics at the Ohio State University, the Mitchell Institute for Fundamental Physics and Astronomy at Texas A&M University, Financiadora de Estudos e Projetos, Fundação Carlos Chagas Filho de Amparo à Pesquisa do Estado do Rio de Janeiro, Conselho Nacional de Desenvolvimento Científico e Tecnológico and the Ministério da Ciência, Tecnologia

Table 6. Statistics of $P(\kappa_{\rm ext}|\zeta_1^{45''}, \zeta_{1/r}^{45''}, \zeta_1^{120''}, \zeta_{1/r}^{120''}, \gamma)$ as a function of γ, for the DES J0408−5354 and WGD 2038−4008 systems. We report the variation in the median and semi-difference of the 16th and 84th quantiles. The error bar around each γ constraint is 0.005. For WGD 2038−4008 the distributions for large γ are too noisy to report.

	DES J0408−5354		WGD 2038−4008	
γ	med_κ	σ_κ	med_κ	σ_κ
0.01	−0.053	0.025	−0.004	0.006
0.02	−0.052	0.025	−0.002	0.007
0.03	−0.049	0.026	0.002	0.008
0.04	−0.046	0.027	0.008	0.011
0.05	−0.041	0.029	0.016	0.017
0.06	−0.035	0.032	0.032	0.028
0.07	−0.028	0.035	0.056	0.038
0.08	−0.020	0.039	0.074	0.042
0.09	−0.009	0.043	0.101	0.046
0.10	0.002	0.048	0.128	0.054
0.11	0.018	0.054	...	...
0.12	0.032	0.060	...	...
0.13	0.046	0.067	...	...
0.14	0.067	0.075	...	...
0.15	0.088	0.083	...	...

e Inovação, the Deutsche Forschungsgemeinschaft and the Collaborating Institutions in the Dark Energy Survey.

The Collaborating Institutions are Argonne National Laboratory, the University of California at Santa Cruz, the University of Cambridge, Centro de Investigaciones Energéticas, Medioambientales y Tecnológicas-Madrid, the University of Chicago, University College London, the DES-Brazil Consortium, the University of Edinburgh, the Eidgenössische Technische Hochschule (ETH) Zürich, Fermi National Accelerator Laboratory, the University of Illinois at Urbana-Champaign, the Institut de Ciències de l'Espai (IEEC/CSIC), the Institut de Física d'Altes Energies, Lawrence Berkeley National Laboratory, the Ludwig-Maximilians Universität München and the associated Excellence Cluster Universe, the University of Michigan, the National Optical Astronomy Observatory, the University of Nottingham, The Ohio State University, the University of Pennsylvania, the University of Portsmouth, SLAC National Accelerator Laboratory, Stanford University, the University of Sussex, Texas A&M University, and the OzDES Membership Consortium.

Based in part on observations at Cerro Tololo Inter-American Observatory, National Optical Astronomy Observatory, which is operated by the Association of Universities for Research in Astronomy (AURA) under a cooperative agreement with the National Science Foundation.

The DES data management system is supported by the National Science Foundation under Grant Numbers AST-1138766 and AST-1536171. The DES participants from Spanish institutions are partially supported by MINECO under grants AYA2015-71825, ESP2015-88861, FPA2015-68048, SEV-2012-0234, SEV-2016-0597, and MDM-2015-0509, some of which include ERDF funds from the European Union. IFAE is partially funded by the CERCA program of the Generalitat de Catalunya. Research leading to these results has received funding from the European Research Council under the European Union's Seventh Framework Program (FP7/2007-2013) including ERC grant agreements 240672, 291329, and 306478. We acknowledge support from the Australian Research Council Centre of Excellence for All-sky Astrophysics (CAASTRO), through project number CE110001020.

This manuscript has been authored by Fermi Research Alliance, LLC under Contract No. DE-AC02-07CH11359 with the U.S. Department of Energy, Office of Science, Office of High Energy Physics. The United States Government retains and the publisher, by accepting the article for publication, acknowledges that the United States Government retains a non-exclusive, paid-up, irrevocable, world-wide license to publish or reproduce the published form of this manuscript, or allow others to do so, for United States Government purposes.

Based on observations obtained at the Gemini Observatory (acquired through the Gemini Observatory Archive and processed using the Gemini IRAF package), which is operated by the Association of Universities for Research in Astronomy, Inc., under a cooperative agreement with the NSF on behalf of the Gemini partnership: the National Science Foundation (United States), National Research Council (Canada), CONICYT (Chile), Ministerio de Ciencia, Tecnología e Innovación Productiva (Argentina), Ministério da Ciência, Tecnologia e Inovação (Brazil), and Korea Astronomy and Space Science Institute (Republic of Korea).

This paper includes data gathered with the 6.5 meter Magellan Telescopes located at Las Campanas Observatory, Chile.

Based on observations collected at the European Southern Observatory under ESO programme 0102.A-0600(E).

This work made extensive use of the Astropy library, a community-developed core Python package for Astronomy (Astropy Collaboration et al. 2013).

REFERENCES

Abbott T. M. C., et al., 2018, ApJS, 239, 18
Agnello A., et al., 2018, MNRAS, 479, 4345
Ammons S. M., Wong K. C., Zabludoff A. I., Keeton C. R., 2014, ApJ, 781, 2
Amorisco N. C., Evans N. W., 2012, MNRAS, 424, 1899
Andreon S., Hurn M. A., 2010, MNRAS, 404, 1922
Arnouts S., Cristiani S., Moscardini L., Matarrese S., Lucchin F., Fontana A., Giallongo E., 1999, MNRAS, 310, 540
Astropy Collaboration et al., 2013, A&A, 558, A33
Auger M. W., Treu T., Brewer B. J., Marshall P. J., 2010, Monthly Notices of the Royal Astronomical Society: Letters, Volume 411, Issue 1, pp. L6-L10., 411, L6
Beers T. C., Flynn K., Gebhardt K., 1990, The Astronomical Journal, 100, 32
Benítez N., 2000, ApJ, 536, 571
Bertin E., Arnouts S., 1996, Astronomy and Astrophysics Supplement Series, 117, 393
Birrer S., et al., 2019, MNRAS, 484, 4726
Bruzual G., Charlot S., 2003, MNRAS, 344, 1000
Chabrier G., 2003, PASP, 115, 763

Chen G. C. F., et al., 2019, MNRAS, 490, 1743
Collett T. E., et al., 2013, MNRAS, 432, 679
De Lucia G., Blaizot J., 2007, MNRAS, 375, 2
De Vicente J., Sánchez E., Sevilla-Noarbe I., 2016, MNRAS, 459, 3078
Desai S., et al., 2012, The Astrophysical Journal, Volume 757, Issue 1, article id. 83, 22 pp. (2012)., 757
Diehl H. T., et al., 2019,] 10.2172/1596042
Dressler A., et al., 2011, PASP, 123, 288
Drlica-Wagner A., et al., 2018, ApJS, 235, 33
Fassnacht C. D., Koopmans L. V. E., Wong K. C., 2011, MNRAS, 410, 2167
Flaugher B., et al., 2015, The Astronomical Journal, Volume 150, Issue 5, article id. 150, 43 pp. (2015)., 150
Foreman-Mackey D., Hogg D. W., Lang D., Goodman J., 2013, PASP, 125, 306
Goodman J., Weare J., 2010, Communications in Applied Mathematics and Computational Science, Vol.˜5, No.˜1, p.˜65-80, 2010, 5, 65
Greene Z. S., et al., 2013, ApJ, 768, 39
Guérou A., et al., 2017, A&A, 608, A5
Hamilton A. J. S., Tegmark M., 2004, MNRAS, 349, 115
Henriques B. M. B., White S. D. M., Thomas P. A., Angulo R., Guo Q., Lemson G., Springel V., Overzier R., 2015, MNRAS, 451, 2663
Heymans C., et al., 2012, MNRAS, 427, 146
Hilbert S., Hartlap J., White S. D. M., Schneider P., 2009, A&A, 499, 31
Hoyle B., et al., 2018, MNRAS, 478, 592
Ilbert O., et al., 2006, A&A, 457, 841
Koleva M., Prugniel P., Bouchard A., Wu Y., 2009, A&A, 501, 1269
Koposov S. E., et al., 2011, ApJ, 736, 146
Kurtz M. J., Mink D. J., 1998, Publications of the Astronomical Society of the Pacific, 110, 934
Laporte C. F. P., Agnello A., Navarro J. F., 2019, MNRAS, 484, 245
Lemson G., Virgo Consortium t., 2006, arXiv e-prints, pp astro–ph/0608019
Lin H., et al., 2017, ApJ, 838, L15
Martin N. F., Collins M. L. M., Longeard N., Tollerud E., 2018, ApJ, 859, L5
McCully C., Keeton C. R., Wong K. C., Zabludoff A. I., 2014, MNRAS, 443, 3631
McCully C., Keeton C. R., Wong K. C., Zabludoff A. I., 2017, ApJ, 836, 141
Morganson E., et al., 2018, Publications of the Astronomical Society of the Pacific, 130, 074501
Mosteller F., Tukey J. W., 1977, Data analysis and regression. A second course in statistics. `http://adsabs.harvard.edu/abs/1977dars.book.....M`
Oemler A., Clardy K., Kelson D., Walth G., Villanueva E., 2017, COSMOS: Carnegie Observatories System for MultiObject Spectroscopy (ascl:1705.001)
Peng C. Y., Ho L. C., Impey C. D., Rix H.-W., 2010, AJ, 139, 2097
Planck Collaboration et al., 2016, A&A, 596, A105
Refsdal S., 1964, Monthly Notices of the Royal Astronomical Society, 128, 307
Rusu C. E., et al., 2017, MNRAS, 467, 4220
Rusu C. E., et al., 2019, arXiv e-prints,
Rykoff E. S., et al., 2014, The Astrophysical Journal, 785, 104
Salpeter E. E., 1955, ApJ, 121, 161
Sánchez-Blázquez P., et al., 2006, MNRAS, 371, 703
Shajib et al. 2019a, MNRAS, submitted
Shajib A. J., et al., 2019b, Monthly Notices of the Royal Astronomical Society, 483, 5649
Sluse D., et al., 2017, Monthly Notices of the Royal Astronomical Society, 470, 4838
Sluse D., et al., 2019, MNRAS, 490, 613
Springel V., et al., 2005, Nature, 435, 629
Suyu S. H., Marshall P. J., Auger M. W., Hilbert S., Blandford R. D., Koopmans L. V. E., 2010a,] 10.1088/0004-637X/711/1/201, 1, 201
Suyu S. H., Marshall P. J., Auger M. W., Hilbert S., Blandford R. D., Koopmans L. V. E., Fassnacht C. D., Treu T., 2010b, The Astrophysical Journal, Volume 711, Issue 1, pp. 201-221 (2010)., 711, 201
Suyu S. H., Auger M. W., Hilbert S., Marshall P. J., Tewes M., Treu T., Fassnacht C. D., 2013,] 10.1088/0004-637X/766/2/70, 70
Suyu S. H., et al., 2017, MNRAS, 468, 2590
Swanson M. E. C., Tegmark M., Hamilton A. J. S., Hill J. C., 2008, MNRAS, 387, 1391
Treu T., Koopmans L. V. E., 2002, MNRAS, 337, L6
Treu T., Marshall P. J., 2016, A&ARv, 24, 11
Treu T., et al., 2018, MNRAS, 481, 1041
Vazdekis A., Sánchez-Blázquez P., Falcón-Barroso J., Cenarro A. J., Beasley M. A., Cardiel N., Gorgas J., Peletier R. F., 2010, MNRAS, 404, 1639
Wainer H., Thissen D., 1976, Psychometrika, 41, 9
Walker M. G., Peñarrubia J., 2011, ApJ, 742, 20
Wilman D. J., Balogh M. L., Bower R. G., Mulchaey J. S., Oemler A., Carlberg R. G., Morris S. L., Whitaker R. J., 2005, MNRAS, 358, 71
Wilson M. L., Zabludoff A. I., Ammons S. M., Momcheva I. G., Williams K. A., Keeton C. R., 2016, ApJ, 833, 194
Wong K. C., et al., 2019, arXiv e-prints, p. arXiv:1907.04869
Zahid H. J., Geller M. J., Fabricant D. G., Hwang H. S., 2016, ApJ, 832, 203

AFFILIATIONS

[1]Fermi National Accelerator Laboratory, P. O. Box 500, Batavia, IL 60510, USA
[2]National Astronomical Observatory of Japan, 2-21-1 Osawa, Mitaka, Tokyo 181-8588, Japan
[3]Department of Astronomy & Astrophysics, University of Chicago, Chicago, IL 60637
[4]Kavli Institute for Cosmological Physics, University of Chicago, Chicago, IL 60637
[5]DARK, Niels Bohr Institute, University of Copenhagen, Lyngbyvej 2, DK-2100 Copenhagen, Denmark
[6]Department of Physics and Astronomy, PAB, 430 Portola Plaza, Box 951547, Los Angeles, CA 90095-1547, USA
[7]Institute of Cosmology & Gravitation, University of Portsmouth, Portsmouth, PO1 3FX, UK
[8]Kavli Institute for Particle Astrophysics and Cosmology, Stanford University, 452 Lomita Mall, Stanford, CA 94305, USA
[9]Departamento de Ciencias Fisicas, Universidad Andres Bello Fernandez Concha 700, Las Condes, Santiago, Chile
[10]Millennium Institute of Astrophysics, Chile
[11]Department of Physics, University of California Davis, 1 Shields Avenue, Davis, CA 95616, USA
[12]Laboratoire d'Astrophysique, Ecole Polytechnique Fédérale de Lausanne (EPFL), Observatoire de Sauverny, CH-1290 Versoix, Switzerland
[13]STAR Institute, Quartier Agora - Allée du six Aout, 19c B-4000 Liège, Belgium [14]Kavli IPMU (WPI), UTIAS, The University of Tokyo, Kashiwa, Chiba 277-8583, Japan

[15] Departamento de Física Matemática, Instituto de Física, Universidade de São Paulo, CP 66318, São Paulo, SP, 05314-970, Brazil
[16] Laboratório Interinstitucional de e-Astronomia - LIneA, Rua Gal. José Cristino 77, Rio de Janeiro, RJ - 20921-400, Brazil
[17] Instituto de Fisica Teorica UAM/CSIC, Universidad Autonoma de Madrid, 28049 Madrid, Spain
[18] CNRS, UMR 7095, Institut d'Astrophysique de Paris, F-75014, Paris, France
[19] Sorbonne Universités, UPMC Univ Paris 06, UMR 7095, Institut d'Astrophysique de Paris, F-75014, Paris, France
[20] Department of Physics and Astronomy, Pevensey Building, University of Sussex, Brighton, BN1 9QH, UK
[21] Department of Physics & Astronomy, University College London, Gower Street, London, WC1E 6BT, UK
[22] Centro de Investigaciones Energéticas, Medioambientales y Tecnológicas (CIEMAT), Madrid, Spain
[23] Department of Astronomy, University of Illinois at Urbana-Champaign, 1002 W. Green Street, Urbana, IL 61801, USA
[24] National Center for Supercomputing Applications, 1205 West Clark St., Urbana, IL 61801, USA
[25] Institut de Física d'Altes Energies (IFAE), The Barcelona Institute of Science and Technology, Campus UAB, 08193 Bellaterra (Barcelona) Spain
[26] Institut d'Estudis Espacials de Catalunya (IEEC), 08034 Barcelona, Spain
[27] Institute of Space Sciences (ICE, CSIC), Campus UAB, Carrer de Can Magrans, s/n, 08193 Barcelona, Spain
[28] INAF-Osservatorio Astronomico di Trieste, via G. B. Tiepolo 11, I-34143 Trieste, Italy
[29] Institute for Fundamental Physics of the Universe, Via Beirut 2, 34014 Trieste, Italy
[30] Observatório Nacional, Rua Gal. José Cristino 77, Rio de Janeiro, RJ - 20921-400, Brazil
[31] Department of Physics, IIT Hyderabad, Kandi, Telangana 502285, India
[32] Department of Astronomy/Steward Observatory, University of Arizona, 933 North Cherry Avenue, Tucson, AZ 85721-0065, USA
[33] Jet Propulsion Laboratory, California Institute of Technology, 4800 Oak Grove Dr., Pasadena, CA 91109, USA
[34] Santa Cruz Institute for Particle Physics, Santa Cruz, CA 95064, USA
[35] Department of Physics, Stanford University, 382 Via Pueblo Mall, Stanford, CA 94305, USA
[36] Kavli Institute for Particle Astrophysics & Cosmology, P. O. Box 2450, Stanford University, Stanford, CA 94305, USA
[37] SLAC National Accelerator Laboratory, Menlo Park, CA 94025, USA
[38] School of Mathematics and Physics, University of Queensland, Brisbane, QLD 4072, Australia
[39] Center for Cosmology and Astro-Particle Physics, The Ohio State University, Columbus, OH 43210, USA
[40] Department of Physics, The Ohio State University, Columbus, OH 43210, USA
[41] Center for Astrophysics | Harvard & Smithsonian, 60 Garden Street, Cambridge, MA 02138, USA
[42] Australian Astronomical Optics, Macquarie University, North Ryde, NSW 2113, Australia
[43] Lowell Observatory, 1400 Mars Hill Rd, Flagstaff, AZ 86001, USA
[44] George P. and Cynthia Woods Mitchell Institute for Fundamental Physics and Astronomy, and Department of Physics and Astronomy, Texas A&M University, College Station, TX 77843, USA
[45] Department of Astrophysical Sciences, Princeton University, Peyton Hall, Princeton, NJ 08544, USA
[46] Institució Catalana de Recerca i Estudis Avançats, E-08010 Barcelona, Spain
[47] Department of Physics, University of Michigan, Ann Arbor, MI 48109, USA
[48] School of Physics and Astronomy, University of Southampton, Southampton, SO17 1BJ, UK
[49] Brandeis University, Physics Department, 415 South Street, Waltham MA 02453
[50] Computer Science and Mathematics Division, Oak Ridge National Laboratory, Oak Ridge, TN 37831
[51] Max Planck Institute for Extraterrestrial Physics, Giessenbachstrasse, 85748 Garching, Germany
[52] Universitäts-Sternwarte, Fakultät für Physik, Ludwig-Maximilians Universität München, Scheinerstr. 1, 81679 München, Germany

APPENDIX A: PROPERTIES FOR ALL GALAXIES AND GALAXY GROUPS

We present the full sample of galaxies in the spectroscopic sample as well as the group membership of each identified group.

Table A1: Properties of all 199 galaxies in spectroscopic survey of the field of DES J0408−5354 and 54 galaxies in the spectroscopic survey of the field of WGD 2038−4008, arranged in order of decreasing flexion shift on the lens galaxy. The columns display, in order, the galaxy ID, coordinates (RA, DEC in degrees; ICRS), redshift z, DES `MOF_CM_MAG_CORRECTED` i-band magnitudes (whenever possible), distances to the lensing galaxy and flexion shifts. Spectroscopic redshift uncertainties are about 100 km s^{-1}, or 0.00033 in redshift. Galaxies with bad `MOF` magnitudes are indicated with †; for these galaxies, we use `MAG_AUTO_CORRECTED` photometry and the corresponding stellar mass estimates from that photometric data. For the galaxy IDs, DES Y3 galaxies have 9-digit IDs, DES Y1 galaxies have 10-digit IDs, and MUSE galaxies were labeled with the prefix "MUSE" and sorted by ascending redshifts. Stellar masses and corresponding uncertainties were calculated using the `Le PHARE` galaxy template fitting code and DES Y3 photometry (see §3.3). Flexion shift and uncertainties are calculated following the method described in §6.1-6.1.1.

ID	RA (deg)	DEC (deg)	z	i-band Mag	$\log_{10}(M_*)$ ($log_{10}(M_\odot)$)	$\Delta\theta$ (arcsec)	$\log_{10}(\Delta_3 x_{\rm Zahid})$ ($\log_{10}$(arcsec))	$\log_{10}(\Delta_3 x_{\rm Auger})$ ($\log_{10}$(arcsec))
				DES J0408−5354				
488068102	62.090965	-53.901634	0.76866	20.096	$11.42^{+0.10}_{-0.12}$	6.4	$-2.21^{+0.25}_{-0.29}$	$-2.20^{+0.21}_{-0.22}$
488065185	62.095575	-53.898291	0.59441	21.867	$10.29^{+0.10}_{-0.17}$	12.4	$-3.95^{+0.42}_{-0.58}$	$-3.42^{+0.21}_{-0.24}$
488066144	62.090243	-53.903609	0.77069	22.015	$10.66^{+0.13}_{-0.17}$	13.4	$-4.07^{+0.38}_{-0.51}$	$-3.72^{+0.22}_{-0.24}$
488066768	62.092923	-53.900091	1.03197	23.682	$9.68^{+0.24}_{-0.25}$	5.4	$-4.93^{+0.63}_{-0.93}$	$-3.87^{+0.26}_{-0.27}$
488066462	62.083912	-53.903969	0.60048	22.304	$9.88^{+0.12}_{-0.19}$	20.2	$-5.24^{+0.52}_{-0.79}$	$-4.37^{+0.22}_{-0.25}$
MUSE6/488065214†	62.077898	-53.903878	0.59797	22.303	$10.37^{+0.11}_{-0.16}$	30.2	$-5.02^{+0.41}_{-0.56}$	$-4.53^{+0.21}_{-0.23}$
488070148	62.084648	-53.885204	0.27247	18.309	$10.99^{+0.04}_{-0.04}$	54.3	$-4.81^{+0.31}_{-0.37}$	$-4.61^{+0.20}_{-0.20}$
488066886	62.090541	-53.904725	0.77568	22.925	$9.91^{+0.16}_{-0.30}$	17.4	$-5.46^{+0.53}_{-0.90}$	$-4.61^{+0.23}_{-0.30}$
488070807	62.072770	-53.910296	0.59811	19.975	$11.27^{+0.05}_{-0.06}$	53.0	$-4.69^{+0.25}_{-0.30}$	$-4.61^{+0.20}_{-0.21}$
MUSE8/488067782	62.103108	-53.897861	0.59832	22.100	$10.11^{+0.13}_{-0.20}$	27.9	$-5.29^{+0.48}_{-0.71}$	$-4.62^{+0.22}_{-0.25}$
488071104	62.077670	-53.913521	0.29469	18.555	$11.05^{+0.04}_{-0.04}$	56.0	$-4.80^{+0.30}_{-0.36}$	$-4.62^{+0.20}_{-0.20}$
488070774	62.075134	-53.912907	0.29368	18.519	$11.01^{+0.04}_{-0.04}$	57.0	$-4.87^{+0.30}_{-0.37}$	$-4.67^{+0.20}_{-0.20}$
MUSE15/488066060†	62.080992	-53.904565	0.76785	22.762	$10.44^{+0.12}_{-0.18}$	26.1	$-5.19^{+0.40}_{-0.55}$	$-4.74^{+0.22}_{-0.24}$
488066584	62.071692	-53.906245	0.59727	21.426	$10.69^{+0.04}_{-0.03}$	45.8	$-5.18^{+0.35}_{-0.45}$	$-4.84^{+0.20}_{-0.20}$
MUSE12/488067196	62.093482	-53.905711	0.64363	23.311	$9.18^{+0.22}_{-0.28}$	21.9	$-6.60^{+0.65}_{-1.05}$	$-5.10^{+0.25}_{-0.29}$
MUSE10/488070958	62.085862	-53.910180	0.60029	22.304	$10.01^{+0.14}_{-0.22}$	38.3	$-5.86^{+0.50}_{-0.77}$	$-5.10^{+0.22}_{-0.26}$
489523481	62.078380	-53.881917	0.59451	19.918	$11.04^{+0.07}_{-0.18}$	69.6	$-5.31^{+0.30}_{-0.43}$	$-5.13^{+0.21}_{-0.24}$
MUSE9/488069251†	62.085632	-53.891330	0.59906	23.333	$9.49^{+0.26}_{-0.35}$	32.4	$-6.48^{+0.67}_{-1.12}$	$-5.26^{+0.27}_{-0.33}$
488070002	62.070997	-53.882405	0.37961	20.614	$10.39^{+0.05}_{-0.06}$	75.2	$-6.02^{+0.39}_{-0.51}$	$-5.54^{+0.20}_{-0.20}$
488070966	62.067875	-53.910488	0.59977	21.729	$10.11^{+0.15}_{-0.19}$	61.2	$-6.32^{+0.49}_{-0.70}$	$-5.65^{+0.23}_{-0.25}$
488067363	62.134647	-53.901754	0.59479	21.047	$10.86^{+0.05}_{-0.05}$	94.1	$-5.92^{+0.33}_{-0.41}$	$-5.66^{+0.20}_{-0.20}$
MUSE14/488070770	62.099785	-53.908977	0.76669	23.533	$9.85^{+0.21}_{-0.28}$	38.3	$-6.56^{+0.58}_{-0.89}$	$-5.66^{+0.24}_{-0.29}$
488070443	62.101056	-53.907011	1.17764	21.911	$11.01^{+0.34}_{-0.32}$	34.2	$-5.88^{+0.48}_{-0.55}$	$-5.68^{+0.31}_{-0.31}$
488071406	62.054830	-53.913785	0.44241	20.276	$10.58^{+0.06}_{-0.07}$	90.5	$-6.08^{+0.37}_{-0.48}$	$-5.69^{+0.20}_{-0.21}$
405340030	62.118966	-53.880474	0.57772	20.663	$10.71^{+0.07}_{-0.18}$	92.5	$-6.06^{+0.36}_{-0.50}$	$-5.73^{+0.21}_{-0.24}$
488071428	62.068708	-53.913477	0.59843	21.581	$10.15^{+0.12}_{-0.17}$	67.2	$-6.36^{+0.46}_{-0.66}$	$-5.73^{+0.22}_{-0.24}$

488072005	62.068079	-53.917283	0.54122	21.624	$10.32^{+0.10}_{-0.18}$	78.5	$-6.27^{+0.41}_{-0.58}$	$-5.76^{+0.21}_{-0.24}$
MUSE19/488068048	62.088268	-53.890642	0.91504	23.065	$9.92^{+0.30}_{-0.29}$	33.6	$-6.64^{+0.64}_{-0.87}$	$-5.80^{+0.29}_{-0.29}$
488067814	62.109798	-53.896296	0.78734	22.001	$9.90^{+0.20}_{-0.24}$	43.1	$-6.68^{+0.56}_{-0.83}$	$-5.83^{+0.24}_{-0.27}$
MUSE22/488065663	62.090044	-53.891845	1.09148	23.419	$10.22^{+0.28}_{-0.27}$	29.0	$-6.40^{+0.59}_{-0.75}$	$-5.83^{+0.28}_{-0.29}$
488072697	62.061177	-53.921532	0.27257	19.767	$10.33^{+0.04}_{-0.05}$	99.6	$-6.37^{+0.40}_{-0.52}$	$-5.87^{+0.20}_{-0.20}$
MUSE20/488065095	62.091419	-53.890585	0.94698	23.108	$9.91^{+0.34}_{-0.26}$	33.6	$-6.74^{+0.69}_{-0.85}$	$-5.89^{+0.31}_{-0.28}$
488070825	62.106067	-53.909453	0.77562	21.908	$9.93^{+0.21}_{-0.26}$	47.8	$-6.74^{+0.56}_{-0.84}$	$-5.91^{+0.24}_{-0.28}$
488066235	62.023367	-53.910705	0.57025	19.314	$11.28^{+0.06}_{-0.17}$	147.4	$-6.00^{+0.26}_{-0.36}$	$-5.92^{+0.20}_{-0.24}$
489523492	62.067524	-53.881235	0.78001	20.704	$10.92^{+0.12}_{-0.18}$	82.9	$-6.17^{+0.34}_{-0.46}$	$-5.93^{+0.22}_{-0.24}$
489521356	62.083229	-53.863995	0.57765	20.123	$11.02^{+0.07}_{-0.17}$	130.1	$-6.14^{+0.31}_{-0.42}$	$-5.95^{+0.21}_{-0.24}$
488070625	62.057786	-53.908625	0.93778	21.744	$11.27^{+0.05}_{-0.07}$	76.0	$-6.04^{+0.26}_{-0.31}$	$-5.96^{+0.20}_{-0.21}$
488073290	62.106161	-53.923866	0.57035	20.933	$10.36^{+0.07}_{-0.12}$	92.5	$-6.47^{+0.40}_{-0.54}$	$-5.98^{+0.21}_{-0.22}$
488074578	62.144676	-53.934498	0.27176	18.315	$11.11^{+0.05}_{-0.12}$	169.6	$-6.16^{+0.29}_{-0.37}$	$-6.01^{+0.20}_{-0.22}$
488070449	62.025309	-53.910519	0.42954	19.664	$10.95^{+0.05}_{-0.07}$	143.3	$-6.24^{+0.32}_{-0.39}$	$-6.01^{+0.20}_{-0.21}$
488073735	62.139479	-53.928501	0.42858	19.429	$10.95^{+0.05}_{-0.07}$	146.4	$-6.27^{+0.32}_{-0.39}$	$-6.04^{+0.20}_{-0.21}$
488072433	62.093088	-53.919040	0.30909	21.573	$9.45^{+0.09}_{-0.11}$	69.2	$-7.31^{+0.58}_{-0.88}$	$-6.06^{+0.21}_{-0.22}$
489522058	62.078867	-53.872863	0.09083	18.298	$9.90^{+0.04}_{-0.04}$	100.3	$-6.92^{+0.49}_{-0.68}$	$-6.07^{+0.20}_{-0.20}$
488066362	62.052505	-53.883271	0.94641	21.835	$11.50^{+0.03}_{-0.03}$	100.2	$-6.14^{+0.21}_{-0.24}$	$-6.17^{+0.20}_{-0.20}$
488072414	62.148320	-53.919275	0.42744	20.060	$10.70^{+0.10}_{-0.07}$	141.2	$-6.50^{+0.37}_{-0.45}$	$-6.17^{+0.21}_{-0.21}$
488072532	62.024006	-53.921066	0.44478	19.809	$10.87^{+0.06}_{-0.08}$	160.1	$-6.49^{+0.33}_{-0.42}$	$-6.23^{+0.20}_{-0.21}$
488067185	62.020675	-53.907526	0.30566	19.692	$10.58^{+0.04}_{-0.05}$	150.5	$-6.64^{+0.37}_{-0.47}$	$-6.25^{+0.20}_{-0.20}$
488076699	62.096336	-53.944173	0.30792	19.259	$10.67^{+0.05}_{-0.07}$	159.9	$-6.62^{+0.36}_{-0.46}$	$-6.27^{+0.20}_{-0.21}$
MUSE21/488071544	62.087179	-53.913732	0.98821	22.458	$10.21^{+0.23}_{-0.32}$	50.3	$-6.88^{+0.53}_{-0.81}$	$-6.30^{+0.25}_{-0.31}$
488067820	62.129495	-53.889946	0.25191	21.049	$9.53^{+0.09}_{-0.11}$	90.3	$-7.49^{+0.57}_{-0.86}$	$-6.30^{+0.21}_{-0.22}$
MUSE3/488069277	62.103394	-53.889095	0.40779	23.661	$8.52^{+0.27}_{-0.32}$	47.6	$-8.40^{+0.43}_{-0.53}$	$-6.31^{+0.27}_{-0.31}$
488068050	62.133568	-53.897135	0.46159	20.744	$9.75^{+0.09}_{-0.10}$	92.1	$-7.31^{+0.53}_{-0.77}$	$-6.32^{+0.21}_{-0.22}$
MUSE26/488070824	62.095831	-53.909607	1.25062	22.383	$10.49^{+0.19}_{-0.22}$	36.8	$-6.76^{+0.43}_{-0.57}$	$-6.33^{+0.24}_{-0.26}$
488071089	62.049904	-53.911313	0.30581	21.203	$9.64^{+0.10}_{-0.12}$	95.3	$-7.43^{+0.56}_{-0.83}$	$-6.34^{+0.21}_{-0.22}$
488065930	62.137580	-53.888784	0.57825	21.113	$10.08^{+0.11}_{-0.12}$	107.7	$-7.08^{+0.47}_{-0.65}$	$-6.38^{+0.21}_{-0.22}$
488069700	62.083413	-53.882657	0.27216	22.456	$8.80^{+0.16}_{-0.21}$	63.8	$-8.23^{+0.50}_{-0.72}$	$-6.39^{+0.23}_{-0.25}$
489521068	62.092960	-53.861224	0.27153	20.306	$10.21^{+0.07}_{-0.12}$	139.3	$-6.98^{+0.43}_{-0.60}$	$-6.40^{+0.20}_{-0.22}$
489521448	62.103449	-53.864717	0.43985	20.616	$10.23^{+0.10}_{-0.15}$	129.6	$-6.97^{+0.44}_{-0.62}$	$-6.41^{+0.21}_{-0.23}$
488072561	62.053602	-53.920059	0.62960	21.216	$10.16^{+0.09}_{-0.11}$	106.6	$-7.04^{+0.45}_{-0.61}$	$-6.41^{+0.21}_{-0.22}$
488074608	62.140970	-53.931443	0.43054	20.683	$10.53^{+0.05}_{-0.05}$	156.2	$-6.84^{+0.38}_{-0.48}$	$-6.43^{+0.20}_{-0.20}$
488070133	62.169886	-53.887360	0.59607	20.158	$10.84^{+0.14}_{-0.12}$	174.5	$-6.74^{+0.36}_{-0.44}$	$-6.47^{+0.22}_{-0.22}$
488073762	62.131777	-53.926465	0.42904	21.665	$10.11^{+0.08}_{-0.14}$	129.8	$-7.15^{+0.45}_{-0.65}$	$-6.49^{+0.21}_{-0.23}$
488073021	62.080583	-53.922670	0.30741	21.184	$9.21^{+0.08}_{-0.09}$	84.6	$-7.96^{+0.59}_{-0.89}$	$-6.49^{+0.21}_{-0.21}$
489522199	62.081990	-53.870601	0.39730	21.866	$9.72^{+0.14}_{-0.24}$	106.9	$-7.51^{+0.56}_{-0.90}$	$-6.50^{+0.22}_{-0.27}$
488072604	62.073251	-53.920150	0.77290	22.129	$10.07^{+0.16}_{-0.19}$	81.5	$-7.20^{+0.50}_{-0.71}$	$-6.50^{+0.23}_{-0.25}$
489521528	62.088464	-53.864945	0.24688	20.718	$9.83^{+0.09}_{-0.08}$	125.9	$-7.43^{+0.52}_{-0.73}$	$-6.52^{+0.21}_{-0.21}$
488069699	62.097258	-53.886716	0.92560	22.617	$9.67^{+0.22}_{-0.23}$	49.6	$-7.58^{+0.61}_{-0.91}$	$-6.52^{+0.25}_{-0.27}$

488070602	62.030809	-53.908820	0.26729	20.096	$9.86^{+0.06}_{-0.06}$	130.4	$-7.45^{+0.50}_{-0.71}$	$-6.56^{+0.20}_{-0.21}$
489523576	62.050079	-53.881679	0.94745	22.694	$11.08^{+0.07}_{-0.08}$	107.8	$-6.73^{+0.29}_{-0.36}$	$-6.57^{+0.20}_{-0.21}$
MUSE24/488069253	62.104998	-53.902502	1.14831	23.055	$9.55^{+0.26}_{-0.28}$	32.3	$-7.76^{+0.66}_{-1.01}$	$-6.59^{+0.27}_{-0.29}$
488074678	62.146922	-53.934938	0.27044	19.713	$10.34^{+0.04}_{-0.04}$	174.0	$-7.09^{+0.40}_{-0.52}$	$-6.59^{+0.20}_{-0.20}$
488074840	62.107311	-53.932685	0.73105	21.409	$10.54^{+0.09}_{-0.11}$	123.4	$-7.00^{+0.38}_{-0.50}$	$-6.59^{+0.21}_{-0.22}$
488071415	62.113750	-53.913080	0.74981	22.287	$9.54^{+0.18}_{-0.15}$	68.6	$-7.78^{+0.61}_{-0.89}$	$-6.60^{+0.24}_{-0.23}$
488070947	62.158048	-53.912350	0.76818	18.274	$11.02^{+0.10}_{-0.14}$	150.3	$-6.80^{+0.32}_{-0.41}$	$-6.60^{+0.21}_{-0.23}$
488067669	62.135908	-53.895219	0.46127	22.257	$9.47^{+0.18}_{-0.28}$	98.0	$-7.85^{+0.62}_{-1.03}$	$-6.61^{+0.23}_{-0.29}$
488071411	62.045447	-53.913359	0.30642	21.438	$9.44^{+0.10}_{-0.11}$	107.0	$-7.89^{+0.58}_{-0.89}$	$-6.63^{+0.21}_{-0.22}$
489523301	62.097716	-53.879281	0.27278	22.768	$8.75^{+0.16}_{-0.22}$	75.8	$-8.53^{+0.46}_{-0.67}$	$-6.65^{+0.23}_{-0.26}$
488072531	62.108813	-53.919489	0.75070	22.550	$9.73^{+0.17}_{-0.20}$	80.6	$-7.68^{+0.57}_{-0.86}$	$-6.67^{+0.23}_{-0.25}$
488070816	62.035444	-53.909470	0.60004	22.347	$9.92^{+0.23}_{-0.24}$	121.6	$-7.52^{+0.58}_{-0.82}$	$-6.68^{+0.25}_{-0.27}$
404169047	62.136795	-53.861686	0.16020	18.916	$10.04^{+0.04}_{-0.04}$	169.1	$-7.42^{+0.46}_{-0.63}$	$-6.69^{+0.20}_{-0.20}$
488070607	62.037079	-53.908383	0.59964	22.356	$9.76^{+0.18}_{-0.21}$	117.2	$-7.72^{+0.57}_{-0.85}$	$-6.74^{+0.23}_{-0.26}$
488067357	62.163804	-53.896708	0.72762	21.625	$10.72^{+0.06}_{-0.11}$	156.1	$-7.10^{+0.36}_{-0.46}$	$-6.77^{+0.20}_{-0.22}$
404169634	62.112378	-53.871809	0.80252	21.675	$10.34^{+0.15}_{-0.37}$	111.3	$-7.28^{+0.43}_{-0.72}$	$-6.79^{+0.22}_{-0.34}$
488074345	62.179533	-53.930268	0.43930	20.522	$10.58^{+0.06}_{-0.12}$	218.3	$-7.23^{+0.37}_{-0.50}$	$-6.84^{+0.20}_{-0.22}$
489521853	62.084697	-53.867583	0.27148	21.675	$9.27^{+0.12}_{-0.13}$	116.9	$-8.25^{+0.60}_{-0.92}$	$-6.84^{+0.21}_{-0.22}$
488078736	62.114845	-53.953040	0.42826	21.346	$10.35^{+0.07}_{-0.09}$	198.2	$-7.36^{+0.40}_{-0.53}$	$-6.86^{+0.21}_{-0.21}$
488066250	62.017973	-53.905064	0.57028	21.306	$10.05^{+0.10}_{-0.14}$	154.8	$-7.59^{+0.47}_{-0.68}$	$-6.87^{+0.21}_{-0.23}$
488069992	62.129682	-53.882696	0.23970	21.880	$8.93^{+0.10}_{-0.12}$	103.8	$-8.63^{+0.53}_{-0.78}$	$-6.91^{+0.21}_{-0.22}$
488074838	62.144448	-53.932510	0.50871	21.484	$9.97^{+0.09}_{-0.13}$	164.1	$-7.75^{+0.49}_{-0.70}$	$-6.96^{+0.21}_{-0.22}$
488078018	62.078114	-53.949484	0.51766	21.911	$10.14^{+0.09}_{-0.17}$	180.4	$-7.60^{+0.45}_{-0.67}$	$-6.96^{+0.21}_{-0.24}$
488073172	62.142324	-53.923373	0.39342	21.554	$9.52^{+0.12}_{-0.12}$	138.8	$-8.18^{+0.58}_{-0.87}$	$-6.98^{+0.21}_{-0.22}$
488077424	62.142854	-53.946644	0.39071	21.170	$10.14^{+0.07}_{-0.09}$	201.7	$-7.65^{+0.44}_{-0.60}$	$-7.01^{+0.21}_{-0.21}$
488077861	62.077259	-53.948516	0.51744	21.566	$10.04^{+0.10}_{-0.12}$	177.3	$-7.75^{+0.48}_{-0.66}$	$-7.01^{+0.21}_{-0.22}$
488075668	62.133767	-53.937477	0.42807	20.447	$9.77^{+0.07}_{-0.06}$	163.6	$-8.01^{+0.52}_{-0.75}$	$-7.04^{+0.21}_{-0.21}$
488067945	62.019121	-53.902892	0.57171	21.720	$9.77^{+0.10}_{-0.13}$	151.6	$-8.02^{+0.53}_{-0.79}$	$-7.04^{+0.21}_{-0.23}$
488072443	62.054344	-53.919213	0.27226	22.046	$8.75^{+0.14}_{-0.13}$	103.4	$-8.94^{+0.45}_{-0.58}$	$-7.06^{+0.22}_{-0.22}$
488068654	62.143374	-53.894424	0.81351	22.007	$10.04^{+0.19}_{-0.23}$	114.0	$-7.79^{+0.53}_{-0.77}$	$-7.06^{+0.24}_{-0.27}$
488071272	62.133772	-53.912201	0.15809	22.207	$8.60^{+0.13}_{-0.16}$	102.1	$-9.09^{+0.29}_{-0.36}$	$-7.07^{+0.22}_{-0.23}$
488072984	62.146444	-53.921724	0.60815	22.144	$9.68^{+0.13}_{-0.18}$	142.5	$-8.13^{+0.56}_{-0.86}$	$-7.08^{+0.22}_{-0.24}$
488068672	62.140255	-53.894233	0.16682	21.453	$8.67^{+0.13}_{-0.14}$	107.7	$-9.04^{+0.37}_{-0.47}$	$-7.09^{+0.22}_{-0.23}$
488073629	62.125366	-53.926127	0.63364	22.258	$9.43^{+0.16}_{-0.16}$	120.1	$-8.38^{+0.61}_{-0.92}$	$-7.10^{+0.23}_{-0.23}$
488073466	62.165107	-53.925645	0.93736	20.916	$11.24^{+0.05}_{-0.07}$	183.5	$-7.21^{+0.26}_{-0.31}$	$-7.12^{+0.20}_{-0.21}$
488073766	62.050530	-53.926881	0.75824	22.336	$9.92^{+0.21}_{-0.34}$	128.8	$-8.00^{+0.57}_{-0.95}$	$-7.17^{+0.25}_{-0.33}$
488070459	62.171977	-53.907068	0.37773	21.361	$9.65^{+0.11}_{-0.12}$	174.9	$-8.25^{+0.56}_{-0.83}$	$-7.17^{+0.21}_{-0.22}$
488070459	62.171977	-53.907068	0.37779	21.361	$9.65^{+0.11}_{-0.12}$	174.9	$-8.25^{+0.56}_{-0.83}$	$-7.17^{+0.21}_{-0.22}$
488072024	62.037238	-53.917791	0.37796	22.807	$9.08^{+0.18}_{-0.26}$	129.9	$-8.78^{+0.62}_{-1.01}$	$-7.19^{+0.24}_{-0.28}$
488070460	62.171213	-53.906968	0.79720	22.595	$10.56^{+0.08}_{-0.08}$	173.2	$-7.60^{+0.38}_{-0.48}$	$-7.19^{+0.21}_{-0.21}$
488072618	62.142800	-53.919871	0.77739	22.398	$10.00^{+0.17}_{-0.35}$	132.3	$-7.96^{+0.52}_{-0.93}$	$-7.19^{+0.23}_{-0.33}$

488070460	62.171213	-53.906968	0.79737	22.595	$10.56^{+0.08}_{-0.08}$	173.2	$-7.60^{+0.38}_{-0.48}$	$-7.19^{+0.21}_{-0.21}$
488074030	62.163437	-53.927404	0.46567	21.400	$9.79^{+0.10}_{-0.11}$	183.8	$-8.16^{+0.53}_{-0.76}$	$-7.20^{+0.21}_{-0.22}$
488070027	62.154997	-53.888704	0.81379	22.887	$10.25^{+0.18}_{-0.26}$	142.8	$-7.74^{+0.49}_{-0.73}$	$-7.20^{+0.24}_{-0.28}$
404169734	62.125315	-53.873569	0.76243	22.755	$9.75^{+0.23}_{-0.30}$	120.3	$-8.20^{+0.61}_{-0.96}$	$-7.21^{+0.26}_{-0.30}$
488075485	62.112254	-53.935970	0.29471	22.103	$9.08^{+0.12}_{-0.14}$	137.9	$-8.80^{+0.58}_{-0.89}$	$-7.21^{+0.22}_{-0.23}$
404169375	62.133682	-53.867494	0.16039	20.977	$9.07^{+0.11}_{-0.12}$	148.4	$-8.82^{+0.58}_{-0.88}$	$-7.22^{+0.21}_{-0.22}$
MUSE25/488070944	62.098868	-53.909951	1.25002	23.508	$9.42^{+0.19}_{-0.26}$	40.4	$-8.50^{+0.63}_{-1.02}$	$-7.22^{+0.24}_{-0.28}$
488067796	62.025664	-53.892284	0.91979	21.768	$10.53^{+0.10}_{-0.31}$	140.1	$-7.65^{+0.39}_{-0.63}$	$-7.24^{+0.21}_{-0.31}$
488073160	62.043694	-53.923652	0.91456	22.098	$10.36^{+0.18}_{-0.20}$	130.9	$-7.75^{+0.44}_{-0.58}$	$-7.26^{+0.24}_{-0.25}$
404169737	62.148449	-53.873747	0.75002	22.097	$10.09^{+0.15}_{-0.19}$	155.0	$-7.95^{+0.49}_{-0.70}$	$-7.26^{+0.22}_{-0.25}$
MUSE28/488067056	62.107634	-53.905654	1.25400	23.100	$9.45^{+0.23}_{-0.25}$	42.0	$-8.52^{+0.65}_{-1.00}$	$-7.26^{+0.25}_{-0.28}$
404169584	62.156567	-53.871330	0.80070	21.188	$10.48^{+0.29}_{-0.13}$	174.0	$-7.70^{+0.49}_{-0.52}$	$-7.27^{+0.28}_{-0.22}$
405340085	62.140943	-53.880240	0.30034	21.842	$8.88^{+0.18}_{-0.13}$	128.4	$-9.04^{+0.55}_{-0.74}$	$-7.27^{+0.24}_{-0.22}$
488077259	62.092037	-53.945258	0.54971	22.234	$9.56^{+0.15}_{-0.18}$	163.4	$-8.44^{+0.59}_{-0.91}$	$-7.28^{+0.22}_{-0.24}$
489521272	62.090218	-53.862527	0.63286	22.813	$9.36^{+0.23}_{-0.25}$	134.5	$-8.64^{+0.66}_{-1.02}$	$-7.30^{+0.25}_{-0.28}$
489523103	62.037949	-53.878208	0.89700	21.083	$10.30^{+0.13}_{-0.17}$	136.0	$-7.83^{+0.43}_{-0.58}$	$-7.31^{+0.22}_{-0.24}$
488076578	62.107604	-53.941787	0.79782	21.477	$10.19^{+0.14}_{-0.16}$	155.2	$-7.91^{+0.47}_{-0.64}$	$-7.32^{+0.22}_{-0.23}$
489521533	62.082318	-53.864622	0.67459	23.344	$9.38^{+0.26}_{-0.28}$	128.1	$-8.65^{+0.68}_{-1.05}$	$-7.33^{+0.27}_{-0.29}$
489522088	62.038672	-53.869800	0.59969	22.534	$9.40^{+0.27}_{-0.25}$	154.2	$-8.66^{+0.68}_{-1.02}$	$-7.36^{+0.27}_{-0.28}$
488072301	62.160850	-53.917944	0.59760	22.185	$9.47^{+0.16}_{-0.18}$	162.9	$-8.61^{+0.61}_{-0.93}$	$-7.37^{+0.23}_{-0.24}$
404169401	62.147459	-53.869008	0.75141	21.712	$10.05^{+0.24}_{-0.28}$	164.3	$-8.10^{+0.57}_{-0.82}$	$-7.38^{+0.26}_{-0.29}$
404169402	62.130404	-53.867675	0.59397	23.104	$9.20^{+0.26}_{-0.33}$	143.7	$-8.88^{+0.68}_{-1.12}$	$-7.40^{+0.27}_{-0.32}$
404169758	62.146052	-53.874054	0.75095	22.586	$9.85^{+0.16}_{-0.21}$	150.3	$-8.31^{+0.55}_{-0.82}$	$-7.40^{+0.23}_{-0.25}$
404169588	62.151601	-53.871104	0.56693	22.810	$9.40^{+0.18}_{-0.19}$	166.1	$-8.73^{+0.62}_{-0.95}$	$-7.43^{+0.23}_{-0.25}$
488076552	62.105955	-53.941347	0.36171	22.388	$9.03^{+0.16}_{-0.17}$	152.8	$-9.06^{+0.59}_{-0.89}$	$-7.43^{+0.23}_{-0.24}$
488078159	62.047075	-53.950191	0.56953	21.811	$9.71^{+0.09}_{-0.12}$	203.1	$-8.49^{+0.54}_{-0.80}$	$-7.46^{+0.21}_{-0.22}$
489522305	62.030458	-53.871796	0.91911	22.148	$10.48^{+0.19}_{-0.38}$	162.5	$-7.90^{+0.43}_{-0.70}$	$-7.46^{+0.24}_{-0.35}$
488073582	62.036870	-53.925643	0.91818	21.953	$10.27^{+0.18}_{-0.28}$	146.6	$-8.01^{+0.45}_{-0.66}$	$-7.48^{+0.23}_{-0.29}$
489522522	62.023889	-53.873587	0.59935	22.742	$9.35^{+0.18}_{-0.25}$	170.0	$-8.87^{+0.63}_{-1.03}$	$-7.52^{+0.24}_{-0.28}$
488075100	62.135113	-53.933925	0.42804	22.300	$8.97^{+0.07}_{-0.07}$	154.9	$-9.22^{+0.54}_{-0.79}$	$-7.54^{+0.21}_{-0.21}$
404168970	62.143547	-53.858498	0.84037	22.020	$10.35^{+0.16}_{-0.17}$	186.9	$-8.04^{+0.43}_{-0.57}$	$-7.55^{+0.23}_{-0.24}$
404169534	62.142829	-53.870321	0.80082	21.848	$9.86^{+0.19}_{-0.17}$	153.9	$-8.45^{+0.56}_{-0.78}$	$-7.55^{+0.24}_{-0.24}$
488073010	62.046958	-53.922500	0.27124	22.409	$8.37^{+0.16}_{-0.14}$	123.0	$-9.78^{+0.25}_{-0.22}$	$-7.56^{+0.23}_{-0.23}$
488079339	62.108903	-53.956880	0.42895	21.139	$9.48^{+0.09}_{-0.08}$	208.9	$-8.80^{+0.58}_{-0.86}$	$-7.56^{+0.21}_{-0.21}$
488070430	62.027802	-53.906937	0.95625	22.490	$10.13^{+0.21}_{-0.32}$	135.2	$-8.23^{+0.53}_{-0.84}$	$-7.57^{+0.24}_{-0.31}$
488071245	62.030863	-53.912062	0.77531	22.736	$9.46^{+0.25}_{-0.19}$	133.7	$-8.84^{+0.66}_{-0.94}$	$-7.59^{+0.26}_{-0.25}$
488078889	62.046282	-53.955925	0.19565	20.697	$9.31^{+0.10}_{-0.10}$	222.4	$-8.98^{+0.59}_{-0.90}$	$-7.60^{+0.21}_{-0.21}$
489521965	62.045558	-53.868686	0.89759	22.513	$10.04^{+0.21}_{-0.24}$	147.2	$-8.33^{+0.55}_{-0.78}$	$-7.60^{+0.25}_{-0.27}$
488065215	62.027412	-53.885104	1.10526	22.372	$10.66^{+0.26}_{-0.37}$	143.9	$-7.99^{+0.45}_{-0.67}$	$-7.63^{+0.27}_{-0.34}$
488075166	62.149266	-53.934182	0.50880	22.887	$9.14^{+0.19}_{-0.24}$	175.5	$-9.18^{+0.63}_{-1.00}$	$-7.64^{+0.24}_{-0.27}$
488068535	62.149540	-53.895034	0.77707	22.702	$9.28^{+0.24}_{-0.22}$	126.6	$-9.06^{+0.66}_{-0.99}$	$-7.65^{+0.26}_{-0.26}$

488073904	62.151510	-53.927139	0.27214	22.822	$8.74^{+0.12}_{-0.16}$	162.5	$-9.55^{+0.43}_{-0.58}$	$-7.66^{+0.22}_{-0.23}$
488068835	62.019738	-53.894319	0.91905	22.531	$10.05^{+0.21}_{-0.26}$	151.3	$-8.40^{+0.54}_{-0.80}$	$-7.68^{+0.25}_{-0.28}$
405340125	62.147848	-53.880963	0.82674	22.738	$9.58^{+0.23}_{-0.27}$	139.6	$-8.83^{+0.64}_{-0.99}$	$-7.69^{+0.26}_{-0.29}$
488076126	62.098545	-53.939165	0.29568	22.286	$8.45^{+0.12}_{-0.11}$	142.4	$-9.86^{+0.19}_{-0.18}$	$-7.71^{+0.21}_{-0.22}$
488074972	62.158897	-53.933231	0.27187	22.261	$8.93^{+0.11}_{-0.13}$	188.4	$-9.43^{+0.54}_{-0.79}$	$-7.71^{+0.21}_{-0.22}$
488073464	62.128601	-53.924891	1.08324	22.899	$10.15^{+0.25}_{-0.33}$	121.1	$-8.35^{+0.57}_{-0.85}$	$-7.72^{+0.26}_{-0.32}$
488072862	62.014278	-53.921997	0.44369	22.954	$8.99^{+0.17}_{-0.23}$	180.0	$-9.41^{+0.59}_{-0.92}$	$-7.73^{+0.23}_{-0.26}$
488071425	62.019165	-53.913520	0.77498	22.912	$9.57^{+0.18}_{-0.24}$	158.9	$-8.89^{+0.60}_{-0.96}$	$-7.74^{+0.23}_{-0.27}$
488077585	62.091222	-53.947042	0.85319	23.034	$9.94^{+0.17}_{-0.20}$	169.8	$-8.57^{+0.54}_{-0.77}$	$-7.75^{+0.23}_{-0.25}$
404169398	62.129582	-53.867590	1.04896	22.750	$10.28^{+0.30}_{-0.36}$	142.9	$-8.28^{+0.51}_{-0.72}$	$-7.75^{+0.29}_{-0.34}$
488076873	62.062246	-53.943414	0.51666	22.956	$8.90^{+0.28}_{-0.27}$	167.7	$-9.51^{+0.64}_{-0.89}$	$-7.76^{+0.28}_{-0.28}$
404169833	62.165627	-53.875815	0.61452	22.767	$9.16^{+0.22}_{-0.18}$	181.6	$-9.30^{+0.65}_{-0.95}$	$-7.78^{+0.25}_{-0.24}$
488074337	62.173464	-53.929392	0.40472	22.616	$9.08^{+0.15}_{-0.17}$	205.6	$-9.40^{+0.60}_{-0.92}$	$-7.81^{+0.22}_{-0.24}$
488067934	62.032469	-53.898319	1.34023	21.519	$10.94^{+0.05}_{-0.04}$	123.0	$-8.04^{+0.32}_{-0.39}$	$-7.81^{+0.20}_{-0.20}$
488077841	62.133208	-53.947857	0.35684	22.687	$8.91^{+0.17}_{-0.23}$	195.1	$-9.57^{+0.56}_{-0.85}$	$-7.83^{+0.23}_{-0.26}$
488070960	62.031874	-53.910446	1.23026	21.226	$10.58^{+0.19}_{-0.19}$	129.8	$-8.25^{+0.42}_{-0.54}$	$-7.86^{+0.24}_{-0.25}$
489521442	62.031862	-53.864100	0.90591	22.699	$9.96^{+0.24}_{-0.26}$	179.0	$-8.74^{+0.58}_{-0.83}$	$-7.94^{+0.26}_{-0.28}$
488076117	62.040622	-53.939310	1.01820	22.596	$10.24^{+0.18}_{-0.21}$	176.9	$-8.54^{+0.49}_{-0.67}$	$-7.99^{+0.23}_{-0.26}$
404169065	62.156908	-53.860476	0.75027	22.948	$9.44^{+0.23}_{-0.25}$	200.1	$-9.34^{+0.65}_{-1.01}$	$-8.07^{+0.25}_{-0.28}$
489520262	62.067931	-53.853616	0.91854	22.457	$9.71^{+0.25}_{-0.23}$	173.3	$-9.12^{+0.63}_{-0.89}$	$-8.10^{+0.26}_{-0.26}$
404169193	62.141088	-53.862996	1.16021	22.384	$10.50^{+0.21}_{-0.30}$	170.9	$-8.52^{+0.44}_{-0.63}$	$-8.10^{+0.25}_{-0.30}$
404169489	62.136503	-53.870431	0.04355	21.430	$7.60^{+0.37}_{-0.32}$	144.3	$-11.07^{+0.59}_{-0.51}$	$-8.16^{+0.32}_{-0.31}$
404169659	62.146071	-53.872477	1.14904	21.682	$9.98^{+0.17}_{-0.22}$	153.9	$-9.09^{+0.53}_{-0.78}$	$-8.31^{+0.23}_{-0.26}$
488075055	62.169444	-53.933578	1.03614	22.691	$10.13^{+0.17}_{-0.32}$	206.8	$-8.97^{+0.50}_{-0.84}$	$-8.32^{+0.23}_{-0.31}$
404169176	62.145040	-53.862782	1.14723	22.928	$10.20^{+0.24}_{-0.30}$	176.9	$-8.92^{+0.55}_{-0.80}$	$-8.33^{+0.26}_{-0.30}$
404169154	62.149335	-53.862340	1.14884	22.251	$9.78^{+0.20}_{-0.24}$	184.1	$-9.66^{+0.59}_{-0.88}$	$-8.69^{+0.24}_{-0.27}$
488073779	62.020985	-53.927277	1.38408	22.280	$10.52^{+0.18}_{-0.24}$	177.2	$-9.12^{+0.42}_{-0.58}$	$-8.70^{+0.23}_{-0.27}$
488072310	62.161986	-53.918003	1.25287	22.603	$9.08^{+0.18}_{-0.14}$	165.2	$-10.89^{+0.61}_{-0.89}$	$-9.31^{+0.23}_{-0.23}$
488072700	62.160696	-53.920293	1.25468	22.908	$9.07^{+0.25}_{-0.24}$	166.2	$-10.93^{+0.66}_{-0.98}$	$-9.33^{+0.26}_{-0.27}$
488072408	62.161866	-53.918519	1.25018	22.937	$8.95^{+0.18}_{-0.19}$	165.7	$-11.10^{+0.58}_{-0.86}$	$-9.40^{+0.24}_{-0.25}$
404169985	62.153722	-53.878539	1.41999	22.613	$9.23^{+0.26}_{-0.24}$	154.7	$-11.00^{+0.68}_{-1.02}$	$-9.55^{+0.27}_{-0.27}$
489520462	62.073666	-53.855405	1.17034	22.110	$7.69^{+0.45}_{-0.45}$	164.0	$-12.93^{+0.72}_{-0.72}$	$-10.10^{+0.37}_{-0.39}$
489520752	62.055153	-53.858062	1.59303	22.328	$9.14^{+0.29}_{-0.23}$	168.1	$-11.75^{+0.70}_{-0.99}$	$-10.21^{+0.28}_{-0.27}$
3070263610	62.040098	-53.885262	1.32360	-	-	119.0	-	-
3070263850	62.075161	-53.892278	0.91583	-	-	42.4	-	-
3070265512	62.076105	-53.885866	0.91540	-	-	58.9	-	-
3070264072	62.073661	-53.889176	0.76790	-	-	52.4	-	-
MUSE1	62.093482	-53.907716	0.23983	–	–	28.9	–	–
MUSE2	62.088497	-53.889554	0.28757	–	–	37.4	–	–
MUSE4	62.079502	-53.896486	0.55446	–	–	26.2	–	–
MUSE5	62.092164	-53.902560	0.59221	–	–	10.3	–	–

MUSE7	62.086607	-53.902732	0.59822	–	–	13.0	–	–
MUSE11	62.092623	-53.909149	0.64338	–	–	33.7	–	–
MUSE13	62.088612	-53.911555	0.76379	–	–	42.2	–	–
MUSE16	62.075319	-53.889095	0.76863	–	–	50.4	–	–
MUSE17	62.095373	-53.907544	0.82980	–	–	29.5	–	–
MUSE18	62.069991	-53.898778	0.85458	–	–	43.5	–	–
MUSE23	62.082424	-53.891043	1.13208	–	–	36.1	–	–
MUSE27	62.084658	-53.911326	1.25152	–	–	42.9	–	–
				WGD 2038−4008				
169190452	309.539131	-40.115839	0.22917	18.213	$10.76^{+0.04}_{-0.04}$	107.9	$-6.39^{+0.35}_{-0.43}$	$-6.08^{+0.20}_{-0.20}$
169192596	309.492815	-40.140131	0.23003	21.389	$9.28^{+0.11}_{-0.18}$	52.3	$-7.61^{+0.60}_{-0.96}$	$-6.21^{+0.21}_{-0.24}$
169191228	309.535586	-40.122881	0.22900	20.025	$10.13^{+0.07}_{-0.11}$	83.9	$-6.86^{+0.45}_{-0.62}$	$-6.21^{+0.21}_{-0.22}$
169189459	309.539963	-40.103707	0.22827	17.848	$11.00^{+0.04}_{-0.04}$	143.5	$-6.47^{+0.30}_{-0.37}$	$-6.27^{+0.20}_{-0.20}$
169192249	309.537431	-40.135642	0.22864	21.077	$9.60^{+0.08}_{-0.09}$	71.9	$-7.50^{+0.56}_{-0.82}$	$-6.38^{+0.21}_{-0.21}$
169192351	309.523347	-40.137071	0.42874	20.494	$10.12^{+0.10}_{-0.12}$	32.9	$-7.05^{+0.46}_{-0.63}$	$-6.39^{+0.21}_{-0.22}$
169191897	309.517763	-40.130806	0.34445	22.210	$8.69^{+0.13}_{-0.12}$	28.5	$-8.56^{+0.40}_{-0.49}$	$-6.63^{+0.22}_{-0.22}$
169193594	309.514195	-40.155037	0.27820	21.126	$9.31^{+0.11}_{-0.13}$	65.3	$-8.19^{+0.60}_{-0.92}$	$-6.81^{+0.21}_{-0.22}$
169194640	309.471495	-40.170293	0.23647	19.289	$10.42^{+0.06}_{-0.06}$	162.4	$-7.38^{+0.39}_{-0.51}$	$-6.91^{+0.20}_{-0.21}$
169192636	309.498710	-40.140676	0.42710	22.669	$9.45^{+0.16}_{-0.26}$	37.3	$-8.27^{+0.61}_{-1.01}$	$-7.02^{+0.23}_{-0.28}$
169193902	309.487074	-40.160804	0.42725	18.676	$11.35^{+0.03}_{-0.03}$	108.6	$-7.09^{+0.24}_{-0.27}$	$-7.04^{+0.20}_{-0.20}$
169191786	309.521701	-40.129094	0.34157	22.937	$8.60^{+0.23}_{-0.18}$	40.3	$-9.15^{+0.43}_{-0.40}$	$-7.13^{+0.26}_{-0.24}$
169191437	309.540911	-40.125437	0.22716	21.577	$8.65^{+0.10}_{-0.10}$	91.4	$-9.34^{+0.33}_{-0.39}$	$-7.37^{+0.21}_{-0.21}$
169193432	309.557474	-40.152652	0.34079	19.475	$10.47^{+0.07}_{-0.07}$	138.8	$-7.83^{+0.39}_{-0.50}$	$-7.39^{+0.21}_{-0.21}$
169194065	309.562909	-40.162398	0.34506	19.299	$10.78^{+0.07}_{-0.05}$	168.7	$-7.75^{+0.35}_{-0.43}$	$-7.45^{+0.20}_{-0.20}$
169191326	309.496715	-40.122896	0.34271	22.345	$8.96^{+0.18}_{-0.19}$	64.9	$-9.20^{+0.58}_{-0.86}$	$-7.50^{+0.23}_{-0.25}$
169189145	309.516470	-40.095073	0.20084	19.786	$9.31^{+0.11}_{-0.11}$	151.7	$-8.89^{+0.60}_{-0.91}$	$-7.51^{+0.21}_{-0.22}$
169192814	309.520646	-40.143046	0.52902	22.046	$9.57^{+0.20}_{-0.22}$	33.5	$-8.75^{+0.62}_{-0.94}$	$-7.60^{+0.24}_{-0.26}$
169194067	309.482408	-40.160695	0.07580	20.890	$8.19^{+0.26}_{-0.19}$	116.7	$-10.15^{+0.41}_{-0.31}$	$-7.77^{+0.27}_{-0.25}$
169193455	309.496328	-40.151391	0.36829	22.005	$8.79^{+0.11}_{-0.12}$	66.3	$-9.68^{+0.46}_{-0.62}$	$-7.83^{+0.21}_{-0.22}$
169189914	309.518874	-40.103760	0.19742	22.878	$8.00^{+0.20}_{-0.17}$	121.5	$-10.71^{+0.32}_{-0.27}$	$-8.16^{+0.24}_{-0.24}$
169194531	309.503092	-40.167505	0.42654	21.622	$9.83^{+0.10}_{-0.12}$	112.1	$-9.10^{+0.52}_{-0.75}$	$-8.18^{+0.21}_{-0.22}$
169189067	309.542813	-40.092954	0.28598	21.217	$9.10^{+0.14}_{-0.12}$	180.7	$-9.92^{+0.60}_{-0.89}$	$-8.35^{+0.22}_{-0.22}$
169193237	309.561418	-40.148516	0.34018	22.225	$9.14^{+0.12}_{-0.14}$	143.8	$-9.92^{+0.59}_{-0.91}$	$-8.39^{+0.22}_{-0.23}$
169193555	309.568673	-40.153285	0.34218	21.564	$9.39^{+0.12}_{-0.14}$	168.2	$-9.75^{+0.59}_{-0.92}$	$-8.43^{+0.21}_{-0.23}$
169191966	309.541745	-40.132233	0.60086	20.513	$10.76^{+0.07}_{-0.23}$	85.3	$-9.01^{+0.35}_{-0.52}$	$-8.70^{+0.21}_{-0.26}$
169189826	309.535769	-40.102557	0.47794	22.031	$9.99^{+0.08}_{-0.09}$	141.1	$-9.52^{+0.48}_{-0.67}$	$-8.75^{+0.21}_{-0.21}$
169194495	309.511978	-40.166836	1.13033	22.524	$10.29^{+0.24}_{-0.27}$	107.3	$-9.34^{+0.48}_{-0.64}$	$-8.82^{+0.26}_{-0.29}$
169193901	309.570179	-40.158238	0.47405	21.269	$10.18^{+0.09}_{-0.11}$	178.9	$-9.50^{+0.44}_{-0.60}$	$-8.89^{+0.21}_{-0.22}$
169189023	309.491739	-40.092652	0.54487	20.724	$10.80^{+0.03}_{-0.03}$	168.6	$-9.26^{+0.34}_{-0.42}$	$-8.97^{+0.20}_{-0.20}$
169193078	309.564077	-40.146099	0.34071	22.869	$8.37^{+0.14}_{-0.14}$	148.7	$-11.21^{+0.23}_{-0.23}$	$-8.99^{+0.22}_{-0.23}$
169191992	309.457026	-40.131800	0.51834	21.469	$9.85^{+0.11}_{-0.13}$	150.8	$-10.17^{+0.52}_{-0.75}$	$-9.27^{+0.21}_{-0.22}$

169195181	309.510546	-40.177017	1.17836	22.655	$9.61^{+0.15}_{-0.17}$	144.0	$-10.62^{+0.58}_{-0.88}$	$-9.51^{+0.23}_{-0.24}$
169192635	309.485842	-40.140711	1.35058	20.463	$7.58^{+0.37}_{-0.41}$	71.5	$-12.53^{+0.60}_{-0.66}$	$-9.61^{+0.32}_{-0.37}$
169191596	309.458841	-40.126588	0.48342	22.409	$8.93^{+0.18}_{-0.17}$	149.4	$-11.35^{+0.57}_{-0.82}$	$-9.63^{+0.23}_{-0.24}$
169190526	309.539140	-40.111919	0.91987	21.537	$10.65^{+0.18}_{-0.33}$	118.4	$-10.39^{+0.41}_{-0.63}$	$-10.03^{+0.24}_{-0.32}$
169196183	309.518797	-40.190901	0.97564	21.295	$10.77^{+0.24}_{-0.32}$	195.0	$-10.38^{+0.43}_{-0.60}$	$-10.08^{+0.26}_{-0.31}$
169193763	309.500311	-40.155916	0.67100	22.476	$9.75^{+0.27}_{-0.19}$	74.5	$-11.24^{+0.65}_{-0.84}$	$-10.25^{+0.28}_{-0.25}$
169189572	309.526023	-40.099386	0.62258	20.045	$9.74^{+0.07}_{-0.05}$	141.4	$-11.35^{+0.53}_{-0.75}$	$-10.35^{+0.20}_{-0.20}$
169192546	309.545721	-40.139586	0.67484	21.345	$10.03^{+0.11}_{-0.16}$	95.0	$-11.16^{+0.48}_{-0.70}$	$-10.43^{+0.21}_{-0.23}$
169194605	309.556455	-40.168268	0.60064	22.811	$9.43^{+0.21}_{-0.27}$	167.4	$-11.80^{+0.64}_{-1.02}$	$-10.52^{+0.25}_{-0.28}$
169194113	309.498489	-40.161174	0.87838	22.655	$10.00^{+0.22}_{-0.26}$	93.9	$-11.50^{+0.56}_{-0.81}$	$-10.74^{+0.25}_{-0.28}$
169195495	309.501974	-40.181155	0.92178	21.862	$9.98^{+0.19}_{-0.16}$	161.0	$-11.68^{+0.54}_{-0.72}$	$-10.89^{+0.24}_{-0.23}$
169190809	309.511333	-40.116436	0.81855	20.801	$10.56^{+0.18}_{-0.24}$	74.1	$-11.89^{+0.42}_{-0.58}$	$-11.50^{+0.24}_{-0.27}$
169193629	309.483800	-40.153801	0.82247	21.200	$10.41^{+0.16}_{-0.16}$	97.0	$-12.27^{+0.42}_{-0.55}$	$-11.80^{+0.23}_{-0.23}$
169196130	309.490867	-40.190128	0.81949	21.775	$10.90^{+0.04}_{-0.05}$	199.3	$-12.75^{+0.32}_{-0.40}$	$-12.50^{+0.20}_{-0.20}$
169195905	309.520673	-40.186885	0.82054	21.349	$10.42^{+0.15}_{-0.20}$	181.3	$-13.15^{+0.42}_{-0.57}$	$-12.69^{+0.23}_{-0.25}$
14	309.515660	-40.134512	0.77392	21.462	$10.55^{+0.08}_{-0.12}$	14.9	$-14.27^{+0.38}_{-0.50}$	$-13.87^{+0.21}_{-0.22}$
13	309.515880	-40.135034	0.77492	20.761	$11.32^{+0.05}_{-0.06}$	14.3	$-14.00^{+0.24}_{-0.29}$	$-13.94^{+0.20}_{-0.20}$
169194395	309.544629	-40.165182	0.76076	22.386	$10.04^{+0.32}_{-0.18}$	136.6	$-14.95^{+0.66}_{-0.71}$	$-14.22^{+0.30}_{-0.24}$
169194256	309.543818	-40.163338	0.76067	22.326	$9.84^{+0.19}_{-0.27}$	130.2	$-15.19^{+0.57}_{-0.89}$	$-14.29^{+0.24}_{-0.29}$
169190626	309.551365	-40.113228	0.78249	22.480	$9.87^{+0.21}_{-0.30}$	139.5	$-17.17^{+0.58}_{-0.92}$	$-16.28^{+0.25}_{-0.30}$
15	309.516878	-40.135319	0.77619	22.884	$10.18^{+0.13}_{-0.20}$	16.3	$-17.18^{+0.46}_{-0.69}$	$-16.58^{+0.22}_{-0.25}$
169192350	309.514393	-40.137815	-9.00000	-	-	8.8	-	-

Table A2: Properties of galaxies in each trial group. The columns display, in order, the coordinates (RA, DEC in degrees; ICRS), redshift z, DES i-band `MOF_CM_MAG_CORRECTED` magnitudes (if available; assigned a value of -99 if not), ID, and whether that galaxy passes the iterative group membership algorithm described in §5.1. Spectroscopic redshift uncertainties are about 100 $\mathrm{km\,s^{-1}}$, or 0.00033 in redshift. Galaxies with DES Y3 IDs have 9 digits, while galaxies with DES Y1 IDs have 10 digits. The lens galaxy is indicated as such, and galaxies with spectroscopic redshifts from MUSE have IDs that begin with "MUSE"

RA	DEC	z	i-band Mag	ID	Group Member?
			DES J0408−5354		
			Group 1		
62.030809	-53.908820	0.26729	20.096	488070602	False
62.084697	-53.867583	0.27148	21.675	489521853	True
62.061177	-53.921532	0.27257	19.767	488072697	True
62.144676	-53.934498	0.27176	18.315	488074578	True
62.084648	-53.885204	0.27247	18.309	488070148	True
62.097716	-53.879281	0.27278	22.768	489523301	True
62.046958	-53.922500	0.27124	22.409	488073010	True
62.092960	-53.861224	0.27153	20.306	489521068	True

62.054344	-53.919213	0.27226	22.046	488072443	True
62.151510	-53.927139	0.27214	22.822	488073904	True
62.146922	-53.934938	0.27044	19.713	488074678	False
62.158897	-53.933231	0.27187	22.261	488074972	True
62.083413	-53.882657	0.27216	22.456	488069700	True
			Group 2		
62.049904	-53.911313	0.30581	21.203	488071089	True
62.045447	-53.913359	0.30642	21.438	488071411	True
62.080583	-53.922670	0.30741	21.184	488073021	True
62.093088	-53.919040	0.30909	21.573	488072433	True
62.096336	-53.944173	0.30792	19.259	488076699	True
62.020675	-53.907526	0.30566	19.692	488067185	True
			Group 3		
62.139479	-53.928501	0.42858	19.429	488073735	True
62.025309	-53.910519	0.42954	19.664	488070449	False
62.114845	-53.953040	0.42826	21.346	488078736	True
62.108903	-53.956880	0.42895	21.139	488079339	True
62.131777	-53.926465	0.42904	21.665	488073762	True
62.148320	-53.919275	0.42744	20.060	488072414	True
62.133767	-53.937477	0.42807	20.447	488075668	True
62.135113	-53.933925	0.42804	22.300	488075100	True
62.140970	-53.931443	0.43054	20.683	488074608	False
			Group 4		
62.106161	-53.923866	0.57035	20.933	488073290	True
62.023367	-53.910705	0.57025	19.314	488066235	True
62.151601	-53.871104	0.56693	22.810	404169588	False
62.047075	-53.950191	0.56953	21.811	488078159	True
62.017973	-53.905064	0.57028	21.306	488066250	True
62.019121	-53.902892	0.57171	21.720	488067945	True
			Group 5		
62.037079	-53.908383	0.59964	22.356	488070607	True
62.169886	-53.887360	0.59607	20.158	488070133	True
62.160850	-53.917944	0.59760	22.185	488072301	True
62.130404	-53.867675	0.59397	23.104	404169402	False
62.035444	-53.909470	0.60004	22.347	488070816	True
62.068708	-53.913477	0.59843	21.581	488071428	True
62.071692	-53.906245	0.59727	-9999.000	488066584	True
62.134647	-53.901754	0.59479	21.047	488067363	False
62.078380	-53.881917	0.59451	19.918	489523481	False
62.072770	-53.910296	0.59811	19.975	488070807	True
62.083912	-53.903969	0.60048	22.304	488066462	True

62.067875	-53.910488	0.59977	21.729	488070966	True
62.038672	-53.869800	0.59969	22.534	489522088	True
62.023889	-53.873587	0.59935	22.742	489522522	True
62.095575	-53.898291	0.59441	21.867	488065185	False
62.090417	-53.899889	0.59671	19.770	Lens	True
62.092164	-53.902560	0.59221	-99.000	MUSE5	False
62.077898	-53.903878	0.59797	-99.000	MUSE6	True
62.086607	-53.902732	0.59822	-99.000	MUSE7	True
62.103108	-53.897861	0.59832	-99.000	MUSE8	True
62.085632	-53.891330	0.59906	-99.000	MUSE9	True
62.085862	-53.910180	0.60029	-99.000	MUSE10	True
			Group 6		
62.148449	-53.873747	0.75002	22.097	404169737	True
62.113750	-53.913080	0.74981	22.287	488071415	False
62.147459	-53.869008	0.75141	21.712	404169401	True
62.156908	-53.860476	0.75027	22.948	404169065	False
62.146052	-53.874054	0.75095	22.586	404169758	True
62.108813	-53.919489	0.75070	22.550	488072531	False
			Group 7		
62.106067	-53.909453	0.77562	21.908	488070825	False
62.158048	-53.912350	0.76818	18.274	488070947	False
62.125315	-53.873569	0.76243	22.755	404169734	False
62.073251	-53.920150	0.77290	22.129	488072604	False
62.090965	-53.901634	0.76866	20.096	488068102	True
62.050530	-53.926881	0.75824	22.336	488073766	False
62.090541	-53.904725	0.77568	22.925	488066886	False
62.030863	-53.912062	0.77531	22.736	488071245	False
62.019165	-53.913520	0.77498	22.912	488071425	False
62.090243	-53.903609	0.77069	22.015	488066144	False
62.073661	-53.889176	0.76790	-99.000	3070264072.0	True
62.088612	-53.911555	0.76379	-99.000	MUSE13	False
62.099785	-53.908977	0.76669	-99.000	MUSE14	True
62.080992	-53.904565	0.76785	-99.000	MUSE15	True
62.075319	-53.889095	0.76863	-99.000	MUSE16	True
			Group 8		
62.142829	-53.870321	0.80082	21.848	404169534	True
62.107604	-53.941787	0.79782	21.477	488076578	True
62.171213	-53.906968	0.79737	22.595	488070460	True
62.156567	-53.871330	0.80070	21.188	404169584	True
62.112378	-53.871809	0.80252	21.675	404169634	True
62.171213	-53.906968	0.79720	22.595	488070460	True

			Group 9		
62.036870	-53.925643	0.91818	21.953	488073582	True
62.043694	-53.923652	0.91456	22.098	488073160	True
62.025664	-53.892284	0.91979	21.768	488067796	True
62.030458	-53.871796	0.91911	22.148	489522305	True
62.019738	-53.894319	0.91905	22.531	488068835	True
62.067931	-53.853616	0.91854	22.457	489520262	True
62.075161	-53.892278	0.91583	-99.000	3070263850.0	True
62.076105	-53.885866	0.91540	-99.000	3070265512.0	True
62.088268	-53.890642	0.91504	-99.000	MUSE19	True
			Group 10		
62.161866	-53.918519	1.25018	22.937	488072408	True
62.160696	-53.920293	1.25468	22.908	488072700	True
62.161986	-53.918003	1.25287	22.603	488072310	True
62.098868	-53.909951	1.25002	-99.000	MUSE25	True
62.095831	-53.909607	1.25062	-99.000	MUSE26	True
62.084658	-53.911326	1.25152	-99.000	MUSE27	True
62.107634	-53.905654	1.25400	-99.000	MUSE28	True
			WGD 2038−4008		
			Group 1		
309.492815	-40.140131	0.23003	21.389	169192596	True
309.539963	-40.103707	0.22827	17.848	169189459	True
309.539131	-40.115839	0.22917	18.213	169190452	True
309.535586	-40.122881	0.22900	20.025	169191228	True
309.540911	-40.125437	0.22716	21.577	169191437	True
309.537431	-40.135642	0.22864	21.077	169192249	True
309.511379	-40.137024	0.22829	–	169191076/Lens	True
			Group 2		
309.521701	-40.129094	0.34157	22.937	169191786	True
309.517763	-40.130806	0.34445	22.210	169191897	True
309.564077	-40.146099	0.34071	22.869	169193078	True
309.561418	-40.148516	0.34018	22.225	169193237	True
309.557474	-40.152652	0.34079	19.475	169193432	True
309.496715	-40.122896	0.34271	22.345	169191326	True
309.568673	-40.153285	0.34218	21.564	169193555	True
309.562909	-40.162398	0.34506	19.299	169194065	True

This paper has been typeset from a TEX/LATEX file prepared by the author.

Table A3. Properties of redMaPPer clusters in the field of view of WGD 2038−4008 . The columns show the cluster ID, cluster redshift, richness, velocity dispersion (rounded to the nearest $10\,\mathrm{km\,s^{-1}}$), the group centroid (in RA and Dec), projected distance of the centroid to the lens ($\Delta\theta$), and flexion shift $\log(\Delta_3 x(\mathrm{arcsec}))$. See §6.3 for further discussion

MEM_MATCH_ID	$\bar{z}_{\mathrm{group}}$	λ	σ_{group} ($\mathrm{km\,s^{-1}}$)	$\mathrm{RA_{ctr}}$, $\mathrm{DEC_{ctr}}$ (deg)	$\Delta\theta$ (arcsec)	$\log_{10}(\Delta_3 x)$ ($\log_{10}$(arcsec))
62659	0.221 ± 0.008	5.1 ± 1.7	340^{+60}_{-70}	309.53913, -40.11584	107.9	$-5.1^{+0.3}_{-0.4}$
138669	0.405 ± 0.017	10.8 ± 2.0	430^{+50}_{-60}	309.48707, -40.16080	108.6	-6.0 ± 0.2